MRI safety of implants: transfer function determination from MR images

Janot Tokaya

Cover design   J.P. Tokaya

MRI safety of implants: transfer function determination from MR images
PhD thesis, Utrecht University, The Netherlands

Manuscript

Layout: J.P. Tokaya
Typeset in: LaTeX 2_ε
Printed by: Ridderprint
ISBN: 9789039372418

MRI safety of implants: transfer function determination from MR images

MRI veiligheid van implantaten: bepaling van de transfer functie uit MRI beelden

(met een samenvatting in het Nederlands)

Proefschrift

ter verkrijging van de graad van doctor aan de Universiteit Utrecht
op gezag van de rector magnificus, prof. dr. H.R.B.M. Kummeling,
ingevolge het besluit van het college voor promoties
in het openbaar te verdedigen
op dinsdag 7 januari 2020 om 16.15 uur

door:

Janot Philippe Tokaya
geboren op 9 augustus 1989
te Groningen, Nederland

Promotoren: Prof. dr. P.R. Luijten
Copromotoren: Dr. ir. C.A.T. van den Berg
                 Dr. ir. A.J.E. Raaijmakers

Contents

Preface

Originally, the work presented here was started in a collaboration with Sapiens Steering Brain Stimulation. This company, now acquired by Medtronic, resulted from research at Philips Healthcare that was aimed at improving care of Parkinson's patients. Sapiens was developing a deep brain stimulator with a steerable therapeutic electric excitation field. Topics of shared scientific interest between the imaging department of the UMC Utrecht and Sapiens included coping with susceptibility artifacts due to main magnetic field distortions by metallic objects, heating assessment by means of MR thermometry[1] and MR based current measurements. All these topics involve mitigating of even utilizing image distortions caused by an implant in MR images.

---

[1] Heating can be measured with MRI using thermometry, either relying on the temperature dependence of the proton resonance frequency or of the spin-lattice relaxation time.

List of Symbols and Abbreviations

AIMD	Active Implantable Medical Device
B_0	Static magnetic field
B_1	Radiofrequency magnetic field
B_1^+	Positively rotating radiofrequency magnetic field
DBS	Deep Brain Stimulator
D	Electric displacement field in coulomb per meter square(in this context assumed to be harmonically rotating at the RF frequency)
EM	ElectroMagnetic
E	Electric field in V/m (in this context assumed to be harmonically rotating at the RF frequency)
FDTD	Finite Difference Time Domain
$\frac{\mathrm{d}}{\mathrm{d}t}$	Time derivative operator
G	Gradient magnetic field
M	Transfer matrix
MRI	Magnetic Resonance Imaging
NSA	Number of Signal Averages
R	Pearson correlation coefficient
RF	RadioFrequency
RMS	Root Mean Square
SAR	Specific Absorption Rate
SNR	Signal-to-Noise Ratio
$S(q)$	Transfer function (q parametrized the trajectory of the implant)
TF	Tranfer Function (always shorthand for RF electric field tranfer function)
TM	Tranfer Matrix (always shorthand for RF electric field transfer matrix)

General Introduction

1.1 Challenges and opportunities

In modern healthcare, medical imaging plays a crucial role. Its importance as a diagnostic tool and as a means of treatment response monitoring is well established. Additionally, medical imaging is used to gain insights in fundamental mechanisms in the human body and to unravel causes behind diseases. Especially Magnetic Resonance Imaging (MRI) has proven its value because of a superior soft tissue contrast compared to other modalities and the possibilities to measure neurological and endovascular functionality, metabolism, diffusion, temperature changes and many other relevant physical, physiological and anatomical parameters. The absence of ionizing radiation furthermore distinguishes MRI from computed tomography (CT), X-ray imaging and positron-emission tomography (PET). For many suspected conditions MRI is the modality of choice and its worldwide usage is increasing (OECD).

Due to the aging population and advances in medical device technology the prevalence of implants is also growing [1–3]. Not everybody in this growing patient population is able to benefit from the increased availability and capabilities of MR imaging. Unfortunately, some implants are contra-indicated for MRI exams because of hazardous interactions between the metallic structures in the implant and the electromagnetic fields necessary to produce an MR image. Conflictingly, the patient group with implants is more likely to need MRI exams. It is for example estimated that three out of four patients with a pace-

maker or defibrillator would benefit from an MRI scan during the lifetime of their device [4]. Next to the challenges that are faced when using the MR as a diagnostic modality on patients with implants also opportunities arise. The interactions between the implant and the MR scanner cause distinct image distortions that can be used as experimental instruments to characterize and gain insight into these interactions. This insight led to this thesis' aspiration of assessing implant safety using MRI. Steps towards this goal are presented in the upcoming chapters, but first a short review of MRI with a focus on the electromagnetic fields and the risks associated with implants is provided.

1.2 MRI principles

The description of MRI given here will be far from exhaustive. For more elaborate discussions the reader is referred to a wide variety of text books [5–7]. An MR scanner creates three (electro)magnetic fields to produce images of internal structures and processes in the human body. Firstly, a static magnetic field, called B0, is applied that creates a preference for the intrinsic magnetic moments of atomic nuclei (called spins) to be in a state of alignment with it (see fig 1B). In nearly all human tissues the distribution of spin orientations is skewed towards antiparallel alignment with B0 as most tissue types are weakly diamagnetic [8]. A net bulk magnetization is created. The spins will furthermore precess around B_0 with a frequency proportional to the strength of the magnetic field. This phenomenon is called Larmor precession and the frequency of precession is called Larmor frequency. For magnetic field strengths typically used (1.5, 3 or 7 tesla) the Larmor frequency of protons is in the radiofrequency (RF) range (e.g. 64, 128 or 298 MHz).

Secondly, a radiofrequency electromagnetic field is applied with a magnetic component rotating at this Larmor frequency, called B_1. Its projection onto the positively rotating transverse plane (in the convention with B_0 in the z-direction) at the Larmor frequency results in stationary component in this frame, called the B1+ field. The B_1^+ applies an effective torque to tip the net magnetization away from the direction of B0 (as shown in fig 1C). The strength of B_1^+ field is several tens of microteslas. Subsequently, the magnetization when tipped away from B_0 will like the individual spins exhibit Larmor precession. This rotating magnetization generates a time-varying magnetic flux outside the patient which is picked up as a MR signal by a detection coil through Faraday induction.

Lastly, magnetic gradient fields with a spatially varying field strength up
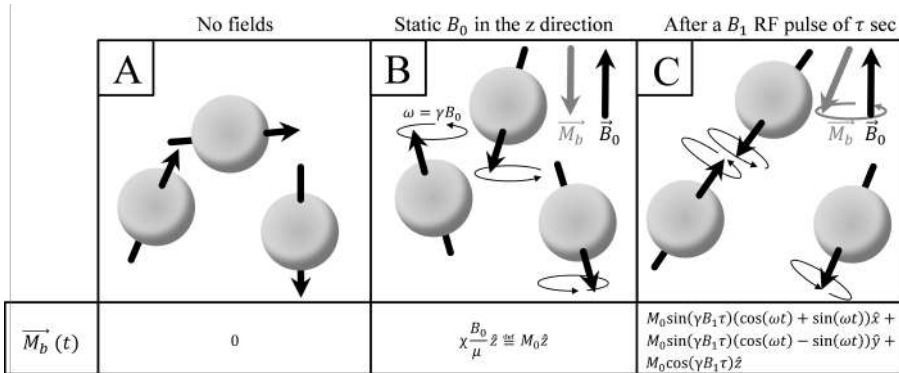
	No fields	Static B_0 in the z direction	After a B_1 RF pulse of τ sec
$\overrightarrow{M_b}(t)$	0	$\chi\frac{B_0}{\mu}\hat{z} \overset{\text{def}}{=} M_0\hat{z}$	$M_0\sin(\gamma B_1\tau)(\cos(\omega t)+\sin(\omega t))\hat{x} +$ $M_0\sin(\gamma B_1\tau)(\cos(\omega t)-\sin(\omega t))\hat{y} +$ $M_0\cos(\gamma B_1\tau)\hat{z}$

Figure 1.1: The principle behind MRI in the classical picture. The unordered spins of for example water protons align parallel or antiparallel with an external magnetic field to form a net magnetization. In figure B a magnetic field in the z-direction of magnitude B_0 is applied. The spins will start to precess around the main magnetic field direction. This phenomenon is known as Larmor precession. An RF pulse can be used to tilt the magnetization away from the B_0 direction which in turn will start to precess. This creates a measurable rotating magnetization as shown in C. Gradients are used to encode the signals spatially by making ω a function of spatial location, e.g. $\omega(\vec{r})$.

to tens of militelsas per meter are used to locally change the rotation frequency. This spatially encodes the MR signals, which is necessary to create images.

1.3 Safety aspects of the three magnetic fields of an MRI scanner

Because the B_0 field is static, safety concerns mainly relate to forces and torques on ferromagnetic objects. Fatal MRI incidents with oxygen cylinders [9] and vacuum cleaners [10] that turned into projectiles when brought accidentally into the vicinity of an MR scanner have happened [11]. In the absence of metallic objects, the B_0 field induces only minor effects in the human body. Physiological effects like blood pressure changes due to hydrodynamic forces caused by the Lorentz force on the moving blood in our veins and arteries do occur, but have been proven insignificant [12–14] and remain unnoticed. Nausea and vertigo are well-known and temporary effects [15] caused by motion of the vestibular system in the static magnetic field when moving the patient into the scanner. Despite their unpleasant nature they are not considered a serious safety concern.

The gradient fields add a relatively small component to the B_0 field. Still,

the dynamic nature of the gradient fields introduces new safety considerations. The gradient can switch polarity in less than a millisecond with slew rates up to 200 T/m/s to make rapid spatial encoding possible. The currents that run in the gradient coil change orientation to switch the polarity of the gradient field. The Lorentz forces on the conductors carrying these currents in the B0 field will also change direction. This results in vibrations of the gradient coils resulting in loud noises [16], sometimes exceeding 130dB [17], characteristic to MRI. To avoid noise induced hearing loss [18] the mandatory ear protection is simple solution. More importantly, A time varying magnetic field, like the gradient and RF field, cannot exist without an electric component. This is stated by Faraday's law of induction:

$$\oint_C \vec{E} \cdot \mathrm{d}\vec{l} = -\oiint_V \frac{\mathrm{d}\vec{B}}{\mathrm{d}t} \vec{\mathrm{d}l} \tag{1.1}$$

In this equation $\vec{B}$ stands for the time varying magnetic field with field lines going through a surface S. On any closed contour C within this surface, an electric field $\vec{E}$ will be present. The incident time-varing magnetic field that the gradient coils create will produce electric fields in the body that can lead to electric potential differences across nerves. If these potentials become high enough nerves can be activated leading to muscle contraction. The threshold of cardiac or respiratory stimulation is not reached in commercial systems [19] and only the peripheral nerves are stimulated unintentionally due to the enforced operational limits (for example in the US, the gradient slew rate limits are set at 200 T/m/s). Unintended peripheral nerve stimulation, like the loud noises, nausea and vertigo, can hence be uncomfortable, but do not pose a serious safety threat.

Equation 1 also dictates that the time-varying RF B1 field has an associated electric field component. The RF magnetic field, being about 1-20 μ T (three orders of magnitude weaker than the gradient field), changes five orders of magnitude more rapidly. Hence, its associated electric field is one to two orders of magnitude stronger. The physiological response of nerves fortunately is too slow for unintended stimulation. Nonetheless, another effect associated with electric fields is more pronounced. When an electric field, is present in a conductive medium, currents are induced that deposited energy through collisions of the moving charged particles within the medium. This energy deposition will result in what is known as ohmic heating. Human tissues are (poorly) conductive in the considered RF frequency regime and hence exhibit ohmic heating. For frequencies above ~1GHz dielectric heating due to

dipole rotations and vibrations become relevant, but the role of this effect in MRI is minimal.

Limitations on the electric fields that RF coils produce in a subject are formulated to restrict the maximal whole-body temperature rise to 1 degree Celsius. The amount of power deposited by an electromagnetic field in the 100kHz to 10GHz range in a volume of conductive tissues is described by the so-called specific absorption rate (SAR):

$$\langle SAR \rangle = \frac{1}{V} \int SAR(\vec{r}) \mathrm{d}V = \frac{1}{V} \int \frac{\sigma(\vec{r}) \left| \vec{E}(\vec{r}) \right|^2}{2\rho(\vec{r})} \mathrm{d}V \qquad (1.2)$$

In this equation $\sigma(\vec{r})$ is the electrical conductivity of the medium permeated by an electric field with magnitude of E. The density of the medium is $\rho(\vec{r})$ and the volume over which the SAR is calculated is V. Common integration volumes are taken to be the entire body (whole body SAR) or by 1g or 10g total mass for local SAR. General local and global limits for human exposure to RF fields are given by the International Commission of Non-Ionizing radiation protection [20]. MRI specific guidelines have been formulated by the International Electrotechnical Commission (IEC 60601-2-33) on the maximal averaged local and global SAR a patient is allowed to receive. Abiding these regulations, with global SAR restrictions for volume transmit coils and both local and global restrictions for local transmit coils, ensures that no harmful tissue heating occurs anywhere in the body of a patient due the RF fields of the MRI system [21].

1.4   Implants and MRI

The first medical implants were used decades before MRI was invented [22]. A distinction is made between active implantable medical devices (AIMD), usually powered by a battery to replace or assist (neuronal) functionality in the human body, and passive implants. Examples of active implants are pacemakers, defibrillators, neural stimulators and cochlear implants. Cardiovascular stents and orthopedic implants are examples of passive implants.

Nowadays considerations about MR safety have tremendous impact on the design of both passive and active implants. The first necessary condition for MRI compatibility is the absence of sizeable ferromagnetic components in a medical implant. If the materials the implant is composed of become strongly magnetized in the B_0 field the implant will be subject to forces, torques

5

and vibrations that potentially cause harm to the patient. For example, iron, cobalt, nickel and some stainless steels are ferromagnetic materials used in medical applications, which can experience strong forces. Implants composed of these metals are generally MRI incompatible. Also, the local distortion of the static magnetic field due to the induced magnetization cause what is known as susceptibility artifacts that decrease the diagnostic value of acquired MR images. Most modern implants consist of other materials like titanium (which can still cause susceptibility artifacts), copper and cobalt-chromium.

Gradients are less prone to produce significant forces or torques, but are able to create vibrations and malfunctioning of devices. For AIMDs furthermore unintended stimulation or device breakdown can be an issue. Sometimes, gradient heating is also a concern [23,24] albeit to lesser extent than RF induced device heating. The RF field can likewise cause malfunction of an implant and unintended stimulation. The biggest concern associated with the RF field however is heating due to currents induced inside the implant. RF induced heating is by far the biggest safety concern and its mitigation has the biggest impact on the design choices made by the manufacturer of AIMDs, which is shown in figure 2.
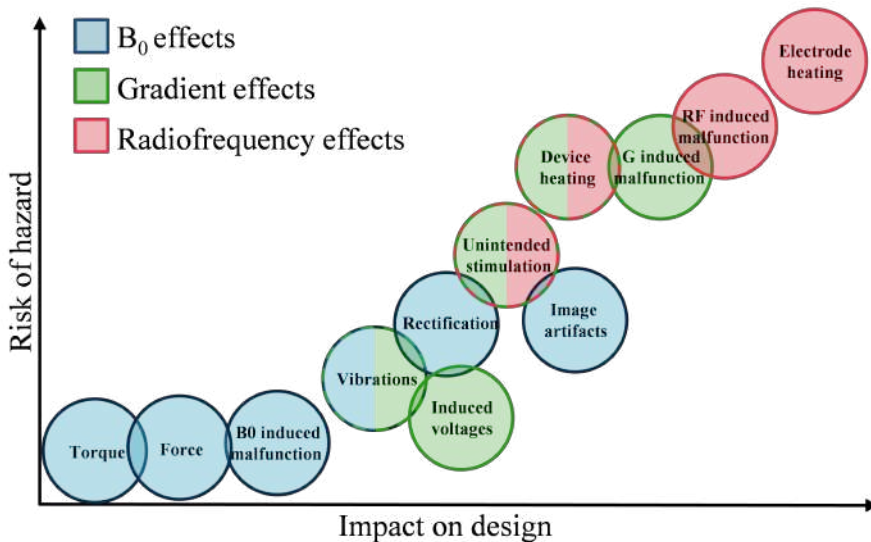

Figure 1.2: The impact various MR related risks have on the design of deep brain stimulator. Similar trends will be found for other AIMDs with leads and guide wires.

Much effort is put into making implants MRI safe(r) and into the accurate assessment of risks associated with specific implants. The RF associated issues are hardest to avoid. The heating is a result of induction of unintended currents in the conductive parts of the implants. Avoidance of the use of conductive materials is for many implants impossible in view of the functionality of the device. Active devices often rely on the delivery of therapeutic or signaling currents that are customarily transmitted through conductive wires towards electrodes. Especially these elongated conductive structures, characteristic to AIMDs are problematic and are known to potentially cause hazardous RF heating during MR exams. This RF risks are summarized in an implant specific MR unsafe or conditional labels which respectively lead to a contraindication for MR exams or define safe operational transmit power limits for the MR scanners. Such MR conditional labels define the operational limits in terms of SAR and B_1 for the MR scanner that guarantee safety of the patient.

1.5 RF heating of AIMDS

Especially elongated structures like guide wires [25] and leads from implanted pacemakers [26], ECGs [27] and deep brain stimulators [28, 29] have shown a capacity cause local tissue heating. Temperature rises of up to 48°C and 20°C degrees have been reported in phantom [30] and pig [26] experiments for guide wires and pacemaker leads respectively. The mechanism behind RF heating is well understood. When a conductive structure is exposed to an electric field, currents will be induced. A current in turn can cause charge accumulation at tissue boundaries where differences in electrical conductivity occur. This results in sharply peaked local electric fields and temperature hotspots [25], predominantly occurring at the electrodes at lead tips of which a situation is shown in figure 3. Contrarily to these dramatic temperature rises patients with implanted pacemakers have been scanned without discovered adverse effects [31, 32] (but only if the implant and/or the imaging sequence is designed accordingly).

Longer implants are particularly precarious because they couple over the entire length to the electric field causing higher potential differences generating stronger currents. If their length become in the order of the effective RF wavelength, there is the risk of resonance effects. This can occur for implants that are approximately half a wavelength of the RF radiation in the surrounding tissue or longer. If the length of an implant is smaller than half a wavelength it is called electrically short. Because the wavelength of the 64MHz RF field (the Larmor frequency at 1.5 T) in average human tissue is around 40 centimeters

many AIMDs do not fall into the electrically short category. The occurrence of resonance depends on an interplay between the incident electric field and the way currents are damped in the implant and can form standing wave patterns, which in turn depend on the properties of the implant [33,34], the surrounding tissues [35], the used RF coil and the relative positions of implant, subject and coil [25, 36–40]. Especially currents in insulated wires often present in AIMDs are not heavily damped and support propagation with relatively little energy losses along their length causing all energy to be deposited at the lead tip.

The growing patient population with medical implants and the increased demand of MR access has put pressure on medical device manufacturers to produce MR safe implants or conditional labels. This triggered the formulation of a standardized process to assess RF heating of AIMDS. This standardized process is described in a technical specification (ISO/TS 10974) that receives broad support from implant manufacturers, MRI vendors, operators and safety experts. The specification aims to streamline the safety assessment to characterize the heating through an implant specific conditional label.

A four tier approach is described in ISO/TS 10974. With each higher tier the complexity of the test method increases, but so does the accuracy of the predicted heating and thus the amount of conservative margin that needs to be applied decreases. The lowest tier is most easily performed but makes the biggest overestimation resulting in extremely conservative scanning restrictions. In tier 1, only applicable to electrically short implants, no numerical modeling of the electromagnetic field is required. The highest possible electric field that can occur in the body region of interest is applied to the implant and the subsequent heating is assessed. For tier 2, which also only applies to electrically short implants, the highest electric field in the body is replaced by the highest electric field found at realistic implant positions. This value is determined through electromagnetic modeling. In tier 3 the electric fields no longer has a fixed magnitude, but a realistic distribution along the length of the implant. The incident electric field distribution along a broad collection of realistic implant trajectories is extracted from simulations of a representative group of subjects. To translate these electric fields into tip heating the so-called electric field transfer function (TF) [41] of an implant is used. The TF translates any electric field incident on an implant to a heating at a specific location, usually the contact points of electrodes. The TF thus removes the necessity to model the implant and MR scanner simultaneously. This, on the other hand, is exactly what is required for the highest tier. In tier 4 a representation of all possible scenarios that can occur in clinical practice are modeled

in concomitant numerical simulations of subject, RF coil and implant. The high level of detail that is necessary to accurately resolve the implant together with the size of the scanner make these simulations extremely computationally expensive. Because tier 4 is often unfeasible, manufacturers of electrically long AIMDs mostly resort to tier 3 for safety assessments.

Tier 3 makes it possible to do a numerical evaluation of enough situations to create a statistical basis for general statements about the potential heating of a certain implant. The implant characteristic TF is determined in separate simulations of the implant only using a reduced computational domain, which makes the required detailed modeling possible. The TF can furthermore be measured/verified in phantom experiments [41, 42]. Currently, experimental TF determination is only possible in homogenous liquid media in dedicated bench setups where electric field probes are employed. To be able to make a realistic translation to in vivo heating, a phantom liquid embedding the implant needs to closely resemble the actual tissue electrical and thermal properties. Nevertheless, the translation from a homogenous surrounding to a realistic environment introduces uncertainties. Generally speaking, in all safety assessments, lacking knowledge and uncertainties lead to the necessity to assume a worst-case scenario. This inevitably results in overly stringent operational limits for the MR scanner, which consequently leads to suboptimal care for the patient.

The potential hazardous RF interaction between the implant and MR scanner also result in typical distortions in the MR image. The current induced in the implant creates a secondary RF magnetic field of its own. This secondary RF magnetic field superimposes on the background B_1^+ field and can be used to resolve the current causing it [43–45] because MRI is able measure this B_1^+ field. As will be shown in the upcoming chapters the current induced in the implant contains valuable information about the RF interaction and the heating potential it has.

1.6 Thesis outline

In the next chapters methods will be explained to measure the TF with MRI. In chapter 1 the implant is modified into a transmit and receive antenna. The current induced in this antenna, which can be determined with MRI, will directly reflect its TF. Even though this method can be used to determine the TF in nonhomogeneous media and solids the modifications that are necessary to change an implant into a transceive antenna limit its practical applicability.
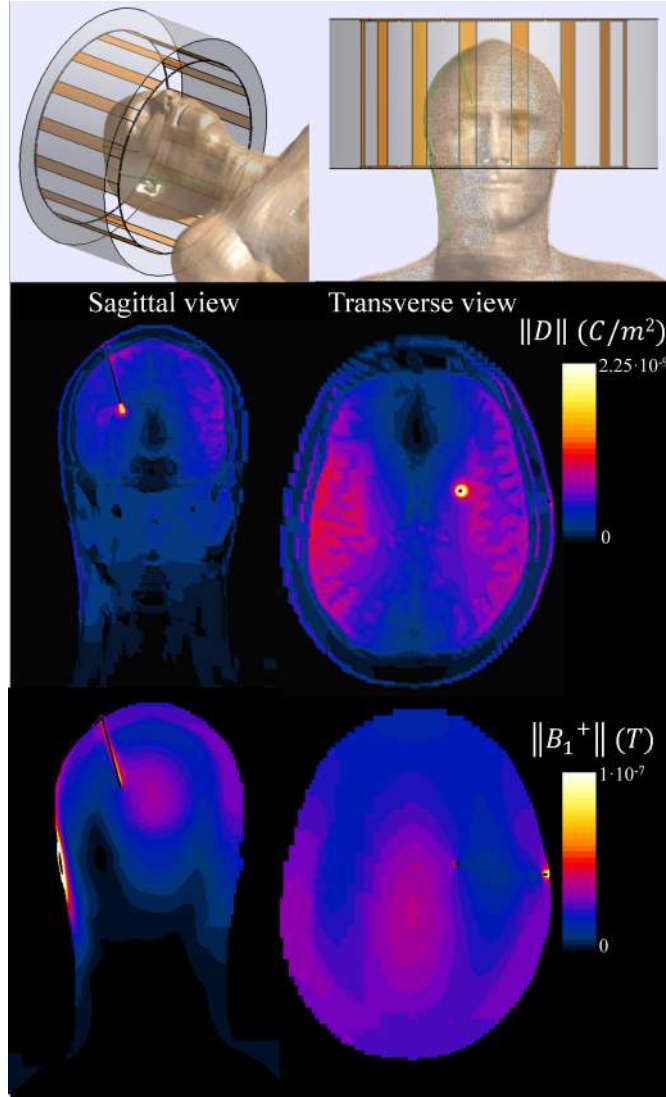
Figure 1.3: An example of the localized electric field enhancement around the lead tip of a deep brain stimulator. The enhancement will result in local heating. The 'displacement field' $D = \epsilon E$ describes the electric field in a medium together with its influence on free and bound charges in it. In the right (counter-clockwise) circularly polarized component of the RF magnetic field, i.e. B_1^+, clear field enhancements and voids are visible.

It allows exploration of the effects of realistic surrounding media, but is not applicable for actually implanted devices.

The methodology hence is modified and extended in chapters three and four to make scanning with the RF coils used in clinical practice possible. The alterations to the implant are no longer required. Because the RF electric fields generated by MR coils are not localized and will always generate an exposure over the entire length of the implant a generalization of the TF was necessary. This extension, named transfer matrix (TM), is introduced in chapter 3. It relates an incident electric field distribution along the length of the implant to an induced current distribution. For bare and (partially) insulated wires an analytical description of the TM is derived by using a transmission line model. If the current in the implant is known, which we can measure with MRI, together with the electric field which can be determined through simulation for a known experimental setup the TM can be determined. This is shown in chapter 3. The knowledge of the electric field, attained through electromagnetic simulations, can only be acquired if the geometrical and dielectric properties of setup are known.

Because this generally is not the case, the method is extended further in chapter 4. Here, the electric field is determined from field distributions that can be measured with an MRI. Still, two assumptions are necessary that will introduce inaccuracies in vivo, but these assumptions are not central to the presented idea. The fully MR based method for TF determination in a phantom experiment presented in chapter 4 brings in vivo TF determination closer to reality. The last chapter dives deeper into the descriptive potential of the transfer matrix.

MRI-Based Transfer Function Determination for the Assessment of Implant Safety

Tokaya, Janot P.
Raaijmakers, Alexander J.E.
Luijten, Peter R.
Bakker, Jurriaan F.
van den Berg, Cornelis A.T.

Abstract

Purpose We introduce a new MR-based method to determine the transfer function (TF) for radiofrequency (RF) safety assessment of active implantable medical devices. Transfer functions are implant-specific measures that relate the incident tangential electric field on an (elongated) implant to a scattered electric field at its tip. The proposed method allows for TF determination with a high spatial resolution in relatively fast measurements without requiring dedicated bench setups from MR images.

Theory and Methods The principle of reciprocity is used in conjunction with the potential to measure currents with MRI to determine the TF. Low-flip angle 3D dual gradient echo MRI data is acquired with an implant as transceive antenna, which requires minimal hardware adaptations. The implant-specific TF is determined from the acquired MRI data, with two different postprocessing methods for comparison.

Results TFs of linear and helical implants can be determined accurately (with a Pearson correlation coefficient $R \geq 0.7$ between measurements and simulations, and a difference in field at the tip $\Delta E_{tip} \leq 19\%$) from relatively quick ($t = 20$ minutes) MRI acquisitions with (several) millimeter spatial resolution.

Conclusion Transfer function determination with MRI for RF safety assessment of implantable medical devices is possible. The proposed MR-based method allows for TF determination in more realistic exposure scenarios and solid media.

Introduction

The patient population with active implantable medical devices (AIMDs), like pacemakers and deep brain stimulators (DBS), is rapidly growing [2, 46]. This patient group more often needs to undergo MRI examinations. For example, the fraction of patients with a pacemaker or defibrillator that would benefit from an MRI scan during the lifetime of their device is estimated to be three out of four [47]. Hence, assessment of MRI-safety of implants is necessary and of growing importance.

Elongated AIMDs often contain metallic structures that potentially interact with the magnetic fields used in MRI and with their associated electric fields [48]. Forces and torques acting on elongated implants, like pacemakers and DBSs, related to the main magnetic field are minor safety issues due to the relatively small content of magnetic materials in these types of implants. The same applies to vibrations induced by switching gradients.

For elongated AIMDs, the electric field component of the rapidly time-varying radiofrequency (RF) fields provokes the gravest safety risk. This electric field can drive currents in conducting structures during MRI examinations. These currents subsequently result in charge accumulation that can become particularly large when currents encounter impedance transitions, for example, at the endings of elongated conducting structures. The accumulated charges cause local and sharply peaked electric fields and consequently high-energy absorption, that is, high local specific absorption rate levels, in proximate tissue. This energy absorption may lead to dangerous tissue temperatures at the tips of elongated structures, for example, the electrode of an implanted pacemaker or DBS lead [**?**, 49]. Logically, much effort has been put into the manipulation of the electric fields to reduce heating [50–52]. Nonetheless, scanning patients with elongated AIMDs is currently contraindicated by most MRI and implant manufacturers, otherwise only conditional safety is guaranteed by imposing severe restrictions on certain scan parameters.

MRI safety (or conditional MRI safety) of an implantable medical device is established by extensive computational investigations alongside experimental studies. Radiofrequency safety assessment by means of brute force numerical simulations of a patient with an AIMD in the MRI is problematic due to the large dimensional difference between the relatively small (often submillimeter) geometrical resolution necessary to accurately model the implant and the size of the human body or the entire MRI environment. Hence, four complementary alternative approaches have been formalized as a four-tier approach in technical

15

International Organization for Standardization/Technical Specification 10974 [53]. Each higher tier results in additional computational and/or experimental effort but a reduction in overestimation of the temperature rise around the implant. A full computational approach is the fourth tier of this technical specification. This method leads to minimal overestimation of the tip heating, but the concomitant computational efforts are elaborate, extensive, and often unfeasible.

In contrast to the fourth-tier approach, the lower tiers require the use of the transfer function (TF) of the implant [54] by exploiting localized nature of tip heating. The TF is an implant characteristic that relates an incident tangential electric-field distribution along the trajectory of an implant to the resultant scattered electric field at the tip of the implant, which drives local heating. It is widely used to assess MRI safety of elongated metallic implants [53].

Present day experimental methods to validate numerically computed TFs rely on a cumbersome technique using a specially designed bench setup that only is applicable in liquid-filled phantom studies. A localized electric field is sequentially applied along the implant, and the TF is determined from subsequent measurements of the resultant electric field at the lead tip. One challenge this technique encounters is the accurate placement of electric field probes and, even more experimentally challenging, the application of a narrow tangential excitation electric field that defines the geometrical resolution of the TF measurement. In theory, an infinitesimal electric excitation field would be required for a correct observation of the TF. Typical setups use a small loop or capacitor, but stray fields are inevitably present, leading to a convolution of the excitation field with the TF in the measurement result. A second challenge is the application of an excitation field at or nearby the tip of an implant while monitoring its response at the same location. This often results in a measured TF with undetermined behavior close to the tip.

It recently has been shown [47], by using the theorem of reciprocity in conjunction with the Huygens Principle 13, that a reciprocal approach also can be employed to determine the transfer behavior of an implant. When a voltage or current source at the tip of an implant is applied, the consequential tangential electric field profile along its trajectory, or equivalently the resultant current distribution through the implant, is the TF after normalization.

Based on this observation and the possibility to determine currents with MRI measurements [45, 55, 56], we present an alternative method to measure

the TF of an implant. We use two (complementary) alternative postprocessing methods to map currents from MRI data; both able to determine TFs with high spatial resolution. These MRI-based methods overcome some of the experimental challenges that conventional TF determination techniques face and, most prominently, can be used to explore more realistic exposure scenarios. The alternative method has the potential to be used in animal tissues, human cadavers, or other heterogeneous media in which conventional methods are inapplicable.

Methods

Firstly, we will repeat the theoretical principles underpinning the TF and introduce how this implant characteristic can be determined with MRI acquisitions. Secondly, we will introduce two methods to determine TFs in EM simulations. The first method is analogous to the conventional experimental method and uses the application of a sequentially repositioned localized tangential field along an implant to determine its TF. The second method relies on a localized excitation at the tip of an implant to determine its TF and confirms the validity of this reciprocal approach. Lastly, we will explain how the reciprocal approach is applied experimentally and how the acquisition of the MRI data from which TFs are determined is performed.

Theory

The scattered electric field $\vec{E}_s$, at a point $\vec{r}$ in the proximity of a tip of an implant as a function of the unit tangential incident field E_{tan} along an implant of length L, whose trajectory is parametrized by q, can be described 12 by

$$\vec{E}_s(\vec{r}) = \vec{E}_{tip}(\vec{r}) \int_0^L S(q)\mathrm{d}q \tag{2.1}$$

In this equation, $S(q)$ is the TF. It is a complex weighting function that determines how the tangential electric field at position q contributes to the field at the tip. A graphical display of the concept of the TF is shown in 2.1. In this description, the dimensionless spatial pattern of the field distribution around the tip, $\vec{E}_{tip}(\vec{r})$ is assumed to be geometrically independent of the incident field.

The TF describes how secondary electric field contributions around the tip of an implant arising from electric fields tangentially incident along the
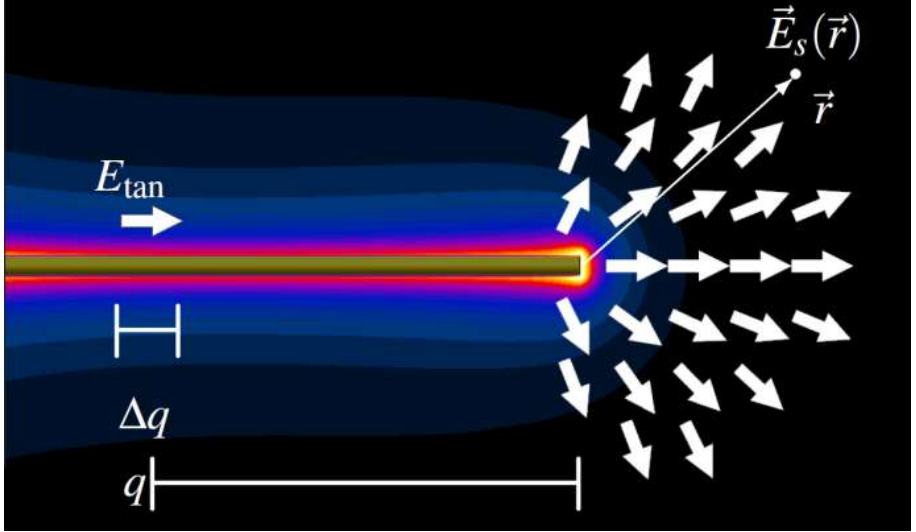
Figure 2.1: A graphical display of the concept of the transfer function. A tangentially incident electric field E_{tan} contributes to a scattered electric field that is particularly focused at the tip of elongated structures. This process is described by an implant specific characteristic called the transfer function.

implant superimpose in a complex fashion. The phase of the TF is a measure of the retardation that a current undergoes propagating from a position q to the tip, and its magnitude is a measure of the attenuation during this propagation. Relying on the principle of reciprocity, the inverse process is described likewise by the TF [47]; that is, the electric field, and thus the current distribution in an implant excited by an infinitesimal source at the tip, also is described by the TF.

This reciprocal approach will be utilized alongside, with the possibility to image currents with MRI techniques [45, 55–57] to determine the TF of an implant in a single measurement. The current-carrying implant, excited at the tip by a coax cable, is used as a transceive antenna during the MRI experiment. The current distribution, which reflects the TF of the implant, produces a magnetic field according to Ampère's circuital law:

$$\oint_C \vec{B} \cdot \mathrm{d}l = \iint \left(\mu_0 \vec{J} + \mu_0 \epsilon_0 \epsilon_r \frac{\partial \vec{E}}{\partial t} \right) \cdot \mathrm{d}\vec{S} \approx \mu_0 I_{enc} \tag{2.2}$$

In this equation, C describes a closed contour around which the magnetic

field $\vec{B}$ is proportional to the electrical and displacement currents through its enclosed surface S. The last approximation, where I_{enc} is the current the wire carries in the enclosed surface, especially holds close to the current-carrying wire because the contribution of the displacement current will be negligible. In this quasi-static approximation for wires parallel to the main magnetic field, we simply find the Biot-Savart law

$$\vec{B} = \frac{\mu_0 I_{enc}}{2\pi r}\hat{\phi} := B_\phi \hat{\phi} \tag{2.3}$$

where $\hat{\phi}$ is the azimuthal unit vector in the cylindrical coordinate system with its z-axis parallel to the static magnetic field.

If this magnetic field is used as the transmit field, in an MRI acquisition, the transverse magnetization generating a spoiled GRE MR signal is proportional to the current in the implant assuming a low flip angle approximation. Subsequently, if the implant is likewise used as a receive antenna the final detected MR signal $\mathcal{S}_{meas}$ is squarely dependent on the enclosed current [58]: i.e.,

$$\mathcal{S}_{meas} \sim B_x^2 + B_y^2 \sim B_\phi^2 \sim I_{enc}^2 \tag{2.4}$$

Note that $\mathcal{S}_{meas}$ and I_{enc} are complex quantities. Hence the current distribution in the implant can be deduced from the acquired MR signal.

MR-Based Transfer Function Determination

We will use two post-processing methods on the MRI data to determine the induced currents in and subsequently the transfer functions of elongated implants. The first method relies on a least squares approximation of the signal by using the law of Biot-Savart. The second method uses loop integration around the implant to determine enclosed currents based on Ampère's circuital law (a specific version of the Biot-Savart law).

The first method relies on the fact that the RF magnetic fields (B_1) are directly proportional to the current running through the implant according to the Biot-Savart law in the quasi-static approximation for the fields in the direct vicinity of the implant,

$$\vec{B}_{implant}(\vec{r}_i) = \frac{\mu_0}{4\pi}\int_C \frac{I(\vec{q_j})\vec{\mathrm{d}q} \times \vec{r}_i}{|r_i|^3} \approx \frac{\mu_0}{4\pi}\sum_{j=1}^{N} \frac{I_j \vec{\mathrm{d}q_j} \times \vec{r}_i}{|r_i|^3} \tag{2.5}$$

The last approximation is a simple transformation of the integral into a Riemann sum by discretization of the current trajectory into small line segments,

$\mathrm{d}\vec{q}_j$. These segments are assumed to be small enough to carry a constant current I_j. In this equation, r_i, is the spatial coordinate describing the magnetic field pattern which is discretized by the positions of the voxels comprised in the MRI data.

The x- and y-component of the magnetic field in the scanner coordinate system (a coordinate system with z-axis parallel to B_0), that are proportional to the current in the wire, determine both the transmit and receive fields. The square of the current in each line segment can be determined from the MRI signal with the following linear least squares minimization assuming the low flip angle approximation is valid:

$$\underset{\tilde{I}_{ews} \in \mathbb{C}^{K \times 1}}{\operatorname{argmin}} \left\| M_{BSM}\tilde{I}_{ews} - \mathcal{S}_{meas} \right\| \tag{2.6}$$

where,

$$(M_{BSM})_{ij} = B_1^+{}_{implant}(\vec{r}_i, \mathrm{d}q_j) B_1^{-*}{}_{implant}(\vec{r}_i, \mathrm{d}q_j) \tag{2.6a}$$

and,

$$\tilde{I}_{ews} = \begin{bmatrix} I_1^2 \\ I_2^2 \\ \vdots \\ I_N^2 \end{bmatrix}. \tag{2.6b}$$

$B_1^+{}_{implant}(\vec{r}_i, \mathrm{d}q_j)$ and $B_1^{-*}{}_{implant}(\vec{r}_i, \mathrm{d}q_j)$ are the transmit and receive fields per unit current respectively, i.e. the fields per unit current in each line segment, that are the counterclockwise and clockwise circularly polarized components of the magnetic field in equation **??** respectively. Their product is a matrix describing the contribution of each current segment on an elongated implant to the signal in each voxel which from now will be called the Biot-Savart Matrix (BSM). Its ith row describes how the ith current segment gives a weighted contribution to the signal in every voxel. Likewise, its jth column describes how all current segments give a weighted contribution to the signal in the jth voxel.

The resultant $\tilde{I}_{ews}$ is a vector containing the element-wise square of the current in each segment that describes the discretized current distribution throughout the wire. The current distribution is determined by the transfer behavior of the implant and hence $\sqrt{\tilde{I}_{ews}}$ is a vector which gives a discretized non-normalized version of the transfer function of the implant. This method to determine transfer functions will be called BSM-method throughout this text.

Method two relies on Ampère's circuital law and simply sums the square root of the MR signal over a closed loop around the implant to obtain a measure of the enclosed current. For each z-slice a square loop integral at five voxels distance from the implant position is calculated reflecting directly the current component ($I_{enc}(z)$), normal to the integration plane, which in turn reflects the transfer function. For this method that from now on will be called loop integral (LI) method, it is important to note that a projection takes place onto the direction of the main magnetic field B_0 as the current is derived from transverse RF magnetic fields. In the experiments it was assured that the implants were aligned along z, i.e. parallel to the main magnetic field and the integration plane was taken in the transverse xy-plane.

Simulations

When comparing electromagnetic finite difference time domain simulations (Sim4Life, ZMT, Zurich, Switzerland) with experimental results generic implants were embedded in a PMMA elliptical phantom model with a size of 600x400 mm, 200 mm radius, 90 mm liquid depth as shown in figure 2A. The dielectric properties of the phantom filling liquid corresponded to those of the saline doped with copper sulfate that was used in experiments. As implants three insulated (0.45 mm PVC) and three bare copper wires with a 2.5 mm diameter of 10, 20 and 30 cm length were used that were available for experiments. For the insulated wires 1 cm of insulation was removed to reproduce implants used in previous studies [41, 47] and allow for comparison with their presented results. To investigate the applicability of MR based TF determination for helical structures, that are often used in elongated implants to mitigate heating [19], a left handed helical wire was devised and simulated. It consisted of a bare copper wire with a 2.5 mm wire diameter, that was wound with a 2.5 mm helix inner diameter, a 5 mm pitch and an axis length of 10 cm.

When comparing the two different simulation techniques to determine the transfer functions, the implants were embedded in a background with the experimentally determined dielectric properties of the phantom filling liquid, using a dielectric assessment kit (DAK-12, SPEAG, Zurich, Switzerland) and a network analyzer (R&S ZNC3). The bare and insulated implants were gridded with a 0.15 mm isotropic resolution in the plane perpendicular to the major axis of the implant and a 0.5 mm resolution along the length of the implant. The helical implant was gridded with a 0.1 mm isotropic resolution. The harmonic simulations had a simulation time of 5 periods, absorbing boundary conditions and were terminated when a -50 dB convergence level was reached.
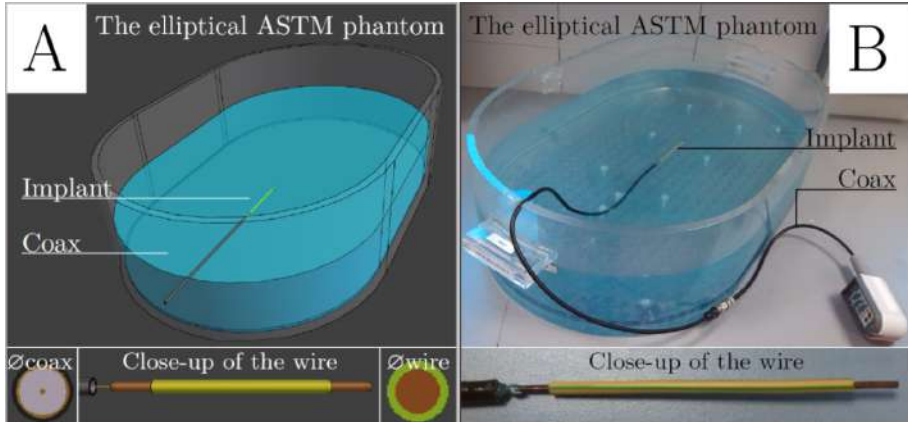
Figure 2.2: The simulation (A) and experimental (B) setup used to determine TFs. A generic implant excited with a coax cable is placed in an elliptical ASTM phantom and used as a transceive antenna in an MRI experiment.

The piecewise excitation method

To achieve a localized tangential electric field incident on the generic implants two counter propagating thin plane wave box sources of 10 cm x 10 cm x 0.5 cm with opposing magnetic and aligned electric fields are used as shown in figure 2.3. Note that the width of the boxes determines both the geometrical resolution of the numerically computed transfer function and the number of simulations required to compute it. This setup of plane wave sources ensures the implant is exposed to a nearly purely tangential electric field excitation. The magnitude of the electric field component parallel to the implant, which is 1.3V/m, exceeds the perpendicular components by at least four orders of magnitude. The magnetic field is zero up to numerical accuracy at the location of the implant due to the destructive interference of the magnetic components of the plane waves. The position of the plane wave boxes is varied along the length of the implant and the resulting electric field at the tip is monitored to determine the transfer function. This approach will be called the piecewise excitation method (PWE) throughout this paper and resembles the current day experimental practice.

The effect of simulation grid resolution on simulation outcome has been checked for all PWE simulations. The simulation grid resolution plays a more important role for the insulated wires because the thickness and shape of the insulation and hence the loading of the implant changes with vary-

ing grid settings. Iterative transfer function simulations with increasing resolution showed convergence at 0.15 mm resolution perpendicular to the major axis of the insulated and the bare implants. Therefore, this resolution was used throughout all simulations. To accurately voxelize to the complex geometry of the helical wire a 0.1 mm isotropic resolution was used.

The coax excitation method

As was stated earlier the transfer function of an implant can also be determined with a reciprocal approach by exciting the implant at the tip and monitoring the resultant tangential electric fields or equivalently the current distribution throughout the structure. Both in experiments and in simulations the excitation at the tip of the implant was created by geometrically connecting it with the inner conductor of a coaxial cable with 0.5 cm of the outer conductor removed. The coaxial cable was simulated as a set of perfectly con-

Figure 2.3: The Piece Wise Excitation (PWE) method in the simulation domain. Two narrow electromagnetic plane wave sources with opposing magnetic fields and aligned electric fields are used to create a localized tangential electric field excitation.

ducting concentric cylinders with a voltage source (of 1V) positioned 15 cm away from the implant connecting the inner to the outer conductor.

The inner conductor has a 0.25 mm radius. The dielectric interior of the coax cable with a 0.25 mm inner and a 1.75 mm outer radius was chosen to be polytetrafluoroethylene (PTFE), a nonconductive dielectric with a relative permittivity of 3. The outer perfectly conducting shell had a thickness of 0.25 mm and the coax was insulated with a 3 mm thick polyethylene layer. A cross section of the model of the coax cable can be seen in figure 2.2A.

Experiments

The MR-based TF determination method was employed to measure the TF of seven generic structures described before. Some of the TFs of the bare and insulated wires are known from literature [41, 59, 60] and the 10 cm insulated wire is similar to a test implant described in safety standards [53, 61]. Therefore the TFs of the linear implants facilitate the validation of the pro-
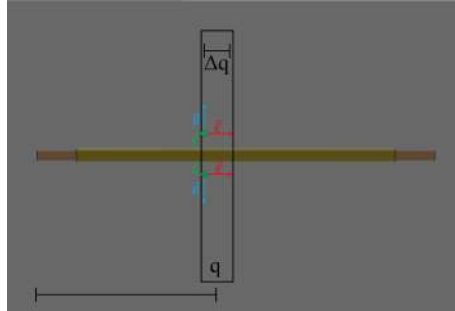
posed experimental method. The helical wire was included in this study to test the method for a more complex geometry that is often found in elongated implants.

For each measurement, one of the seven wires is soldered to the inner conductor of a partially stripped coax cable. This cable is attached to an ODU-connector with appropriate circuitry for coil identification. As such, this assembly can be used as a transceive antenna on a 1.5 T MR Scanner (Achieva, Philips Healthcare, Best, The Netherlands). The implants were positioned in an elliptical phantom (shown in figure 2.2B) filled with saline with conductivity $\sigma = 0.47$ S/m and with relative electrical permittivity $\epsilon_r = 78$. Copper(II) sulfate was added to the saline (5mM) to reduce T_1 therewith enhancing the SNR for the used MRI sequence.

For each implant 3D spoiled gradient echo MR images, with 1 mm isotropic resolution and $2°$ nominal flip angle to ensure the validity of the low flip angle approximation, were acquired. An example of a single slice is shown in figure 2.4 in the results section. The number of sample averages (NSA) was increased until sufficient SNR was reached upon visual inspection. The phase of the transceive field, was determined with two dual echo gradient sequences with opposite readout polarities to correct for eddy current contribution [62]. In order to maximize the SNR the echo times were kept as short as possible. The phase induced by main magnetic field inhomogeneities was corrected using the dual echo acquisition resulting in phase data that only included RF transmit and receive contributions [62].

The implant could easily be discerned in the acquired images (figure 2.4) and its spatial trajectory was determined with a MATLAB routine (The Mathworks, Natick, Massachusetts, USA). Along this trajectory the current distribution in the main magnetic field direction was determined with the two methods described in the previous section. The fact that the signal is proportional to the transceive field in the low flip angle regime, which in turn is squarely proportional to the current, is exploited by both methods.

In the BSM- method the exact wire positions where no signal originates from (due to the absence of phantom material) were masked from the MRI data. The wire was discretized in 3mm line segments whereas the imaging resolution was 1mm isotropic. Smaller line segments led to a worse conditioning of the BSM and larger segments led to a decrease in the resolution of the determined TF. Because the turns of the helical wire cannot be discerned accurately enough in the MRI data its coiled nature was not incorporated in the wire discretization
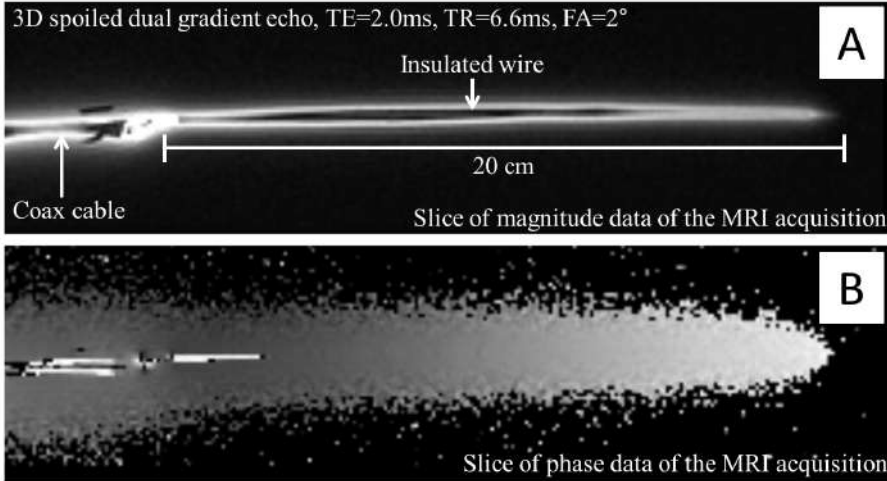
Figure 2.4: A slice of 3D spoiled dual gradient echo data (first echoTE¼2.0 ms) used to determine the transfer function. The magni-tude image (A) acquired with a 20cm insulated wire as transceiveantenna and the corresponding phase image (B).

for the BSM method and the helix was approximated as a linear structure. With this simplification, we effectively measure the current component in the z-direction.

In principle, each current segment will contribute to the signal in all K voxels in the imaging domain, but contributions to the more distant voxels are extremely small. If all contributions are taken into account the resultant maximally dense BSM has a high condition number because the contributions from current segments to voxels far away from these segments are dominated by noise. Therefore, to increase numerical stability, the calculation algorithm assumes that each current segment will only contribute to voxels in a sphere of influence of 3 cm around the corresponding line segment, effectively regularizing the BSM. In general, smaller cutoff radii led to a better conditioning of the BSM but meanwhile reduced the amount of information in the MRI data used for the reconstruction of the current distribution. With the regularized BSM a least-squares minimization was applied to determine the current distribution along the implant from the acquired MRI data which is the non-normalized transfer function.

In the LI-method a small part of the MRI data is used in the determina-

tion of the transfer function. Only the voxels in the square loop 5 mm away from the wire are taken into account and their sum is proportional to the square of the enclosed current that flows perpendicular to this surface. This method uses less MRI data than the BSM-method and is in principle more sensitive to the noise. This can be mitigated by computing and averaging several loops (provided that the noise in the data has zero mean which is true for the Gaussian distributed noise in the real and imaginary channel). Also for larger radii Maxwell's addition to Ampère's circuital law in Eq. (2.2) might become significant. The computed loop integral might no longer be purely determined by the enclosed current in the wire but instead may have a significant contribution from displacement currents. Therefore caution has to be taken when averaging loop integrals. Nonetheless, the LI-method relies on a forward calculation whereas in the BSM-method an inverse problem is solved. For this reason the LI-method faces less numerical difficulties and accompanying instabilities.

Results

In this section we will first show simulation results verifying the validity of the proposed experimental method. Simulated transfer functions are presented using the two simulation techniques, described in the methods section. These results are compared to transfer functions from literature [41], when available, to confirm the validity of both techniques. Secondly, MRI-based experimentally determined transfer functions using the two described post-processing techniques will be presented and compared with the simulation results.

Simulations

To compare the coax excitation method with the conventional PWE technique the transfer functions of implants were determined with both approaches in EM simulations as described in the methods section. The results of these simulations together with TFs known from literature are shown in figure 2.5.

The TFs of insulated and bare wires of various lengths that were determined with the PWE method are shown as dotted lines in figure 5. The transfer functions that were determined with the coax excitation method are depicted as solid lines. The agreement between results from both simulation methods is clear for the bare wires (fig. 2.5A), for the insulated wires (fig.2.5B) as well as for the helical wire (fig.2.5C). A small deviation between the results close to the tip of the implant is visible but still the magnitude of the complex Pearson correlation coefficient R between both simulation techniques is bigger than 0.98
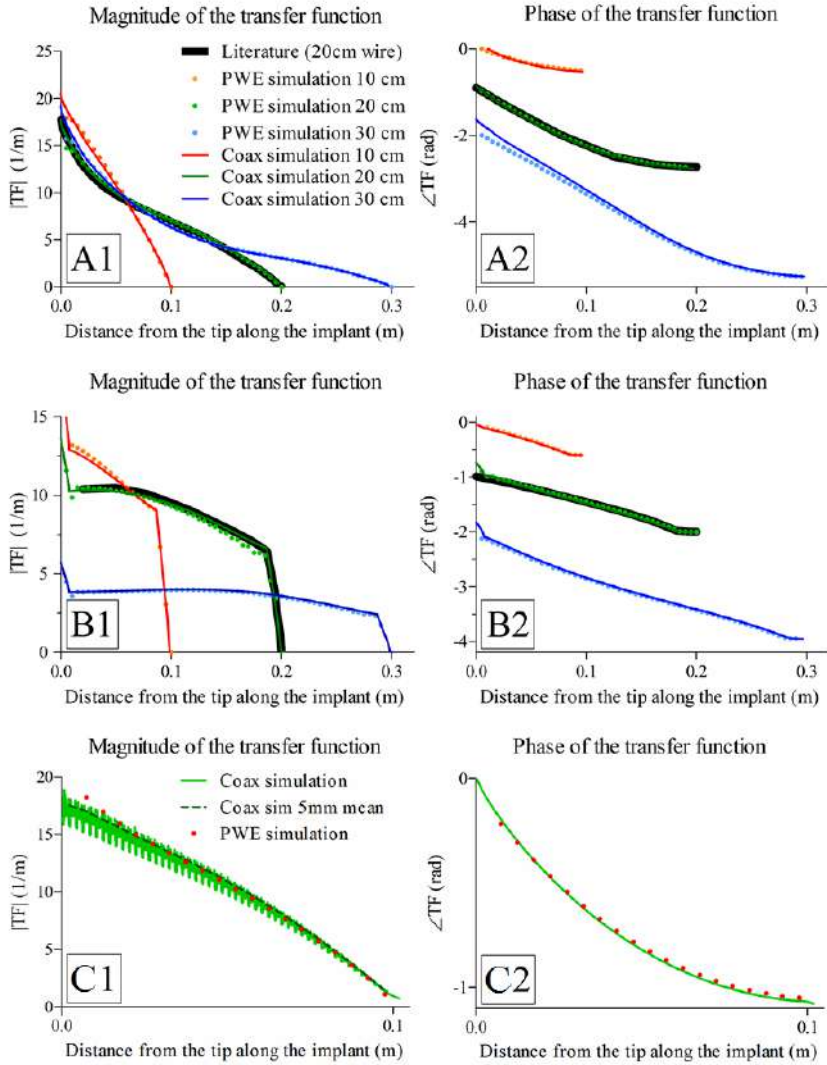
Figure 2.5: Comparison between simulated transfer functions determined with the Piece Wise Excitation (PWE) method, the coax excitation method and literature (8). The normalized magnitude (1) and phase (2) of the transfer functions of bare (A), insulated (B) and helical wires (C) show excellent agreement between both simulation techniques and literature.

for all implants. The simulation results likewise show excellent agreement to the transfer functions found in other studies [41, 59] represented as black lines in figure 2.5 (Only TFs of the implants of 20 cm were available from literature).

The affirmed agreement provides additional evidence of the suitability of the coax excitation method to determine the transfer function. The PWE method is in simulations as well as in experiments more cumbersome and time consuming. Hence the ascertained validity of the alternative reciprocal approach (shown before in [59]) can greatly benefit implant safety studies.

Table 2.1: Measurement durations and required field of views for the MRI acquisitions that were performed for the determination the transfer function of various implants. (a) This is the scan duration of two dual gradient echo 3D MRI acquisition performed with opposite gradient polarity.

Implant	FOV (AP, FH, RL) [mm]	Scan duration (3D dual GE) [s]	$TE_1/TE_2/TR$ [ms]	Imaging matrix (MxP)
10cm bare	(30,160,40)	792	1.9/3.5/7.4	240×240
20cm bare	(30,250,64)	1118	1.9/3.7/6.8	256×2256
30cm bare	(25,320,80)	1156	2.0/4.1/6.6	256×2256
10cm insulated	(43,150,40)	706	1.9/3.6/4.2	256×2256
20cm insulated	(36,250,64)	988	1.9/3.7/10	288×288
30cm insulated	(25,320,64)	1018	2.2/3.9/5.0	352×352
Helical	(29,250,64)	942	1.9/3.6/5.4	256×256

Discussion

This work has shown an alternative MR-based experimental method to accurately determine implant specific transfer functions in quick measurements. Dedicated bench setups with successive applications of localized electric fields, with the accompanying experimental challenges are no longer necessary. This alternative approach merely requires the implant to be used as a transceive antenna and allows for determination of its transfer function from the therewith acquired MRI data. The method was shown to accurately measure transfer functions of bare, insulated and helical copper wires up to 30 cm length in less than 20 minutes.

The presented method can be made faster by improving the antenna characteristics of the implant. The implant was used as a transceive antenna without performing any impedance matching and consequently showed high reflections. Improving the matching of the antenna will make larger flip angles accessible (keeping the validity of the low flip angle approximation in deliber-
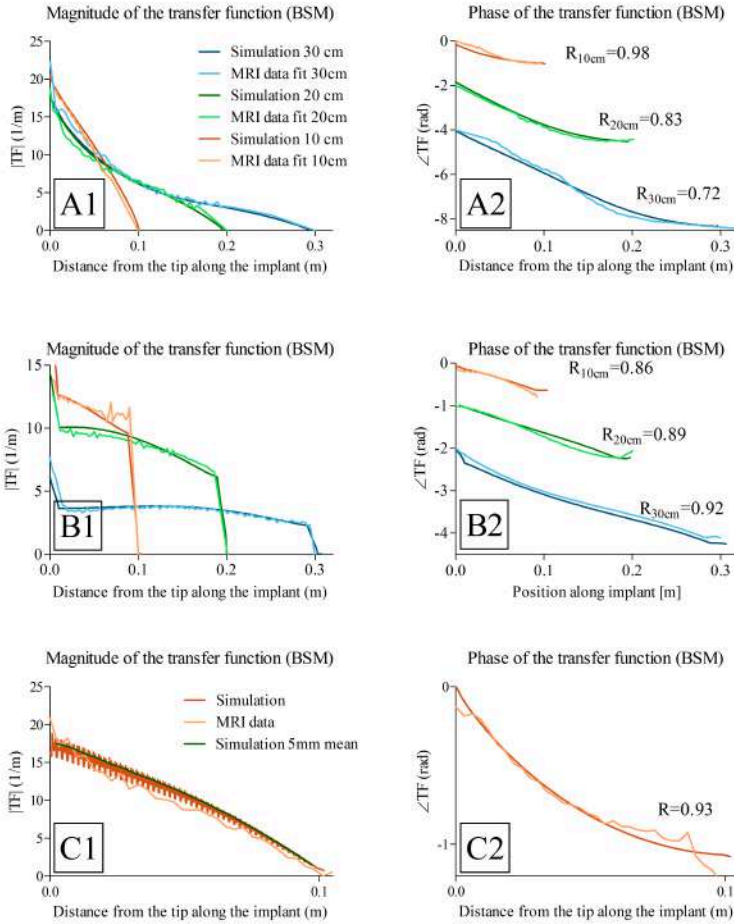
Figure 2.6: Transfer Function (TF) determined using the Biot-Savart Matrix (BSM) method showing the magnitude (1) and phase (2) of the normalized transfer function of bare wires (A), insulated wires (B) and a helical wire (C). The experimentally determined TFs (bright blue, green and orange) are in good agreement with the TFs from simulations (dark blue, green and orange) with a coax excitation that correspond to the solid lines in figure 2.5. The phase profiles are depicted with an offset from each other for clarity. For the helical wire the 5mm mean of the current distribution is also displayed, which corresponds to the TF determined with the PWE method.
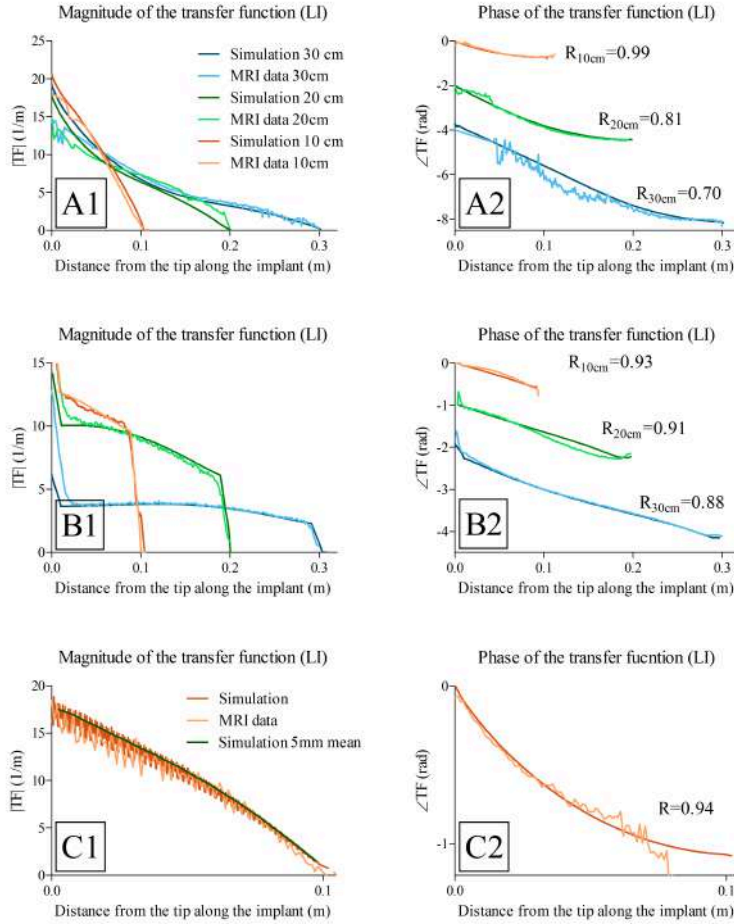
29

Figure 2.7: Transfer Function (TF) determined using the Loop Integral (LI) method showing the magnitude (1) and phase (2) of the normalized transfer function of bare wires (A), insulated wires (B) and a helical wire (C). The experimentally determined TF (bright blue, green and orange) are in good agreement with the TFs from simulations (dark blue, green and orange) with a coax excitation that correspond to the solid lines in figure 2.5. The phase profiles are depicted with an offset from each other for clarity. For the helical wire the 5mm mean of the current distribution is also displayed, which corresponds to the TF determined with the PWE method.

ation) and thereby increase SNR. This will make an MRI acquisition possible with less NSAs and thus reduce its duration. The flip angle was kept low as a precaution to avoid any issues with high reflected powers reaching the RF amplifier system. These reflections can be mitigated with a matching network. The effect of a matching network on the transfer function has to be investigated before this improvement can be made and caution is necessary.

The poor matching of the transceive antennas is actually consider to be beneficial for the accurate determination of the transfer functions, because this ensures that only a small fraction of the current induced in the implant can run back into the coax cable. If the matching is better the implant and coax cable can no longer be seen as two approximately separate systems, which could lead to a misrepresentation of the transfer function. So if matching is used to speed up the measurements, corrections for the alterations of the transfer function need to be developed. This beyond the scope of this paper and therefore we kept using poorly matched antennas (60-80% reflected power).

Another, more easily implementable, way to increase the SNR and hence speed up the acquisition is to employ the implant as transmit antenna but receive with another local element. This requires the receive field to be either known or homogeneous across the acquisition domain. This improvement was not realized because the scanner software only allowed local receive antennas in combination with body coil transmit to be used but not a local transmit element in combination with a separate receive array. Both suggested improvements can drastically speed up experimental determination of TFs.

The MRI measurement of the TF for more elongated implants requires increasing the field of view of the MRI scanner beyond the range of acceptable B_0 homogeneity and reliable gradient performance. The TFs of longer structures can still be determined by combining data from various scanning positions or by bending the structure to entirely fit in a reliable field of view. Bending of the implant away from the z-direction reduces the contribution of the induced current to the transceive field which reduces the sensitivity of the procedure for the non-axially aligned parts. Despite these practical challenges the described method can be used to determine the TF of a structure of any length.

Besides practical considerations numerical instability associated with solving the ill-conditioned linear least squares minimization in the BSM-method can arise. The LI-method does not face these mathematical problems. It however uses less of the acquired MRI data to determine TFs. Only the voxels
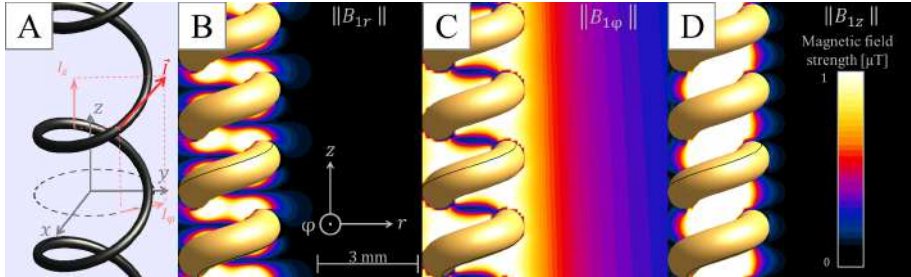
Figure 2.8: Figure 8 To discern between B1-field contributions from the longitudinal, I_z, and azimuthal, I_ϕ, current components in the helix, the cylindrical B_1-field components are depicted in a plane bisecting the helix. In this plane, the r- and z-component of the B_1-field are generated by the azimuthal current component in the helix; the ϕ-component of the B_1-field is generated by the longitudinal current component in the helix. The r- and z-components of the B1 field generated by the azimuthal current in the helical wire drops of quickly due to the cancelation of contributions from neighboring windings. The ϕ-component of the B_1 field generated by the longitudinal current component does not cancel and generates a measurable MR signal. Just 1.5 mm away from the helix the strength of the transverse B1 field generated by the azimuthal current component is about twenty times smaller than the transverse B_1 field generated by the longitudinal current component.

that contribute to the loop integral 5 voxels away from the wire are taken into account and for this reason this method is more sensitive to noise. The reduction in the number of voxels used for the computation of the transfer function is also the underlying reason why it performs less adequate for the bare wires and the helical wire where the SNR is lower compared to the insulated wires. It even outperforms the BSM-method for some wires, but overall the performance of the LI and the BSM method is comparable. One could improve the LI method by performing the integration for various sized loops in parallel and average over the outcomes. However, some caution is needed to avoid to large loop radii. From simulations the contribution of displacement currents is determined to stay below 10% for a loop less than 5 mm away from the wire. The size of this contribution is dependent on the frequency of the RF fields and the permittivity of the phantom material.

Scan-parameters

Concerning helical wires, it might be required to clarify why the MR signal can be used for TF determination. The current in helical structures can be decomposed into a longitudinal and an azimuthal component (figure 2.8a). The azimuthal current component generates a B_1 field around the wire that is both longitudinal, and radial (note the omission of superscript plus or minus

because B_1 denotes the total RF magnetic field and not only the clock wise or counter clock wise rotating component). The radial component adds to the transverse component of the B_1 field and would therefore also be in principle measurable. Indeed, in the direct vicinity of the wire, the radial component is significant. However, the spatial extension of the radial component outside the helix is negligible. This effect is visible in figure 2.8b where at 1.5 mm the radial component becomes negligible and is caused by cancellation from neighboring windings. The radial component decays faster if the helix is more tightly wound and always negligible for the typically densely wound helices used in implants. Note that also the longitudinal B_1 field component does not extend outside the helix (figure 2.8d) although the MR based method is inherently insensitive to it anyway. Therefore, only the azimuthal B_1 component will lead to a measurable contribution to the MR signal for realistic helical implants enabling the MR based measurement of the longitudinal current component via the same principles as for straight wires.

Only measuring the longitudinal current component in the helical wire gives an underestimation of the total current which may be considered a short-coming. However, the same holds for the existing TF measurement methods. The method using the principle of reciprocity [59] measures the longitudinal E-field component along the helix and is therefore likewise only sensitive to the longitudinal current component. This is equivalent to the PWE method where only the longitudinal component of the tangential electric field effectively induces a current along an implant. Note that also for realistic E-field exposures on realistically helically shaped implants in MRI, only the longitudinal component of the electric field can effectively induce a current along the helix (because the wavelength is large with respect to the helix diameter, the E-field along the azimuthal component will integrate to zero over a single winding of the helix).

One could argue that a measurement of the current in the implant excited with a coax cable by using MRI is an overcomplicated way to determine TFs. A transducer allows for more straightforward current measurements and determination of TFs and does not require the use of an MRI scanner. From a certain perspective this claim is correct but using a transducer still does not evade the necessity for successive measurements that requires exact positioning and measuring localized currents. Furthermore, it is only possible to subsequently reposition a transducer in liquid phantoms.

Using an MRI scanner makes it possible to determine the TFs in gels,

heterogeneous media and even animal or human tissues allowing various more realistic loading conditions to be investigated. As long as the material in which the implant is used as a transceive antenna produces sufficient MRI signal the transfer function can be determined. For heterogeneous media changes in proton density might affect the determined transceive sensitivity and subsequently influence the determination of induced currents. Therefore, B_1^+ mapping techniques and a correspondingly altered version of the BSM-method could be used for determining transfer functions in heterogeneous media. In this way the proposed method is a step towards pre-MRI-examination or on-site safety assessment for patients with an AIMD.

If the method described in this paper can be extended to determine transfer functions of implanted medical devices embedded in patients a low power pre-scan can be designed for patient specific safety assessment. This would facilitate relaxation of the safety limits for implants with an MRI conditional label and enable cautious safety assessment for implants without MRI label. On site safety assessment is a step toward making MRI more widely available for the growing group of patients with an AIMD.

Conclusion

We have presented an experimental method to determine transfer functions of elongated implants accurately using MR imaging techniques. The remaining differences between experiments and simulations result in a maximum deviation of $\Delta E_{tip} \leq 11\%$ and $\Delta E_{tip} \leq 19\%$ for the BSM and LI method respectively, as determined from the area under the curve of the magnitude of the transfer function. The proposed method is relatively quick (<20 minutes) and has a high spatial resolution (3 mm and 1 mm). This method can greatly expedite the experimental studies for RF safety assessment of implantable medical devices. Both simulation and experimental results show that the conventional methods to measure TFs by sequentially applying a localized electric field while monitoring the field around the tip of the elongated implant can be replaced by applying a field at the tip and monitoring the response throughout the implant. The proposed MR-based method allows for TF determination of implants embedded in realistic surrounding media, such as test animals or corpses.

Acknowledgments

MR based, wireless determination of the TF of a linear implant: introduction of the transfer matrix

Tokaya, Janot P.

Raaijmakers , Alexander J.E.

Luijten , Peter R.

van den Berg, Cornelis A.T.

Abstract

Introduction: We introduce the transfer matrix (TM) that makes MR-based wireless determination of transfer functions (TFs) possible. TFs are implant specific measures for RF-safety assessment of linear implants. The TF relates an incident tangential electric field on an implant to a scattered electric field at its tip that generally governs local heating. The TM extends this concept and relates an incident tangential electric field to a current distribution in the implant therewith characterizing the RF response along the entire implant. The TM is exploited to measure TFs with MRI without hardware alterations.

Materials & Methods:A model of rightward and leftward propagating attenuated waves undergoing multiple reflections is used to derive an analytical expression for the TM. This allows parameterization of the TM of generic implants, e.g., (partially) insulated single wires, in a homogeneous medium in a few unknowns that simultaneously describe the TF. These unknowns can be determined with MRI making it possible to measure the TM and, therefore, also the TF.

Results: The TM is able to predict an induced current due to an incident electric field and can be accurately parameterized with a limited number of unknowns. Using this description, the TF is determined accurately (with a Pearson correlation coefficient R$\geq$0.9 between measurements and simulations) from MRI acquisitions.

Conclusions: The TM enables measuring of TFs with MRI of the tested generic implant models. The MR-based method does not need hardware alterations and is wireless hence making TF determination in more realistic scenarios conceivable.

Introduction

An ever-growing part of the population is carrying active implanted medical devices (AIMDs). These people are often not eligible for MRI investigations because the scanner interacts with the AIMD through its electromagnetic fields potentially resulting in harm to the patient. The most pressing concern is that the AIMD may be able to locally enhance the radiofrequency (RF) fields of the MRI scanner. This can cause a local temperature hotspot with possibly severe consequences [28]. Many factors influence the extent of the heating [25,34,63–65] making it difficult to predict the occurrence of hazardous situations. This leads to many implants being considered a contraindication for MRI. Withholding these patients from such a diagnostically powerful image modality is unfortunate and hence RF heating is a topic of ongoing research. Likewise, implant manufacturers develop more and more products that can be used safely in an MRI-scanner provided exposure conditions specified in a conditional label are met.

For this purpose, a technical specification [53] has been formulated that provides a consistent testing methodology for implant manufacturers on how to assess the RF safety of implantable medical devices under MRI conditions. A four tier approach is described in this technical specification. The highest (fourth) tier performs the analysis with lowest amount of assumptions or simplifications allowing minimization of the overestimation of safety margins on relevant MR parameters such as for example the specific absorption rate (SAR). The cost is however, an enormous set of numerically expensive simulations comprised of a vast selection of realistic implant positions in numerous human models to build a statistical basis for a prediction of an expected worst case heating. It involves accurate modeling of the often submillimeter details of the implant in a comparatively large volume of an MRI body coil. This combination will in many cases lead to prohibitive calculation times and/or extensive computational power.

The other tiers make use of the transfer function (TF) concept of the implant [41] and rely on the usually localized nature of heating. The normalized TF is an implant characteristic that relates an incident tangential electric field distribution along the trajectory of a linear implant to the resultant, enhanced electric field (often around the tip) of the implant, which drives local heating. In fact, the most significant field enhancement does not necessarily occur at the tip. The active implantable medical devices considered in this paper typically contain an insulated wire having one or more electrode poles in contact with human tissue to deliver therapeutic currents. RF currents can

37

be induced on these conductive structures during an MRI exam that result in energy deposition nearby these poles. Since the poles are most often located near the tip of these implants, this type of heating is often referred to as tip heating. In this work we employed linear, (partially) insulated structures as a surrogate model that are characterized by similar RF current induction and also demonstrate tip heating. The TF simplifies computations because it decouples the assessment of the local scattered field (requiring detailed modeling of an implant) from the incident field (a characteristic of the comparatively large MRI system).

This function can be determined by monitoring the response of an implant to piece wise, localized electric field exposures with dedicated bench setups [42]. Recently, based on the principle of reciprocity an alternative approach has been presented that interchanges the exposure and monitoring locations [59]. This finding triggered the idea of MR based TF determination [66]. For this method, a coax cable is soldered to the implant which is used as a transmit/receive antenna in a phantom during MRI experiments. From the resulting images, the current distribution along the implant is determined that directly reflects the TF. This MR based methodology has the advantage that the TF can be determined without dedicated bench setups. The required galvanic contact however limits the practical applicability of the method and potentially perturbs the TF of the implant.

To avoid this physical alteration to the implant this paper aims to use a regular MRI RF transmission technique (i.e. using the birdcage body coil for transmit). When E-fields arising from the birdcage body coil impinge upon an implant, they excite a current that can be measured by an MRI experiment. This, effectively, enables the determination of the TF of the implant. However, contrarily to other experimental methods [42, 59, 66] the resulting E-field excitation is not localized at the tip and therefore the induced current distribution will not directly reflect the TF. Nevertheless, the transfer function (or its generalization, i.e. the transfer matrix introduced here) describing the current induction in an implant due to a tangential electric field, can be derived from the combined information contained in the incident E-field and the induced current.

This work will show how a standard MRI measurement is also able to provide the transfer function for an implant-like structure in a standardized test phantom. For this purpose, we will employ a description that is a generalization of the TF. This extension, called the transfer matrix, relates an incident electric

field distribution along the implant to the resultant current distribution over the entire implant instead of a single point. This generalization is necessary because the body coil excites the implant over the entire length and the excitation is not confined to the tip of the implant anymore as was originally assumed in the reciprocal approach for TF determination [59]. With the assessment of the transfer matrix, the TF is simultaneously determined A test setup with known properties has to be used as this enables the determination of the incident electric field by means of electromagnetic simulations.

The transfer matrix can be determined through a Greens function approach by application of localized excitation at a range of positions along the implant and measurement of the current distribution along the implant for each excitation position. This is possible in simulations, but is not feasible in an MRI setting. In fact, normally only one incident E-field distribution can be applied and only one current distribution along the wire can be measured. However, it will be shown for implant-like structures that the transfer matrix can be parameterized by an analytical model, depending only on a few unknowns (6-10 unknowns for the cases considered in this work) that determine the entire matrix. The parameterization is derived for bare and (partially) insulated wires embedded in a homogenous dielectric. The application of this model provides a drastic reduction of the number of unknowns in the TM making it possible to determine it with conventional MRI measurements.

Firstly, this parameterization of the TM will be derived in the theory section based on a model of converging sums of attenuated back and forth reflected waves. Secondly, the theoretical description will be validated with simulation results. After this, the feasibility of measuring the transfer matrix with MRI-measurable quantities is demonstrated by extracting these quantities from simulations. Lastly, the actual MRI-based transfer matrix assessment is demonstrated experimentally for two generic structures similar to ones used when the TF was first introduced in the context of RF safety [41]. It should be noted that these generic structures do not resemble any realistic implant that are often much more complex. However for a proof of principle of the method presented here these generic structures suffice. The result is an MRI method that can assess the TF of a medical implant in a standardized phantom without the need for a galvanic contact to the implant.
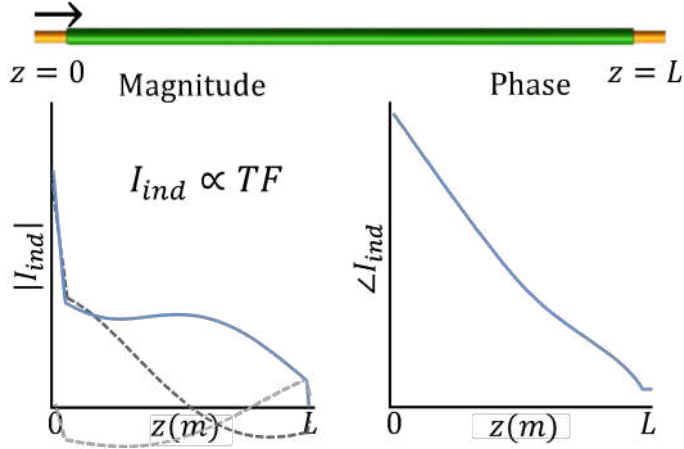
Figure 3.1: The real part of the first induced and reflected wave due to an excitation at the tip of the implant are shown as dashed lines in the left plot. The sum of these waves converges to the transfer function of which the magnitude (left) and phase (right) are shown as solid blue lines. They are the first column of the transfer matrix, M.

Theory

A simplified model

We will start with a theoretical treatise of a one-dimensional implant model. It is composed of a single metallic wire of length L embedded in a homogenous, lossy dielectric. If the implant is exposed to a localized, discretized RF electric field, a propagating, electromagnetic wave along the implant will be induced.

If the electric excitation incident at the tip of the implant, i.e. at $z = 0$ behaves as an infinitesimal field source the current distribution in the wire will reflect the transfer function [59]. An example of such a current distribution for a partially insulated wire is shown in figure 1. This 'tip excitation' will initially create an electromagnetic wave resulting in a current of magnitude $\sigma_{eff} A E_0$ that propagates towards the opposite end of the wire at $z = L$ and subsequently will reflect leftward. At z=0 it will be reflected in the opposite direction again. The complex reflection coefficients at the ends of the wire at $z = 0$ and $z = L$ will be called Γ_0 and Γ_L respectively. This repetitive process results in ever smaller wave amplitudes due to attenuation upon propagation

through the implant. The sum of these waves is given by,

$$I(z) = \sigma_{eff}AE_0(e^{-c_1 z} + \Gamma_L e^{c_1(z-2L)})$$
$$\left(1 + \Gamma_0\Gamma_L e^{-2c_1 L} + (\Gamma_0\Gamma_L e^{-2c_1 L})^2 + ...\right) \tag{3.1}$$

Here c_1 is the complex wave number that describes the propagation of the electromagnetic wave through the implant. A is a proportionality factor with the dimension of a surface determined by the effective cross-sectional area of the implant. σ_{eff} is the effective conductivity that is governed by local loading conditions of the implant and relates the incident electric field, E_0, to an induced current. The geometric series in this equation bears similarities with summations often employed in the field of optics [67]. It converges to $(1 - \Gamma_0\Gamma_L e^{-2c_1 L})^{-1}$ [68]. The resultant function is a standing wave that parameterizes the transfer function of an implant in the aforementioned four complex unknowns, i.e. the wave number c_1, the effective conductivity σ_{eff} and the two reflection coefficients Γ_0 and Γ_L. For a detailed derivation of equation 1 the reader is referred to the appendix A. Figure S1 in appendix A displays the first view waves of the geometric series.

Note that c_1 and σ_{eff} are complex constants as long as the implant is embedded in a homogeneous medium. If the electromagnetic properties of the environment around the implant vary along its length these quantities will be position dependent. This will increase the complexity of the model and not be addressed here. These two parameters as well as Γ_0 and Γ_L will be dependent on the characteristics of the implant and on the electromagnetic properties of its environment. For more complicated structures a similar analysis will yield comparable equations with additional unknowns. The accuracy of this model to represent transfer functions will be demonstrated in the results section.

However, in this work we aim to extend the concept of the one-dimensional TF towards a two dimensional transfer matrix (TM), which is required to measure the TF with MRI experiments. This extension is necessary because during an MRI exam the incident electric field is not confined to the tip of an implant but distributed along its entire length. In this situation each position on the implants becomes a source for induced currents. The net induced current is the superposition of all these individual induced currents and can be described by the multiplication of the transfer matrix and the tangential, incident electric field vector. Therefore, we assume that the excitation does not occur at the tip of the implant, i.e. at $z = 0$, but at some arbitrary location $z = z_j$. It will have a complex value $E(z_j)$. For all practical

purposes this excitation will have a certain finite width, that will determine the resolution in which the TM and TF are rendered. The derivation of the TM will be continued in this discretized space. The excitation will create both a rightward and a leftward propagating (primary) electromagnetic wave with respect to the excitation that induces currents described by,

$$I_p(z_i, z_j) = \sigma_{eff} A E_0 e^{-c_1 |z_i - z_j|}. \tag{3.2}$$

These primary (i.e. primary in this case indicates a wave that is not reflected) rightward and a leftward propagating waves will again be repeatedly reflected at either end of the implant. The total sum of waves will be (see appendix A for the details on this derivation):

$$M(z_i, z_j) = \frac{I_p}{E(z_j)} + \frac{\sigma_{eff} A}{1 - \Gamma_0 \Gamma_L e^{-2c_1 L}} \left(2\Gamma_0 \Gamma_L e^{-2c_1 L} \cosh\left(c_1(z_i - z_j)\right) + \right.$$
$$\left. \sqrt{\Gamma_0 \Gamma_L e^{-2c_1 L}} \cosh\left(c_1(z_i - z_j - L) - \frac{1}{2}\ln(\frac{\Gamma_0}{\Gamma_L})\right) \right). \tag{3.3}$$

This two-dimensional function when multiplied with an electric field distribution incident on a wire gives the current distribution along this wire. For three different excitation positions the induced currents are shown in figure 2.

If an incident electric field distribution is known up to a certain resolution along the length of the implant, $E_{inc}(z_j)$, the resultant induced current distribution throughout the implant is computed through a simple matrix vector multiplication, $I_{ind}(z_i) = M(z_i, z_j)E_{inc}(z_j)$. The transfer matrix describes the RF response of an implant to an electric field exposure with four, in general unknown, complex quantities, c_1, σ_{eff}, Γ_0, Γ_L , and two known parameters L and A (these parameters also define the TF). This parameterization of the TM will be referred to as the attenuated wave model.

The attenuated wave model can be extended to incorporate more complex structures that consist of multiple electromagnetic domains, e.g. partially insulated wires. Additional unknowns will be necessary to describe the current distributions in these structures but still with a limited number of parameters, they can be modeled with equations similar to equation 3.3. An extension of the theory for an implant that contains impedance transitions is given in Appendix A.
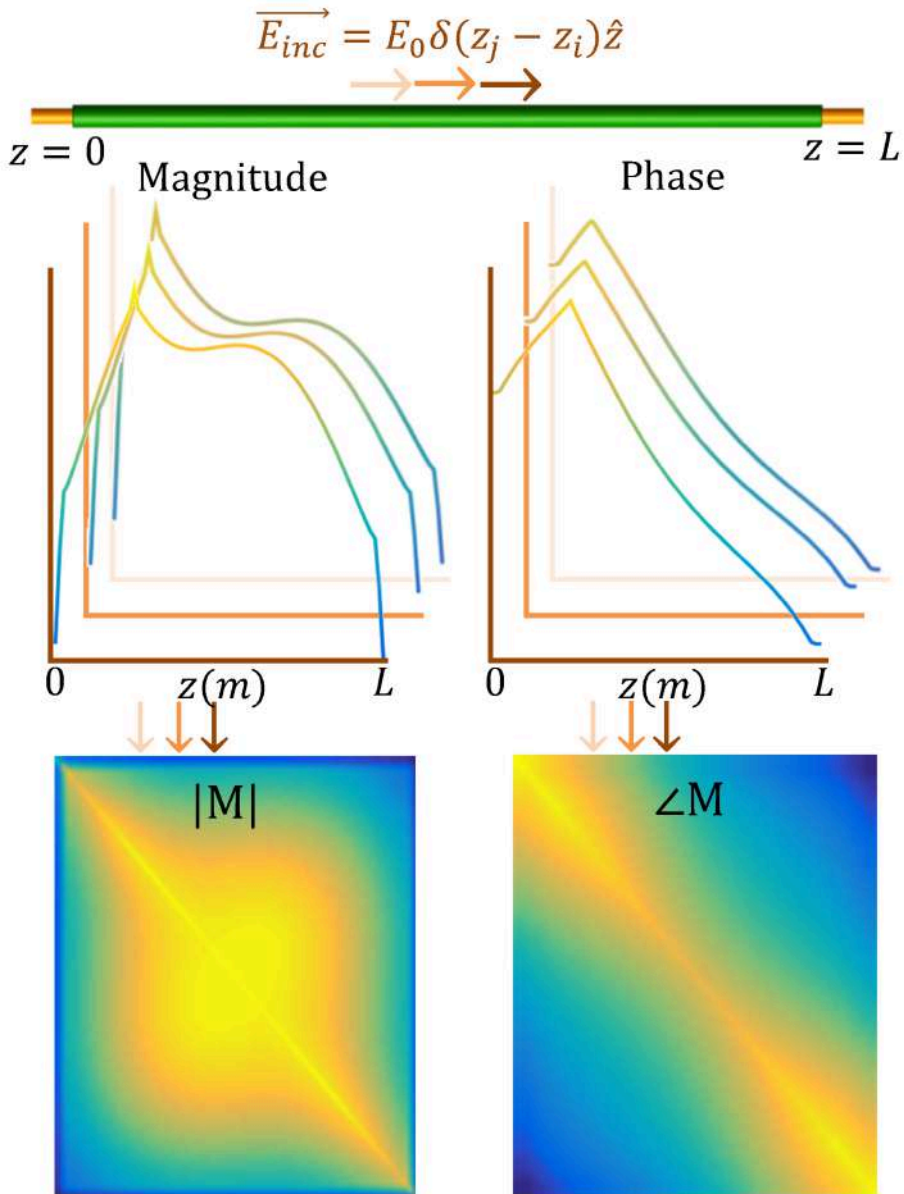
Figure 3.2: Excitations at various locations along the implant induce various current distributions. Three examples are shown as solid colored lines. These current distributions form the columns of the transfer matrix, M. The TF is the first column of the transfer matrix [59]

The transfer function is contained in the transfer matrix.

The current distribution in an implant excited by an electric field at the tip of the implant is described by its transfer function [59]. Exciting the implant at its tip is equivalent to choosing z_j to be zero in its transfer matrix. So,

$$S(z_i) \propto M(z_i, 0), \tag{3.4}$$

because this means the excitation occurs at $z_j = 0$, i.e. the tip of the implant. As a consequence, once the transfer matrix of an implant is known so is its TF.

Methods

With the attenuated wave model the TM and the TF are described by a limited number of unknowns. Given a known, incident electric field and a (measured) resultant current in the implant, the TM can be determined through the following minimization,

$$\underset{c, \Gamma_0, \Gamma_L, \sigma_{eff}}{\operatorname{argmin}} \| M(z_i, z_j; c, \Gamma_0, \Gamma_L, \sigma_{eff}) E_{inc} - I_{ind} \|. \tag{3.5}$$

We will start with verification of the applicability of the attenuated wave model to describe TMs (and TFs) with a limited set of model parameters through simulations. Then, the measurability of the transfer matrix by MRI acquisitions is tested by reconstructing it from MRI accessible quantities. Finally, the actual MRI measurement is performed to determine the TM of two structures representative for implant leads. The $|B_1^+|$ and transceive phase (the sum of the transmit and receive phase) distributions [69], are measured, and used together with a characteristic of the experimental setup, i.e. the incident electric field E_{inc}, to determine the TM.

Verification of the analytical TM description.

To test the validity of the attenuated wave model, the transfer matrices of four implant structures, shown in figure 3.3, were calculated using numerical electromagnetic simulations. Implant A is a bare wire with a length of 20 cm and 2.5 mm diameter for which the reflection coefficients Γ_0 and Γ_L should be equal. Structure B is the same wire but ended on one end with a cube of perfect electric conductive material with 4 cm edges intended to change Γ_L. Implant C is composed of an 8 cm insulated region and a 12 cm bare region and hence contains an impedance transition. Wire D is insulated except for 1cm at both ends. The insulation, of 0.5mm thickness, has a relative permittivity of 3 and is non-conductive. The conductive parts of the wires are composed of copper

with a conductivity (at 64MHz) of $5.8 \cdot 10^7$ S\m and a relative permittivity of 1.

These generic structures were used as test implants because their TMs and TFs will have an increasing level of complexity. Furthermore, the bare and insulated wires have known electrical properties and have been used in other works on transfer functions determination [41, 59, 66] thus facilitating benchmarking. All the structures were embedded in a dielectric with a relative permittivity of 77 and a conductivity of 0.35 S\m that filled the entire computational domain. The phantom filling liquid used in experiments was designed to have the properties of the high permittivity medium [70] that is global average of biological tissues at 64Mhz. It was measured to have the before mentioned somewhat different properties that were subsequently used in simulation.

For all these structures, the TM was determined by harmonic FDTD simulations (Sim4Life, ZMT, Zurich, Switzerland) with a simulation time of 20 periods and a -50dB auto termination condition by application of a localized electric field excitation on the implants. The localized excitations are realized with thin (5mm) electromagnetic plane wave boxes, which is a straightforward method to determine the transfer function by simulations [66]. Two counter propagating plane wave box sources of 10 x 10 x 0.5 cm^3 with opposing magnetic and aligned electric fields are applied as incident waves on the implant,
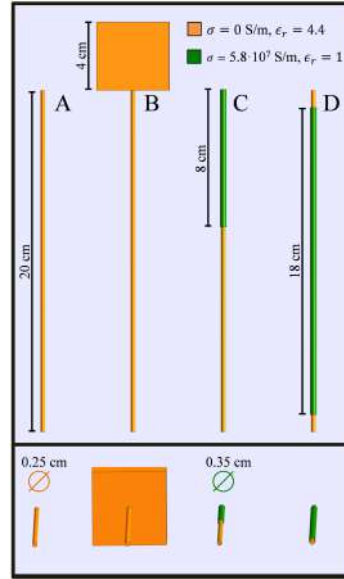

Figure 3.3: The CAD models of the generic structures that are used in simulations to assess the descriptive potential of the TM. Structure A is a bare copper wire of 20 cm length. Structure B is a bare copper wire of 20 cm length that is attached to a PEC block on one end to alter one reflection coefficient. This would for example be the case if a lead is attached to an IPG. Structure C is a copper wire of 20 cm length with 8 cm of insulation. Structure D is an insulated copper wire with 1 cm of insulation stripped from either end.

which is gridded with 0.2 mm isotropic resolution perpendicular to the long axis of the implant and 0.5 mm resolution along the long axis. This setup of plane wave sources ensures the implant is exposed to a purely tangential electric field excitation localized at one specific position z_j along the implant

structure. These simulations with two counter propagating plane wave box excitations will be called piecewise excitation (PWE) simulations throughout this paper.

The TM can be determined from a full set of PWE simulations, i.e. a set of simulations with plane wave excitations at subsequent, discretized locations such that the full length of the implant is covered. For a single PWE simulation the current in the implant is induced by a localized electric field excitation at location, z_j. The current in the wire is computed from the volume current density and discretized with steps equal to the separation between excitation centers. This discretized current is used to fill the z_jth row of the TM, creating a square matrix. Combining the full set of PWE simulations the entire TM can be filled column-wise. The hereby realized TM will be considered the ground truth. We use this benchmark to determine the ability of the attenuated wave model to accurately describe realistic transfer matrices. The parameters of the attenuated wave model ($c_1, c_2, \Gamma_0, \Gamma_L, \sigma_{eff}$) are determined through a nonlinear least squares fit to the PWE simulation results using MATLABs lsqcurvefit (MathWorks, Natick, MA). The resulting fitted transfer matrices are compared to the simulated ground truth matrices to verify the applicability of the attenuated model.

Experimental TM determination.

As an initial test of the proposed MR based TF determination method an idealized version of theexperiment was simulated (figure 4.4) including models of the birdcage coil and phantom setup. A harmonic FDTD simulation of a 16 rungs high pass birdcage coil tuned to 64MHz with 35.2 cm coil radius and 42 cm rung length driven in quadrature mode with two voltage sources (IQ-feed) loaded with an elliptical phantom was performed. The RF shield with a radius of 37.2 cm and length of 70 cm was composed of perfect electric conductor. The simulations of the birdcage coil had a simulation time of 50 periods. The elliptical phantom has walls (11mm thick) composed of PMMA and is filled with a dielectric (9cm filling height), with relative permittivity of 77 and a conductivity of 0.35 S\m. A simulation with and without an implant, is performed to compute the electric field incident on the implant and the induced current respectively. This incident electric field distribution is also used for experimental determination of the TM. The implants have the same electromagnetic properties and dimensions as described in the section on the piecewise excitation method. The phantom and wire position were retrospectively matched to the experimental setup by importing the acquired
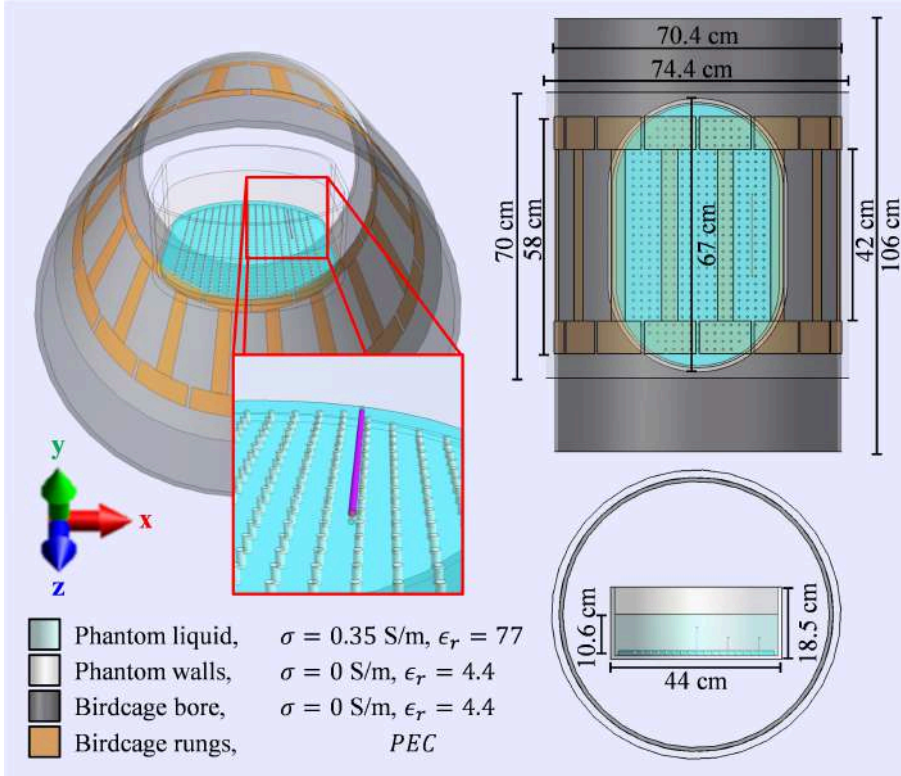
Figure 3.4: The CAD models used in simulations to mimic the performed experiment with the E-field exposure generated by 1.5T RF body coil that is used in experiments. The wire trajectory and phantom position were altered slightly to match their respective experimental locations using the acquired MRI data, with the exception that the wires were always assumed to be perfectly aligned with the z-axis.

MR images in the simulation domain. In experiments, it was attempted to place the phantom in the center of the birdcage and the implants were placed 10 cm away from the center of the birdcage coil in the x-direction submerged under 4 cm phantom liquid.

As long as the incident electric field distribution tangential to the implant, E_{inc}, is known and the resultant current distribution, I_{ind}, through the wire can be measured using MRI, the transfer matrix can be determined through the minimization given by equation 3.5. In this minimization, the transfer matrix M is described by the attenuated wave model and characterized with parameters c,Γ_0,Γ_L and σ_{eff}. The output of the minimization are the model parameters that best describe the complete transfer matrix M. The electric field exposure, E_{inc}, is a fixed characteristic of the measurement setup and does not depend on the implant being examined.

In an actual MRI acquisition the distribution of $|B_1^+|$ and the transceive phase(61) are measurable. The distributions of these quantities in the vicinity of a wire can be used to determine the current [45, 55, 71, 72]. The incident electric field distribution is obtained from simulations.

The simulations approximating the actual MRI experiment were validated by comparison of the $|B_1^+|$ and transceive phase distribution in the phantom without an implant. Therefore, the B_1^+ magnitude distribution was experimentally determined with a 3D dual TR actual flip angle (AFI) acquisition [73] with 7x7x5 mm voxel size and a 30ms TR extension on an initial repetition time of 9.1ms on a 1.5 Tesla Philips Ingenia MR scanner (Philips Healthcare, Best, The Netherlands). With a field of view (FOV) of 140x300x450 mm (APxFHxRL) and 4 signal averages, this acquisition took 192 seconds. The transceive phase was determined by the average phase of two 3D spoiled gradient echo acquisitions with opposing gradient polarities to correct for eddy current contributions [5] and potential timing inaccuracies [74]. The signal contributions from the receive array were removed using homogeneity correction with a coil sensitivity maps acquired in a reference scan. This ensures only transmit and receive sensitivities from the birdcage coil are present in the acquired data. The phase acquisitions have the same geometry as the AFI acquisition. Five echoes were acquired and used to correct for unwanted phase contributions from B_0 inhomogeneities [62] that grow linearly in time. The resulting complex B_1^+ distribution without an implant present is used to validate equivalent simulations without an implant present. From these simulations, the incident electric field is determined.

In addition to the incident electric field, the induced current in the wire needs to be determined. The current is calculated from the $|B_1^+|$ distribution in the phantom with one of the implants present. These distributions were determined with the variable flip angle method [75, 76] as this technique is better able to capture the large range of $|B_1^+|$ values present in the case of the wire immersed in the phantom at the expense of extra acquisition time. For this purpose a large range of 3D spoiled gradient echo images with various nominal flip angles [45] were acquired. The spoiled gradient echo images had the same FOV as the AFI acquisition but a smaller voxel size of 1.9x1.9x5 mm to capture the rapid decay of the $|B_1^+|$ enhancement around the wire. The nominal flip angles were 0.25, 0.5,1, 2, 3, 4, 6, 10, 13, 16, 19, 22, 25, 30, 50, 75, 90, 120 degrees. The acquisitions had a repetition time of 30ms leading to scan duration of 123s per scan. From these acquisitions the $|B_1^+|$ was determined by fitting the signal from spoiled gradient echo acquisitions as function of flip angle to the data on a voxel by voxel basis [45] using the following equation:

$$\mathcal{S}(\vec{r}) = \frac{C_1(\vec{r})(1 - e^{-TR/T_1})\sin(C_2(\vec{r})FA)}{1 - e^{-TR/T_1}\cos(C_2(\vec{r})FA)}e^{-TE/T_2^*}. \qquad (3.6)$$

Here $C_1(\vec{r})$) is proportional to the receive sensitivity and $C_2(\vec{r})$ is proportional to the $|B_1^+(\vec{r})|$ distribution. The relaxation times were fixed parameters in the signal fit that were determined with a simultaneous multi spin echo interleaved with inversion recovery sequence [77]. Subsequently an annulus of $|B_1^+(\vec{r})|$ data around the wire was used to fit the $|B_1^+(\vec{r})|$ artifact resulting from the interference of the complex magnetic fields due to the current and the background B_1^+ field. From the measured $B_1^+(\vec{r})$ field modification, the current distribution along the wire is deduced. The phase difference between the B_1^+ magnetic field produced by current and the background B_1^+ field also follows from this fit. This difference in combination with the experimentally determined transceive phase distribution is used to compute the phase of the current. More details on this procedure can be found in appendix A and B (and supporting figures S1 and S2).

Using the experimentally determined induced current distribution and the matched incident electric field distribution from simulations, the TM can be computed with equation 3.5 similarly as was achieved in simulations. The bare and the capped wire were used as test implants in the MRI experiments.

49

Results

Validation of the attenuated wave model

PWE-simulated transfer matrices and their fits using the attenuated wave model of the TM for the four investigated structures are shown in figure 3.5. The agreement is very good with Pearson correlation coefficients exceeding 0.99 for all implants. This shows that the attenuated wave model is able to accurately capture the induced current in the investigated structures exposed to an incident electric field. Understandably, for symmetrical implants (1 and 4) the TM is also symmetrical.

The transfer function is contained in the transfer matrix

An excitation at the tip of an implant results in an induced current distribution that is proportional to the transfer function of the implant by virtue of the principle of reciprocity [59]. Therefore, the first column of the TM is directly proportional to the TF of the implant. Figure 3.6 shows the first column of the fitted transfer matrix, $M(z, 0)$, in comparison to the transfer function from PWE simulations. The TF is by definition normalized to have unit integral value. In figure 3.6, $M(z, 0)$ is normalized accordingly. The agreement between fitted $M(z, 0)$ and the TF confirms that the transfer matrix parameterized by a few parameters contains an accurate estimate of the transfer function in its first column.

MRI based implant transfer matrix determination

In simulations the relevant electromagnetic quantities, E_{inc} and I_{ind}, are readily available. If these quantities are known, equation 3.5 can be used to determine the transfer matrix. In MRI experiments these electromagnetic quantities are not directly available. However, they can be derived from measurements and simulations. The conductivity of the phantom is determined from a phase only EPT reconstruction using the measured transceive phase distribution [78] in a centered ROI and used in simulations. These simulated $|B_1^+|$ and transceive phase, i.e. $\angle B_1^+ B_1^{-*}$, distributions along with their experimentally determined counterparts are shown in figure 3.7. Data shows that the overall distributions are very similar (R=0.96) although some slight differences do exist. For example, the right top corner of the $|B_1^+|$ distribution in the transverse plane seems to be more enhanced in experiments than in simulations. However, these deviations are minor and are not expected to introduce considerable errors in the resulting transfer matrices.
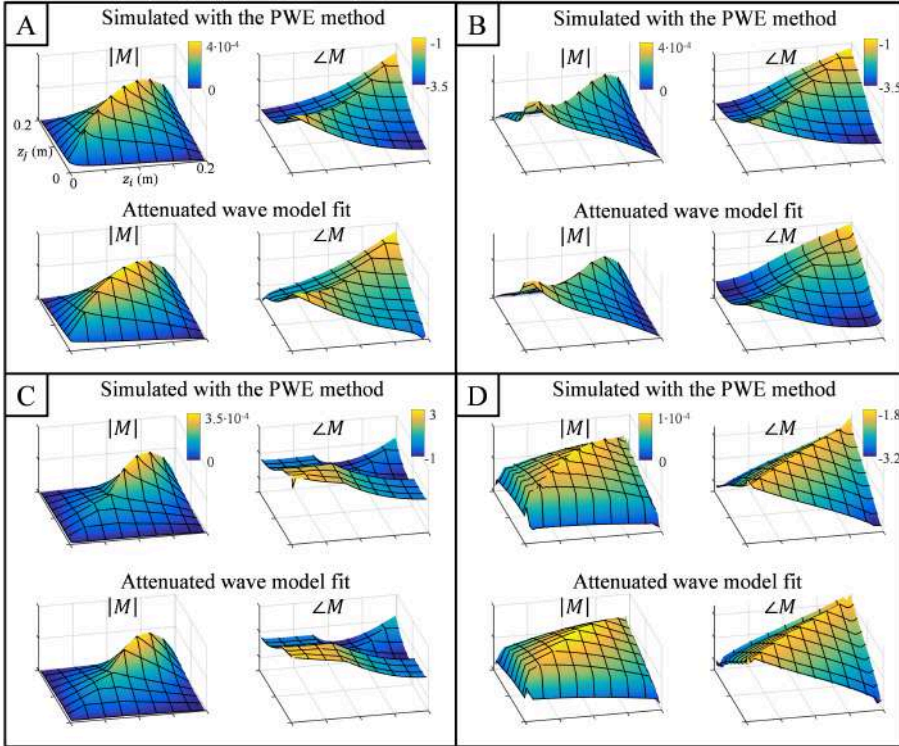
Figure 3.5: Validation of the attenuated wave model: the first row of each subfigure shows the TM that results from the PWE simulations and the second row shows the fitted TM using the attenuated wave model. Note that the x- and y-axis are the same for all plots. This figure demonstrates that the TM of all implants can be accurately characterized using the attenuated wave model (the Pearson correlation coefficient between fitted and simulated TMs was above 0.99 for all structures in both magnitude and phase). Structures A till D correspond to the ones shown in figure 3.3
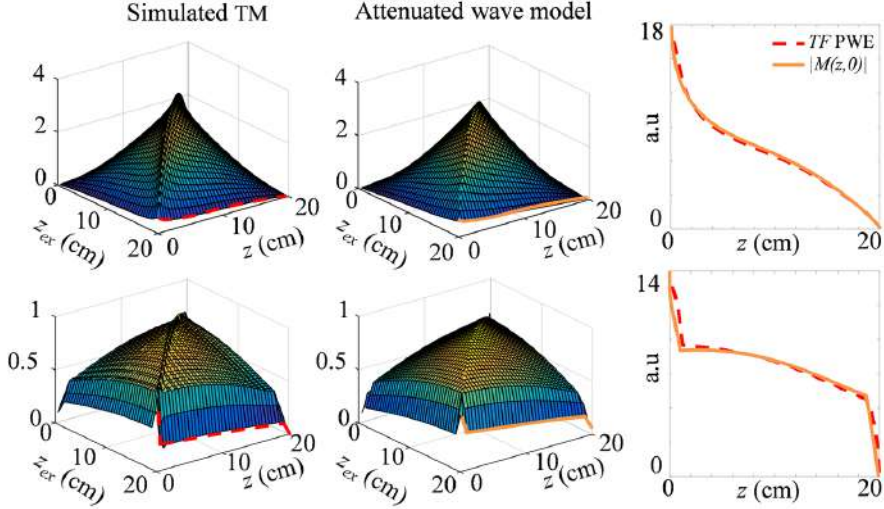
Figure 3.6: The TM contains the transfer function TF. The first column of the TM is directly proportional to the TF of the implant. $M(z, 0)$ is the current distribution in the implant when this distribution is induced by an electric field excitation at the tip. This is proportional to the TF by virtue of the principle of reciprocity [59]. The normalized TF, i.e. to have a unit integral, determined with the PWE method is shown as a dashed red line in the figure of the right. The normalized TF according to the fit of the TM is shown as a solid orange line in this plot. The agreement between both TFs shows that the attenuated wave description keeps the TF intact.

In figure 3.8 the $|B_1^+|$ distribution in the phantom with an embedded implant is shown. The agreement between the distributions in figure 3.8 provides additional confidence in the accuracy of the simulations and the proposed method. A close-up of the $|B_1^+|$ modulation due to the alteration of the RF field by the implant is also shown. This artifact is used to determine the current running in the wire (see appendix B for more details).

The currents are determined from the measured $|B_1^+|$ distributions close to the wire. These measured current distributions along the wires are subsequently used to determine the TM of the bare and the insulated wire with equation 3.5 using a derivative-free, non-linear least squares optimizer (fminsearch). The solution was the one with lowest residual from a set of 256 minimizations performed with equidistantly distributed start points. The same (overall) minimum was found for 29 (11.3%) and 97 (37.9%) out of the 256 start values for the insulated and bare wire, respectively. The frequent occurrence of the found
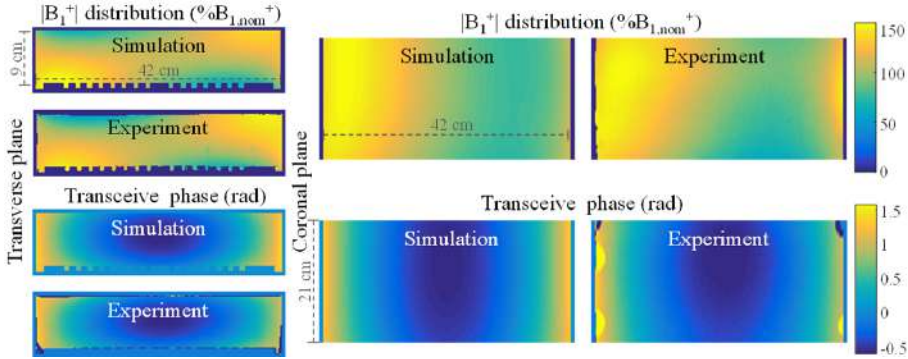
Figure 3.7: The top row shows the simulated and measured |B1+| distributions in percentage of nominal flip angle in the phantom without a wire. The $|B_1^+|$ distribution was experimentally determined with a 3D dual TR actual flip angle (AFI) acquisition [73] with 7x7x5 mm voxel size and a 30ms TR extension on an initial repetition time of 9.1ms. The bottom row shows the simulated and measured transceive phase distributions in radians. The transceive phase was experimentally determined by averaging the phase of two 3D spoiled gradient echo acquisitions with opposing gradient polarities to correct for eddy current contributions [5] and potential timing inaccuracies [74]. Simulations and measurements show good agreement (the Pearson correlation coefficients are $R = 0.90$ and $R = 0.98$ for the magnitude and the phase respectively). Note that the coronal view does not show the entire phantom due to experimental limitations like B_1^+ coverage, B_0 homogeneity and gradient linearity.

minimum with lowest residual suggests convergence to a global minimum in the investigated search space.

The first and second columns in figure 3.9 (bare wire) and 3.10 (insulated wire) show the gold standard TM from PWE simulations and the experimentally determined TM respecively. The normalized TFs that follow from these matrices are plotted in the third column of figure 3.9 and 3.10.

Discussion

This work has presented an alternative method to measure the TF of medical implants using MRI. It does not require alterations to the implant and is therefore a substantial improvement in comparison to the MRI-based method that was presented earlier [66]. Since the electric field is not localized at the tip but will be distributed along the entire implant during an MRI exam, an alternative formalism has been introduced: the transfer matrix. Where the TF can be used to evaluate the electric field at the tip, the TM can be used to determine the total current\electric field anywhere along the implant for a
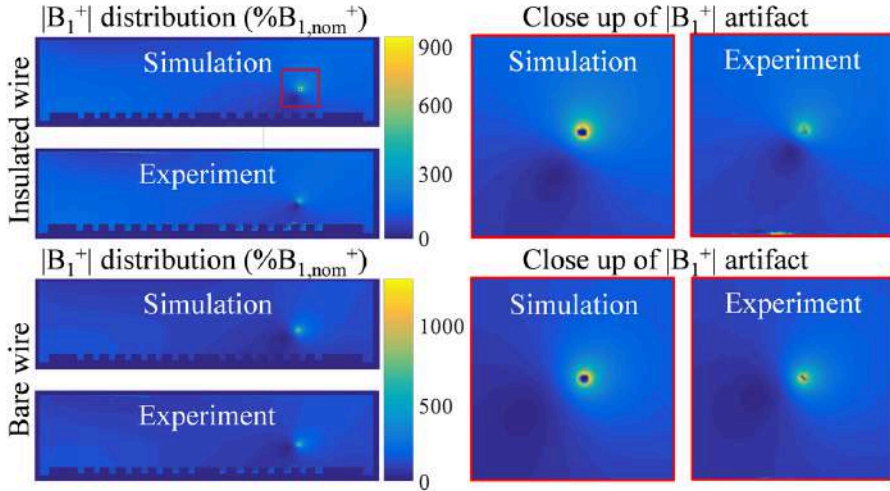
Figure 3.8: Simulated and measured $|B_1^+|$ distributions in percentage of nominal flip angle inside the phantom when an implant is present. A close up of $|B_1^+|$ artifact around the wires is shown on the right. This artifact is used to determine I_{ind} as described in appendix B.

given incident, tangential electric field.

The measurement of the TM by MRI without modification to the implant is only feasible by application of the attenuated wave model which drastically reduces the number of unknowns of this matrix. The attenuated wave description was successfully validated with simulations. With this reduction of unknowns one MRI measurement of the induced current is sufficient to determine the transfer matrix. The TF is contained in the TM as its first row and is hence simultaneously determined. As an additional advantage, the TM also allows identification of other locations that potentially exhibit significant heating along the implant. It is known from practice that localized heating can occur for instance also at impedance transitions in the implant where charge accumulation and thus electric field concentration can take place [79]. Other models [80–82] are available that give an analytical description for the current in a wire due to an incident electric field. With some modifications these models could be used in a similar way as the attenuated wave model.

For the examined structures the presented method was able to accurately measure their TFs (the Pearson correlation coefficients were 0.929 and 0.926 for the bare and the insulated wire respectively). Given a constant electric field
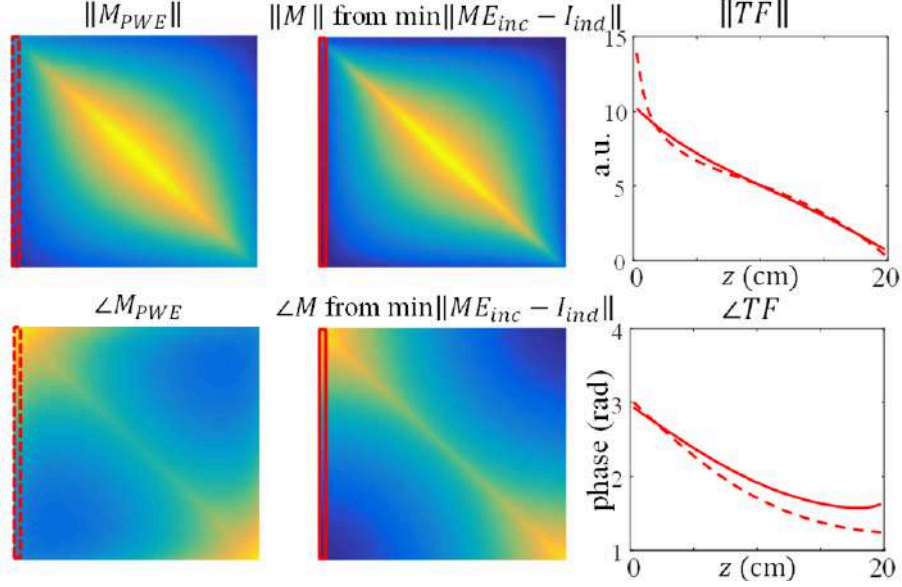
Figure 3.9: The first column in this figure shows the gold standard TM from PWE simulations for the bare wire. The second column shows the TM resulting from the minimization in equation 3.5 given the current measured with MRI and the incident electric field from simulations. The plot in the third column displays the normalized transfer function from measurements (solid line) and simulations (dashed line).

with a worst case phase distribution, i.e. a phase distribution with opposite sign as the phase of the gold standard simulated TFs, the measured TFs would lead to an underestimation of the scattered electric field around the tip of 2.1% and 5.3% respectively in comparison to the simulated cases. The descriptive power of the attenuated wave model for realistic implants is a topic for future research. The number of parameters to describe the response might increase because the wave number can be spatially varying. This will lead to more complicated minimization problems with possible additional numerical challenges. Besides their potentially more complicated descriptions realistic implants might produce susceptibility artifacts that need to be mitigated. This will especially an issue for implants non-parallel with the B_0 field. Many mitigation strategies for metal artifact reduction exist [83], but testing these is beyond the scope of the presented method.

Nonetheless, for the tested generic copper structures the high correlation coefficients between the measured and simulated TFs confirm that the
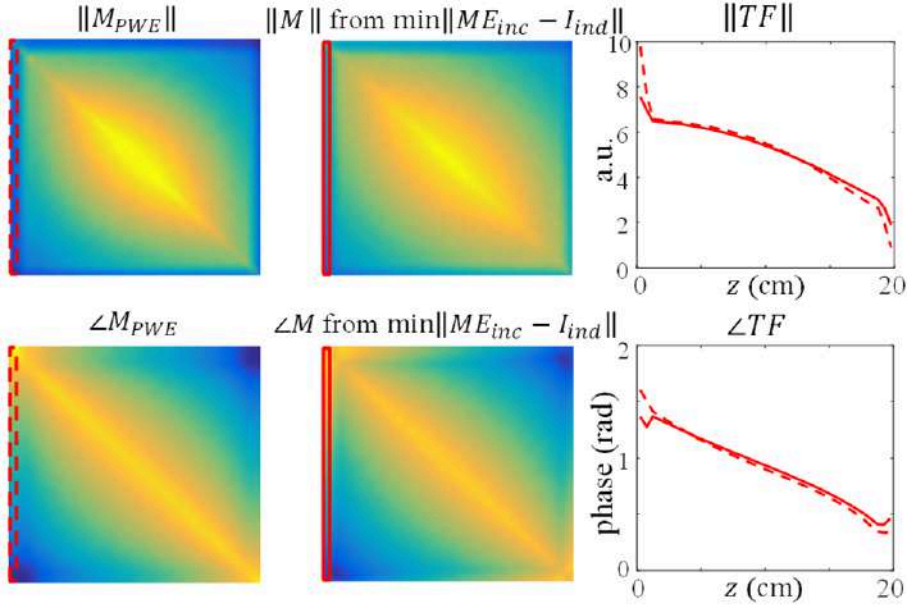
55

Figure 3.10: The experimentally determined TM for the insulated wire. Using the measured induced current and the incident electric field from simulations, equation 3.5 can be used to determine the TM. The first column in this figure shows the gold standard TM from PWE simulations. The second column shows the experimentally determined TM. The plot in the third column displays the normalized transfer function from measurements (solid line) and simulations (dashed line).

normalized transfer function can be accurately determined with the proposed method. In these TMs still some discrepancies are visible for the current estimates close to the tips of the implant. We believe that this is a consequence of the difficulties to accurately determine the low currents and thus low wire $|B_1^+|$ fields near the ends of the wires. Also discrepancies in the phases of the simulated and measured currents are visible. Two potential causes are conceivable. Firstly, the approximation that the transmit and receive phases are equal, the so called transceive phase assumption as used also in EPT, introduces a small error. This approximation is needed to estimate the background phase of the B1+ field created by the birdcage. Secondly, the phase difference between the current in the wire and the background field that follows from the fit of the $|B_1^+|$ artifact, again suffers from the low current magnitudes near the ends of the implant.

Another potential source of inaccuracy are physical deviations between the experiments and the simulations. Some differences between simulations and experiments are inevitably present. For example the wires are assumed to be perfectly aligned with the main magnetic field and perfectly straight. Despite attempts to reach this alignment in practice small angles (less than 5°) with the main magnetic field were present. This leads to errors in the incident electric field, since this is spatially varying, as well as the measured current as it is a projection of the true current on the main magnetic field direction. Other potential sources of inaccuracy are differences in material properties between simulations and experiments, predominantly the phantom liquid and the insulation of the insulated wire. The presented method for TF determination only requires the wire to be aligned with the z-axis because the measurement of the induced current relies on this assumption. Nevertheless, the measurement of induced currents that are not aligned with the z-axis is in principle possible, because the current will always have a nonzero projection on B_1^+. Extension of the current determination method for currents that are not aligned with the z-axis is a topic for future research. This would allow determination of the TF in the case of more realistic lead trajectories.

Most of the aforementioned physical sources of inaccuracy can be mitigated. For example the alignment errors might be reduced with dedicated placeholders for the implants or adaptations to the phantom. More accurate knowledge of the material properties can be attained with dedicated hardware, when available, and could improve agreement between measurements and simulations. Furthermore, a choice was made to determine the current in the wire based on magnitude data. Other approaches, e.g. phase based current determination [71] or a hybrid method, are possible and might perform better. This also holds for the multi flip angle $|B_1^+|$ mapping technique. There are numerous methods [73, 84, 85] to measure $|B_1^+|$ distributions that could outperform the applied technique.

Besides these incremental technical and experimental improvements, MR based TM determination could benefit from other advances. For example, although the induced current along the implant Iind is determined from an MRI measurement, the incident electric field E_{inc} is obtained from simulations. Potentially, simulations can be avoided by means of MRI based E_z-field determination [86]. In this way also the incident, z-component of the electric field can be determined experimentally using the MRI experiment without an implant in the phantom. Although difficulties are expected taking spatial derivatives of the measured, noisy B_1^+ field.

Another limitation is the necessity to perform a separate MRI acquisition without the presence of an implant field to characterize the test setup and therewith validate the exposure field. Note that although a given B1+ magnitude distribution does not uniquely define a corresponding longitudinal electric field distribution, the combination with phase measurements (i.e. the full complex B_1^+ distribution) does. In principle, the scattered and incident electric field could be separated based on their different spatial dependencies. The scattered field drops off radially from the wire and has its source inside the phantom. Contrarily, the incident field is created by sources outside the phantom and can be decomposed in spherical and cylindrical basis functions that are solutions to the source free (or homogeneous) Helmholtz equation [87]. This distinctly different spatial dependency potentially allows reconstruction of both the scattered and incident fields from a single scan with the wire present. However, again knowledge of the complex B_1^+ distribution is required with the implant present, which is hard to attain because its presence makes the transmit and receive phase distinctly different. Multi-transmit methods can be used to remove this obstacle [88].

Currently, inaccuracies of which the significance cannot be exactly gauged, are introduced when a TF measured in a phantom experiment or in simulations are applied to evaluate the heating of an implant in a human body (where the implant's characteristics will be different due to varying loading conditions). The presented method allows TM and hence TF determination in more realistic situations provided that the incident electric fields are assessable and makes it possible to experimentally examine the significance of the uncertainties introduced with this simplification. Furthermore the TM concept can be used in transmit field modification strategies [72, 89–91] to minimize the induced currents in the implant. Most importantly it allows determination of the TF without the need for electric field probes or alterations to the implant with a high spatial resolution that has the potential to be used in solids. With considerable modifications and additional work to the method presented here it is conceivable that extensions to TF determination in heterogeneous media and even animal tests can be made.

Conclusion

We have presented a method to measure the transfer function of an implant in a designated phantom using an MRI scanner without alterations to the implant. The Pearson correlation coefficients between measured and the simulated transfer functions were 0.929 and 0.926 for a 20 cm bare and a 20 cm

insulated wire respectively. For this method, the concept of the transfer matrix was introduced. This matrix relates the induced current along an implant to an incident E-field distribution. This matrix contains the transfer function in its first column. The measurement of this matrix by MRI is feasible by application of an attenuated wave model which drastically reduces the number of unknowns of this matrix. The applicability of this model for (partially) insulated wires in a homogeneous medium was verified with numerical simulations. Using a validated experimental test setup in which the electric field exposure is known, one MRI measurement of the induced current is sufficient to determine the TM and hence also the TF of an simple implant model. For application of the presented method to TF determination of realistic (and often more complex) implants the TM model needs to be extended which might prove to be a non-trivial task.

The introduced TM enables MRI based TF determination without hardware alterations to implant or scanner. This MRI based method opens up possibilities to determine TFs in more realistic scenarios like solid tissues, heterogeneous media and test animals

MRI-based transfer function determination through the transfer matrix by jointly fitting the incident and scattered B$_1^+$ field

Tokaya, Janot P.
Raaijmakers, Alexander J.E.
Luijten , Peter R.
Sbrizzi, Alessandro
van den Berg, Cornelis A.T.

Abstract

Introduction: Purpose: A purely experimental method for MRI-based transfer function (TF) determination is presented. A TF characterizes the potential for radiofrequency heat-ing of a linear implant by relating the incident tangential electric field to a scattered electric field at its tip. We utilize the previously introduced transfer matrix (TM) to determine transfer functions solely from the MR measurable quantities, that is, the B_1^+ and transceive phase distributions. This technique can extend the current practice of phantom-based TF assessment with dedicated experimental setup toward MR-based methods that have the potential to assess the TF in more realistic situations.

Theory & Methods: An analytical description of the B_1^+ magnitude and transceive phase distribution around a wire-like implant was derived based on the TM. In this model, the background field is described using a superposition of spherical and cylindrical harmonics while the transfer matrix is parameterized using a previously introduced attenuated wave model. This analytical description can be used to estimate the transfer matrix and transfer function based on the measured B_1^+ distribution.

Results: The TF was successfully determined for 2 mock-up implants: a 20-cm bare copper wire and a 20-cm insulated copper wire with 10 mm of insulation stripped at both endings in respectively 4 and 3 different trajectories. The measured TFs show a strong correlation with a reference determined from simulations and between the separate experiments with correlation coefficients above 0.96 between all TFs. Compared to the simulated TF, the maximum deviation in the estimated tip field is 9.4% and 12.2% for the bare and insulated wire, respectively.

Conclusions: A method has been developed to measure the TF of medical implants using MRI experiments. Jointly fitting the incident and scattered B_1^+ distributions with an analytical description based on the transfer matrix enables accurate determination of the TF of 2 test implants. The presented method no longer needs input from simulated data and can therefore, in principle, be used to measure TF's in test animals or corpses.

Introduction

The transfer function (TF) has been introduced to characterize the potential for RF heating of elongated linear medical implants like pacemaker and deep brain stimulator leads [41]. The TF is an implant characteristic that describes the scattered electric field at the tip of an implant, where it is most significantly enhanced, as a function of an incident tangential electric field distribution along the trajectory of the implant. For active implantable medical devices (AIMD) these are located at the electrode poles which deliver the therapeutic currents to the tissue. The TF simplifies numerical computations to predict heating because it decouples the assessment of the local scattered field (requiring submillimeter detailed modeling of an implant) from the determination of the incident field (generated and scattered by relatively large objects like the transmit coil and human body respectively).

Experimental validation of numerically determined TFs is performed in phantom experiments. Common measurement methods rely on standardized phantom setups [42,43] and specialized excitation devices and/or measurement probes. A device that applies a confined and localized electric excitation is stepwise repositioned along the length of the implant while the scattered electric field at the tip is monitored. The ratio between the complex electric field at the tip and the complex field at the excitation device as a function of position along the implant gives the value of the transfer function at the location of the excitation. Alternatively, the excitation device and measurement probe swap position: the induced field along the wire as a function of position is measured while the implant is excited at the tip [59]. Both methods are equivalent due to the principle of reciprocity. In previous work, this principle of swapping excitation and measurement position was used to develop a fully MR-based method where the implant is modified into a transmit-receive antenna that is driven at its tip. For this purpose, an RF cable was soldered to the implant and connected to the scanner by a transmit/receive coil interface. Now the current induced in the implant is proportional to the TF and is calculated from acquired MR images [66].

Recently, this method was further improved which enabled the use of standard RF coils and removed the need to make modifications to the implant [92]. For this purpose, the transfer matrix (TM) was introduced. The TM relates an incident tangential electric field distribution along an implant to an induced current distribution along the entire length of implant. This gives a more complete description of the interaction of an implant with an RF electric field than the TF, which focuses on the description of a single point of worst case

heating. In figure 1 an example of a TM is shown, together with a schematic depiction of the way it is determined in simulations as described previously [92]. The method for TM determination relies on knowledge of the induced current, that can be measured with MRI [44, 45, 55, 71], and the incident electric field, that is determined by simulations.

Even though this works for standardized phantom setups with known or measurable geometrical and electromagnetic properties, it rules out the application on less well-determined environments where this knowledge is missing as for example in test animals or human corpses, which makes accurate simulations practically infeasible. In principle, if also the incident electric field distribution can be obtained from MRI measurements, in-vivo transfer function assessment could become feasible.

Here we present a method that is able to determine the TF of an implant exclusively from MRI acquisitions in a single phantom experiment. Contrarily to previously presented work the incident electric field is determined from MRI measurements instead of simulations. Under certain, yet realistic, conditions for linear implant safety testing, the z-component of the electric field distribution is dominant and can be determined from the B_1^+ distribution [86]. In this work we present a model describing the RF magnetic field distribution around an elongated implant following an arbitrary trajectory. This model is used to jointly estimate the transfer matrix and the incident background field based on their different spatial dependencies. Firstly, the validity of this model will be tested on simulated B_1^+ distributions for a bare and insulated wire. Secondly, the TM and TF are determined experimentally for the same two wires. Measurements are performed for various trajectories which will result in different incident electric field exposures and induced currents but should yield the same TM and TF. The presented method allows simultaneous TM and TF determination from a B_1^+ magnitude and transceive phase distribution that are assessable with MRI.

Theory

Without loss of generality, the B_1^+,tot distribution in a subject or a phantom with an implant can be written as,

$$B_1^+{}_{tot} = B_1^+{}_{bg} + B_1^+{}_{sc} \tag{4.1}$$

In this equation, $B_1^+{}_{bg}$ is the circularly polarized incident background RF transmit magnetic field created in the subject or phantom by the transmit coil that

is used for the MR exam. $B_1^+{}_{sc}$ is the circularly polarized component of the scattered RF transmit magnetic field created by the currents that are induced in the implant. The relatively smoothly varying background B+1 magnetic field can be accurately decomposed in SPherical And CYlindrical (SPACY) harmonics [87] that are solutions to the source-free Helmholtz equation for a homogeneous medium in a spherical and cylindrical coordinate system respectively, that is,

$$B_1^+{}_{bg} = \sum_{n=0}^{N_1} \sum_{m=-n}^{n} a_{mn} f_n^m + \sum_{n=0}^{N_2} \sum_{m=-n}^{n} b_{mn} g_n^m \qquad (4.2)$$

where $f_n^m = j_m(\zeta r) Y_n^m(\theta, \phi)$ and $g_n^m = J_m(\zeta \rho) Y_n^m(\vartheta)$. Here, jm is the spherical Bessel function of the first kind of order m, J_m is the ordinary Bessel function of the first kind of order m, and Y_n^m is the spherical harmonic of order n and degree m. The tuples (r, θ, ϕ) and (ρ, ϑ, z) describe the spherical and cylindrical (with z being the main magnetic field direction) coordinate system respectively with the isocenter of the MR scanner as the origin. The parameter ζ is the complex wavenumber of the electromagnetic waves given by $\zeta = \pm \sqrt{\mu_0 \epsilon_r \epsilon_0 \omega^2 + i \mu_0 \sigma \omega}$. The Neumann functions are excluded from the solution set of the Helmholtz equation, because they have a pole at the origin and hence are unable to describe the incident fields. The expansion coefficients a_{mn} and b_{mn} can be determined by fitting equation 4.2 to a measured $B_1^+{}_{,tot}$ field distribution with omission of the limited region where the scattered field caused by to the implant has a significant contribution. The phase of the complex $B_1^+{}_{,bg}$ field is considered to be half the transceive phase [62]. Note that this transceive phase assumption will not be accurate for $B_1^+{}_{,tot}$ because the presence of the implant presents an asymmetric load to both ports of the birdcage. However, our method only requires the transceive phase approximation to be valid for the background field. Given the (near) left-right symmetry of the setup [93] and a circularly polarized $B_1^+{}_{,bg}$, this assumption will be sufficiently accurate for the experiment presented here because the experi-ments are performed at 1.5T [94].

After the $B_1^+{}_{,bg}$ is approximated by the SPACY decomposition, the incident electric field can be calculated [86] because the electric and magnetic fields are intrinsically coupled as described by Maxwell's equations. If one assumes that the longitudinal component of the $B_1^+{}_{,bg}$ field created by the RF coil is negligible, the z-component of the electric field is calculated by:

$$E_{zbg}(\vec{r}; a_{mn}) = \frac{1}{\mu_0 \sigma + i\omega\mu_0\epsilon} \left(-2i\frac{\partial}{\partial x} - 2\frac{\partial}{\partial y} \right) B_1^+{}_{bg}(\vec{r}; a_{mn}) \qquad (4.3)$$

It should be noted that this assumption is valid in the central region and particularly in the midplane of the birdcage coil that are customarily used for 1.5T clinical examinations.

The implant with a random trajectory C, which can be straight or bent and make arbitrary angles with the main magnetic field direction, creates a scattered field. The trajectory C is parameterized by $\vec{r}'$. Therefore, the implant is exposed to a tangential incident electric field, $E_{inc}(\vec{r}')$, that can be computed from this $E_{zbg}(\vec{r}')$ by multiplication with the cosine of the angle, the wire makes with the z-axis at $\vec{r}'$, that is,

$$E_{inc}(\vec{r}; a_{mn}) = E_{zbg}(\vec{r}; a_{mn})\cos(\theta') \qquad (4.4)$$

Equation 4.3 assumes that the x and y component of the electric field are negligible compared to the z-component of the electric field. The current induced in the implant attributed to this E_{inc} is calculated through a multiplication with the TM. The scattered magnetic field caused by the implant is subsequently calculated from the induced current using the time-dependent generalization of the Biot–Savart law known as the Jefimenko equations [95,96]. These equations describe the electromagnetic field attributed to arbitrary time-dependent current and charge distributions while taking retardation into account. The magnetic field is given by,

$$\vec{B}_{1,sc}(\vec{r}, t; a_{mn}, c_k) = \frac{\mu_0}{4\pi} \int_C \Big(\frac{I(\vec{r}', t_r; a_{mn}, c_k)\mathrm{d}\vec{r}' \times (\vec{r}' - \vec{r})}{|\vec{r}' - \vec{r}|^3}$$
$$+ \frac{\partial I/\partial t(\vec{r}', t_r; a_{mn}, c_k)\mathrm{d}\vec{r}' \times (\vec{r}' - \vec{r})}{c|\vec{r}' - \vec{r}|^2} \Big) \qquad (4.5)$$

The scattered field is time and space dependent and can be described by the sets of parameters describing the background field, a_{mn} and b_{mn}, and the parameters describing the transfer matrix of the implant, c_k, this equation describes the magnetic field caused by a general time-varying current I running in the implant. It will take a finite amount of time for the field created by the current at $\vec{r}'$ to reach a certain position $\vec{r}$ which is incorporated in the model through the retardation time $t_r = t - \frac{|\vec{r}' - \vec{r}|}{c_m}$, where c_m is the speed of light in

the medium through which the field propagates. Equation 4.5 is valid whenever the macroscopic Maxwell equations inside a homogeneous dielectric are valid. Because we will assume harmonic time dependency ($\vec{B}(\vec{r},t) = \vec{B}(\vec{r})e^{i\omega t}$) we can write equation 4.5 in phasor notation as,

$$\vec{B}_{1,sc}(\vec{r},t;a_{mn},c_k) = \frac{\mu_0}{4\pi}\int_C I(\vec{r}';a_{mn},c_k)\mathrm{d}\vec{r}' \times (\vec{r}' - \vec{r})e^{i\frac{|\vec{r}'-\vec{r}|\omega}{c_m}}$$
$$\left(\frac{1}{|\vec{r}'-\vec{r}|^3} + \frac{i\omega}{c|\vec{r}'-\vec{r}|^2}\right) \tag{4.6}$$

This describes the scattered field attributed to an arbitrarily shaped wire. In the model used here, the wire will be discretized into a number of line segments that correspond to the size of the transfer matrix (e.g., into 40 line segments of 5 mm for the 200 mm wires considered here). The incident electric field is discretized to the same resolution. In the discretized form after introduction of the TM, equation 4.6 can be approximated by a Riemann sum, that is,

$$\vec{B}_{1,sc}(\vec{r};a_{mn},c_k) = \frac{\mu_0}{4\pi}\sum_{i=1}^{\frac{L}{|\mathrm{d}r_i|}} M(c_k)E(\vec{r}_i;a_{mn})\mathrm{d}\vec{r}_i \times (\vec{r}_i - \vec{r})e^{i\frac{|\vec{r}_i-\vec{r}|\omega}{c_m}}$$
$$\left(\frac{1}{|\vec{r}_i-\vec{r}|^3} + \frac{i\omega}{c|\vec{r}_i-\vec{r}|^2}\right)$$
$$= \frac{\mu_0}{4\pi}\sum_{i=1}^{\frac{L}{|\mathrm{d}r_i|}} M(c_k)\frac{-\cos(\theta_i)}{\sigma + i\omega\epsilon}(2i\partial_x + 2\partial_y)B_1^+{}_{,bg}(\vec{r}'_i;a_{mn})$$
$$\mathrm{d}\vec{r}_i \times (\vec{r}_i - \vec{r})e^{i\frac{|\vec{r}_i-\vec{r}|\omega}{c_m}}\left(\frac{1}{|\vec{r}_i-\vec{r}|^3} + \frac{i\omega}{c|\vec{r}_i-\vec{r}|^2}\right) \tag{4.7}$$

which is linearly dependent on (the coefficients describing) the background field. In this equation, θ_i is the angle the ith line segment makes with the z-axis. The superposition of the circularly polarized RF transmit magnetic incident and scattered field, that is, the total B_1^+ field is hence given by,

$$B_1^+{}_{tot}(\vec{r};a_{mn},c_k) = B_1^+{}_{bg}(\vec{r};a_{mn})$$
$$+ \frac{1}{2}\left(B_1^x{}_{sc}(\vec{r};a_{mn},c_k) + B_1^y{}_{sc}(\vec{r};a_{mn},c_k)\right) \tag{4.8}$$

which is again linearly dependent on the coefficients in the SPACY decomposition. This model can be used to fit a measured or simulated B_1^+ distribution. Note that equation 4.8 describes a complex B_1^+ distribution of which the
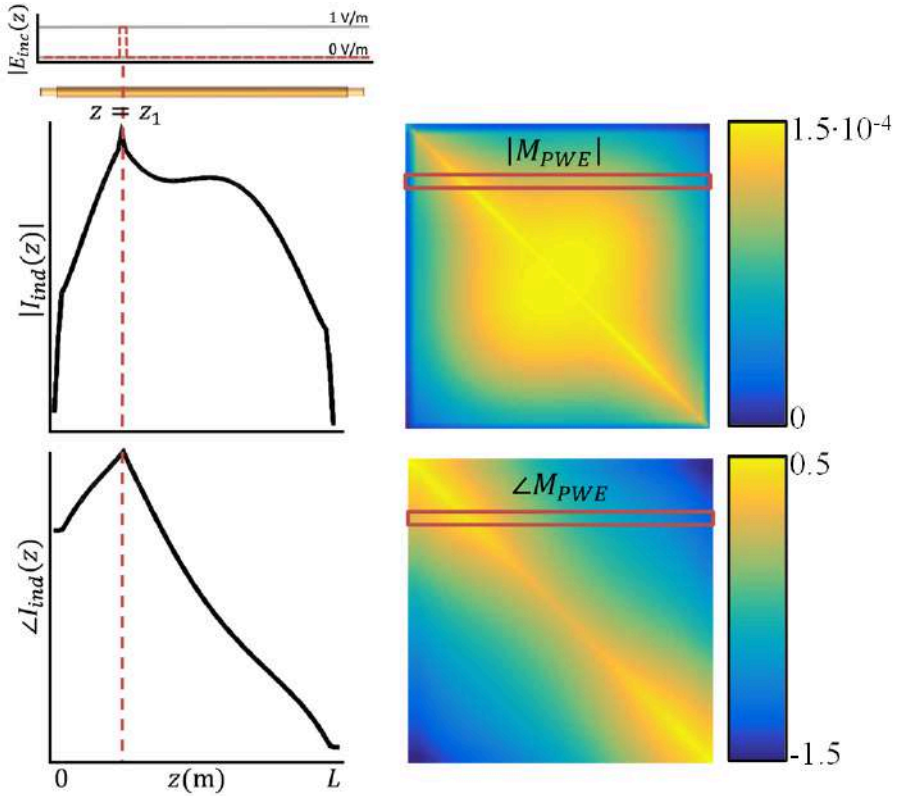
Figure 4.1: The TM is constructed in simulations by application of a localized incident electric fields of 1 V/m created with 2 plane waves that have constructively interfering electric and destructively interfering magnetic field components. This excitation is repositioned along the entire length of the implant. The resultant current distributions for the various excitations describe the rows of the TM. The width of the excitation determines the resolution to which the TM is resolved. Given an implant with a certain TM and some incident electric field, the induced current in the implant is computed with a matrix multiplication, that is, $I = ME$

phase is not experimentally attainable. What can be measured is the so-called transceive phase, which is the sum of the phase of the B_1^+ and B_1^- field. For birdcage coils, the phase of the background receive field is (nearly) equal to the phase of the background transmit field [62]. This is known as the transceive phase approximation stating that the transmit phase will be half the transceive phase. Using this approximation, we can describe the receive background phase with the same SPACY decomposition. A description similar to equation 4.8 can be derived for the phase of B_1^- as a function of the same unknowns. The scattered field contribution to the receive fields is in the direction opposite to the nuclear precession leading to a complex conjugation of the scattered field. Hence, we can write down an expression for the B_1^-,tot phase, that is,

$$\angle B_{1\,tot}^-(\vec{r}; a_{mn}, c_k) = \angle \left(B_{1\,bg}^+(\vec{r}; a_{mn}) \right.$$
$$\left. + \frac{1}{2}\left(B_{1\,sc}^x(\vec{r}; a_{mn}, c_k) + B_{1\,sc}^y(\vec{r}; a_{mn}, c_k) \right)^* \right) \quad (4.9)$$

The transceive phase is the sum the phase given by this equation and the phase of equation 4.8 . It needs to be stressed that equation 4.9 describes the B_1^- phase in the assumption that the background transmit and receive phase are nearly equal. For our purpose, the decomposition of the magnitude of the receive field is not relevant given that we will only use the MRI-measurable distributions ($|B_1^+|$ and transceive phase).

Methods

Equation 4.8 provides an expression for the B_1 field surrounding an elongated implant as a function of the background field parameters a_{mn} and b_{mn} and the transfer matrix parameters c_k. If a B_1^+ map is acquired together with a transceive phase distribution, ϕ_{tr}, with the implant to be tested in a phantom, the transfer matrix can be determined by fitting this expression to the measured (or simulated) field distribution. The corresponding minimization is,

$$\operatorname*{argmin}_{a_{mn}\in\mathbb{C},c_k\in\mathbb{R}} \left\| |B_{1\,meas}^+|e^{\phi_{tr,meas}} \right.$$
$$\left. - |B_{1\,tot}^+(a_{mn}, c_k)|e^{i\arg(B_{1\,tot}^+(a_{mn},c_k)B_{1\,tot}^-(a_{mn},c_k))} \right\| \quad (4.10)$$
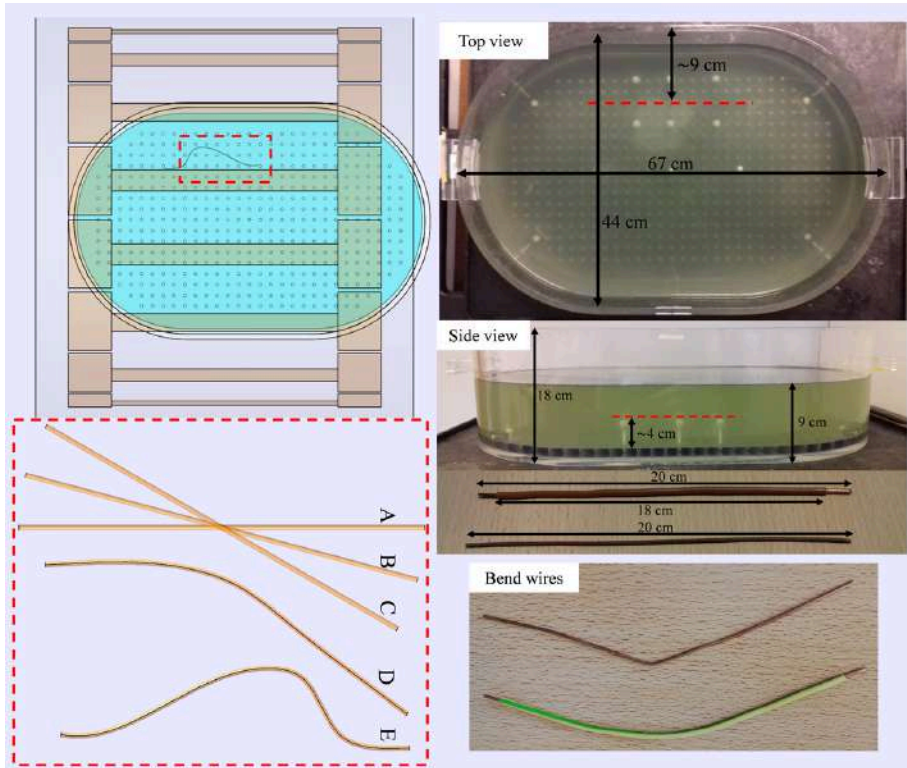
Figure 4.2: The elliptical ASTM phantom in which the dummy implants are placed is shown on the right. The wires are located on a thin sewing thread stung between 4.5cm long plastic screws. The wires are positioned approximately 13 cm away from the center of the phantom and submerged under 5 cm of phantom liquid. The setup of the phantom in the birdcage body coil is shown on the left together with the 5 bare wires that are used in simulations

This procedure was tested for 2 implant-like structures: a 20 cm bare wire and a 20 cm insulated wire where the insulation is stripped from 10 mm at both endings as shown in the bottom right corner of 4.2. For both structures, the MRI measurements are performed with the structures positioned in an elliptical ASTM (American Society for Testing and Materials) phantom also shown in figure 4.2. The elliptical phantom has 11-mm-thick walls of poly-methylmethacrylaatand is filled with hydroxyethyl cellulose gel with relative permittivity of 77 and a conductivity of 0.47 S/m.

The a_{mn}'s and b_{mn}'s that describe the background field and determine the incident electric field are found by a least-squares SPACY decomposition of the complex B_1^+ field disregarding B_1^+ data within a circular region (radius 5 cm) around from the wire. The phase of complex background B_1^+ field is simply considered to be half the transceive phase [62]. An initial guess for the transfer matrix parameters ck is obtained by assuming full out-of-phase reflection at both endings and a propagation constant based on the permittivity and conductivity of the phantom material ($\Gamma_0 \approx -1, \Gamma_0 \approx -1, t \approx 0.01, c \approx \sqrt{\mu_0 \overline{\epsilon_{body}}\omega^2 + i\mu_0 \overline{\sigma_{body}}\omega}$). these initial values, the minimization in equation 4.10 is performed. The Nelder–Mead simplex algorithm [97] implemented in a bound version of MATLAB's fminsearch function (The MathWorks, Inc., Natick, MA) is used to perform the mini-mization. The c_k that follow from this minimization define the TM and TF of the implant. First, the method is tested in silica, that is, using simulated B_1^+ field distributions. Subsequently, the method is applied for experimental TM and TF determination from measured $|B_1^+|$ and transceive phase distributions.

Simulations

The presented procedure and the validity of the field description given by equations 4.8 and 4.9 are tested in silica by numerical FDTD (finite-difference time-domain) simulations (Sim4Life; ZMT, Zurich, Switzerland). A harmonic simulation is performed for 50 periods with a –50dB auto termination condition of a model of the phantom shown in figure 4.2 in the isocenter of a 1.5T birdcage body coil. A 16 rungs high pass birdcage coil tuned to 64 MHz with 35.2-cm coil radius and 42-cm rung length is driven in quadrature mode with 2 voltage sources (IQ-feed). The RF shield with a radius of 37.2 cm and length of 70 cm is composed of perfect electric conductor. The wire positions and trajectories are also shown in figure 4.2. Simulations are performed with a straight wire trajectory aligned with the z-axis, called A. This straight wire is also placed under an angle of 15° and 30° with respect to the main magnetic field, denoted

71

as B and C respectively. Furthermore, 2 arbitrarily bent wire trajectories D and E are also simulated. For the insulated wire, simulations were performed with implant following trajectories A, B, C, and D, which are labeled A_i, B_i, C_i, and D_i respectively.

The resulting B_1^+ magnitude and transceive phase distribution from these simulations are fit with equations 4.8 and 4.9 while optimizing for the TM parameters and keeping the coefficients in the SPACY decomposition of the background field fixed. Note that these distributions (B_1^+ magnitude and transceive phase) are measurable with MRI.

Measurements

The actual MRI measurements were performed in a 1.5T (Philips Ingenia, Best, The Netherlands) MR scanner. $|B_1^+|$ distributions are determined experimentally with the variable flip angle (VFA) method [75, 76]. The elliptical phantom is filled with copper sulfate doped hydroxyl ethyl cellulose (9 cm filling height), with relative permittivity of 77 and a conductiv-ity of 0.47 S/m. The wires are placed approximately 10 cm off-center in the x-direction submerged under 5 cm liquid inside the phantom in the center of the birdcage coil. A straight wire was placed at a 0°, 15°, and 30° angle relative to the z-axis. Subsequently, the bare wire was bent and an additional acquisition was performed.

The VFA method is used instead of more conventional $|B_1^+|$ mapping techniques [73, 85] given that it is able to capture the large dynamic range of actual $|B_1^+|$ values in the vicinity of the wire at the expense of increased acquisition time. For this purpose, a collection of 3D spoiled gradient echo images with various nominal flip angles8 were acquired. The spoiled gradient echo images had a field of view (FOV) (anterior/posterior [AP]× right/left [RL] × feet/head [FH]) of 111×430×250 mm and a voxel size of 1×1×5 mm³. The relatively high resolution in the AP and RL direction are necessary to capture the rapid decay of the $|B_1^+|$ enhancement around the wire. The nominal flip angles were dynamically varied to be 0.25, 0.5,1, 2, 3, 5, 7.5, 10, 12.5, 15, 17.5, 20, 22.5, 25, 27.5, 30, 35, 40, 60, 80, and 100°. The acquisitions had a repetition time of 40 ms, leading to a scan duration of 3 minutes 13 seconds per flip angle. From these acquisitions, the $|B_1^+|$ was determined by fitting the signal from the spoiled gradient echo acquisitions on a voxel-by-voxel basis as function of flip angle using its well-known signal equation [98]. The relaxation times of the phantom fluid were measured [77] and used for the fit with the signal

equation. The resulting fit parameters provide the magnitude of the trans-mit field distribution $|B_{1\,meas}^+|$ and also the receive sensitivity distribution.

The transceive phase distribution is acquired with two 3D multiecho spoiled gradient-recalled echo acquisitions with opposite gradient polarities to correct for eddy current contributions [5] and potential timing inaccuracies [74]. These scans have the same resolution and FOV as the VFA acquisitions. Four echoes are acquired to correct for static B_0 phase contributions [62], which are dominated by the jump in susceptibility at the interface separating the air and the phantom A simple linear regression on the unwrapped phase data as a function of time is used to correct for B_0 contributions. The 3D phase is unwrapped using an energy minimization framework based on graph cuts [99, 100]. The B_0 and eddy current corrected phase only contains the transmit and receive RF phase contributions. This transceive phase and the B+1 magnitude distribution are simultaneously fitted with equation 4.8 (and equation 4.9) to find the parameters $\{\sigma_{eff}, \Gamma_0, \Gamma_L, c_1, c_2, ..., \Gamma_{12}, \Gamma_{23}, ...\}$ that describe the TM.

The conductivity of the liquid in the phantom is determined using the SPACY decomposition. The conductivity and permittivity of the phantom medium determine the wave vector of waves that generate the background field. A parameter sweep through realistic conductivity (0:1 S/m) and permittivity ($1\epsilon_0$:$150\epsilon_0$) values was performed with steps of 0.01 S/m and 1, respectively, to select the values that give lowest residual in the decomposition of the background field. Subsequently, the SPACY decomposition is performed with these optimal dielectric phantom properties to determine the a_{mn}'s.

Results
Simulations
First, the applicability of equations 4.8 and 4.9 to describe the scattered B_1^+ field and transceive phase distribution was tested in silica. Simulated $|B_1^+|$ and transceive phase distributions were fitted with equations 4.8 and 4.9 using the minimization given in equation 4.10. The results of these fits for a phantom with a 20 cm bare and insulated wire together with the actual simulated distributions are shown in figures 4.3 and 4.4, respectively. An example of the resulting TM is given in figure 4.5 for the straight wire trajectories. The TMs that follow from the other simulated distributions can be found in appendix C figures 7.4 to 7.10. The background parameters are fixed at the values that results from the SPACY decomposition of the total field distributions with data within a 5 cm distance from the implant removed.
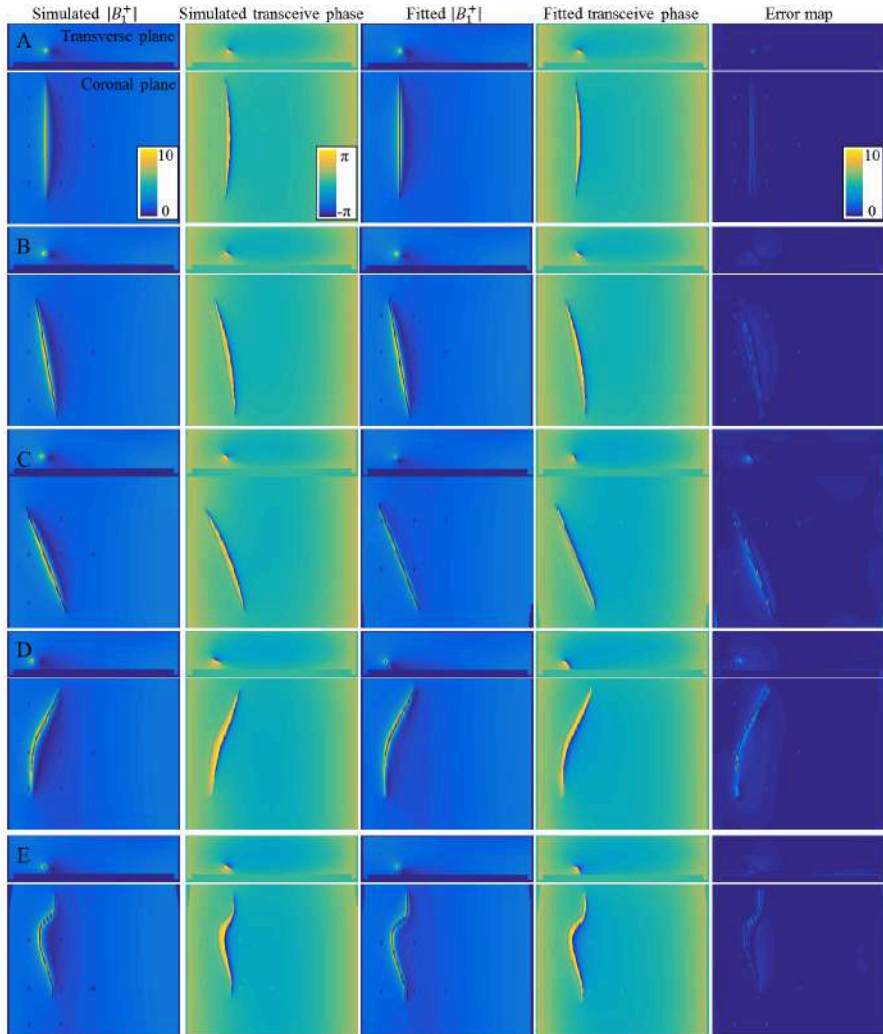
Figure 4.3: The simulated B_1^+ magnitude and transceive phase distribution around the bare 20 cm wire in orientations (A), (B), (C), (D), and (E) are shown on the left. These fields are fitted with equations 4.8 and 4.9 using the minimization given in equation 4.10. The results from these fits are shown in the third and fourth columns. The absolute error shown on the right is small compared to the B_1^+ magnitude.

Figure 4.4: The simulated B_1^+ magnitude and transceive phase distribution around the insulated 20-cm wire in orientations A_i, B_i, C_i, and D_i are shown on the left. These fields are fitted with equations 4.8 and 4.9 using the minimization given in equation 4.10. The results from these fits are shown in the third and fourth columns. The absolute error shown on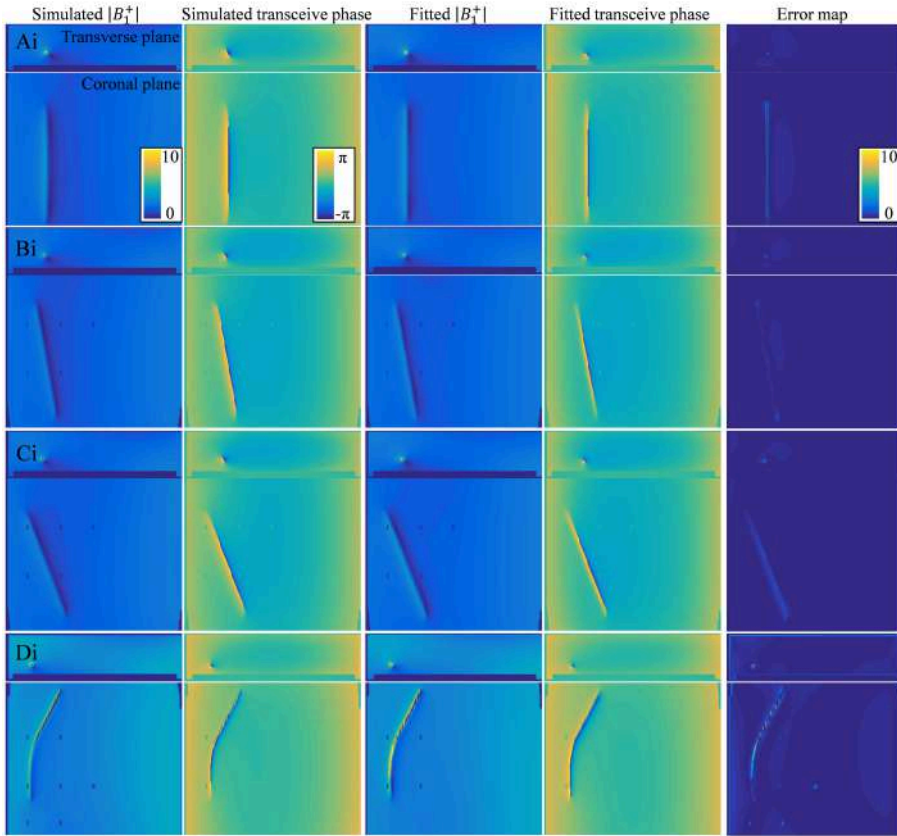 the right is small compared to the B_1^+ magnitude. The screws that keep the implant afloat are not captured by the SPACY harmonics and show up as bright spots in the absolute error map.
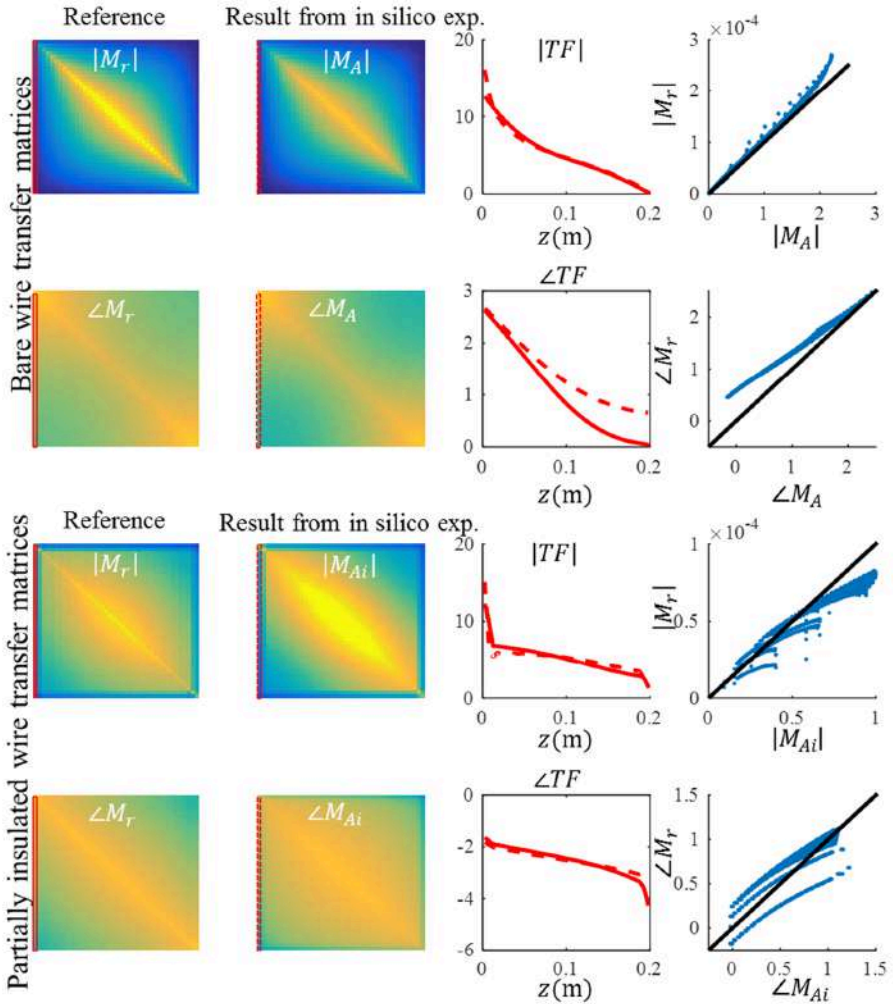
Figure 4.5: Two examples of the TF and TM that follow from the fit of the fields shown in figures figure 4.3 and figure 4.4. The results for the straight wire aligned with the z-axis are displayed here, that is, from distribution (A) and (A_i) in figures figure 4.3 and figure 4.4, respectively. Ideally, the TMs that follow from the full field fit should be identical to the reference TMs and lie the line x = y in the outmost right figures. This is not exactly the case, but Pearson correlations are high, with R = 0.983 and R = 0.962 for the bare and insulated wire, respectively

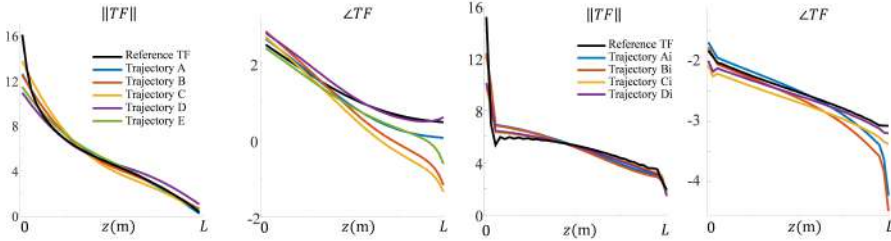**Figure 4.6:** The normalized TFs that follow from the fits of the simulated fields displayed for the bare wires and insulated wires in figures 4.3 and 4.4, respectively. The TFs found from fitting the fields for the different wire trajectories resemble the gold-standard TF.

When simulations are available, it is possible to make a comparison between the current that is running in the implant according to the fit and the current that is actually running in the implant from the simulation results. Likewise, the background field that follows from the fit can be compared to the actual background field, which is com-puted in a separate simulation without a wire in the phan-tom. The maximal absolute relative error in the current distribution on the wire is 3.8%, and the mean relative error is 1.2% for the straight wire aligned with the z-axis. The Pearson correlation between the current from simulation and from the fit of the field distributions is 0.9977. The maximal error in the background field estimate was a lot higher with 26.4%, which occurs near the edges of the phantom. Nevertheless, the overall shape of the background field is accurately described with the SPACY decomposition, as indicated by the average relative error of 3.9%. Also, the more distant deviations will not influence the TM and TF assessment. The TF and TM for the bent wire are compared to simulations in figure 4.4. The normalized TF that follows from the fit of the $|B_1^+|$ and transceive phase distribution closely follows the reference TF. The same holds for the wires in the other trajectories, as is displayed in figure figure 4.5 and in appendix C in figures 7.4 to 7.10. These results show that the model accurately decomposes the total field into its back-ground component and the scattered component and hence gives a correct estimate for the induced current and the TF.

For the partially insulated wire, the TM in equation 4.8 depends on 10 parameters, which makes the minimization given by equation 4.10 somewhat more challenging. The resulting field distribution of the fits for a phantom with a partially insulated 20 cm wire together with the actual simulated distributions are shown in figure 4.4. In the case of the insulated wire, the Pearson correlation between the current from simulation and from the fit of the field distributions

is 0.9752 with a mean relative error over the distribution of 2.36% (which is an underestimation of the deviation in the fitted current that is maximal at the transition between the insulated and bare regions). Still, the TFs that follow from the fit are in good agreement with the reference TF for all the trajectories.

The results shown in figures 4.3 and 4.4, and the supplementary figures in appendix C demonstrate that the model given by equations 4.8 and 4.9 describes the fields adequately. The c_k parameters that result from fitting the simulated distributions are the parameters describing the TMs, and thereby the TFs for the bare and partially insulated wire. These TMs are compared to the TMs determined with simulations of subsequently repositioned incident electric fields generated with thin plane wave boxes. The TMs that result from these simulations are considered the ground-truth reference. For the wires aligned with the z-axis, the TMs that result from the fit of the field are shown in figure 4.5 together with the ground-truth TM. The first row of the TM is the TF and is shown in the third column of figure 4.5 . This TF and the TFs that result from the other in silica experiments together with the directly simulated reference are shown in figure 4.6. .

Measurements

The same method is tested on experimentally determined $|B_1^+|$ and transceive phase distributions. The measurement results and their fits are shown in figures 4.7 and 4.8, respectively. In the measured data, the plastic screws that are used for the positioning of the wire are visible as signal voids in the $|B_1^+|$ distribution. Also, the measured distributions and the relative errors show more grainy distributions attributable to the noise in the MR image. The long wavelength at 1.5T causes the harmonics in the SPACY description of the background field to vary smoothly, which makes the decomposition relatively insensitive to noise, small signal voids, and other abrupt field variations. Therefore, the overall distributions seem to be captured accurately with the fit using equations 4.8 and 4.9 despite the noise. This fit once again provides us with an estimate of the TM and TF. The TMs for the straight wires aligned with the main magnetic field direction are shown in figure 4.9. The top subfigures show the TM and its first row (i.e., the TF) for the bare wire and the bottom subfigures show the results for the insulated wire. The TMs for the other orientations can be found as supplementary figures in appendix C. All the normalized TFs as determined in the various orientations are shown in figure 4.10.
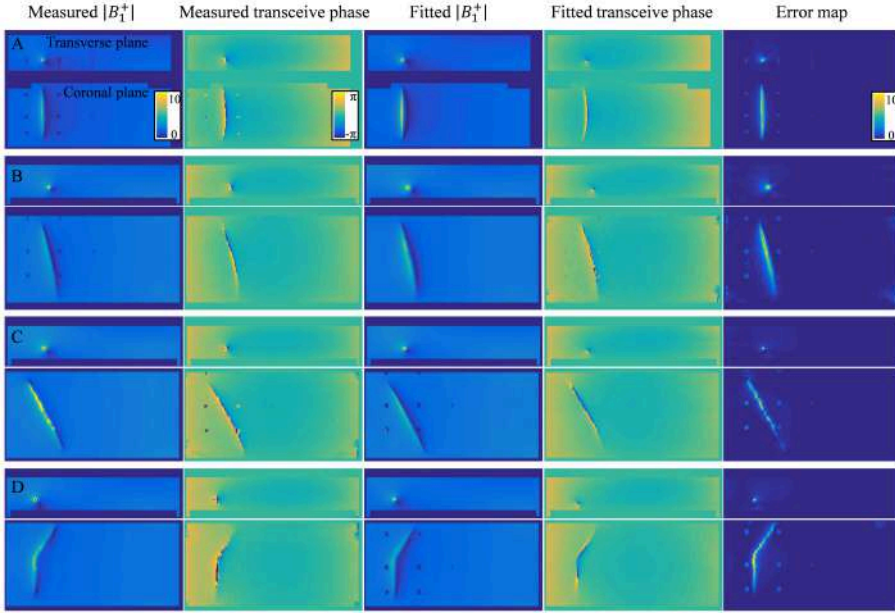
Figure 4.7: The measured B_1^+ magnitude and transceive phase distribution around the bare 20 cm wire in orientations (A), (B), (C), and (D) are shown on the left. These fields are fitted with equations 4.8 and 4.9 using the minimization given in equation 4.10 . The results from these fits are shown in the third and fourth columns. The absolute error is shown on the right. Despite the evident similarity between the distributions, some discrepancies, especially around the wire, remain present.

Discussion

A new method has been developed that is able to measure the TF of a medical implant using only MRI experiments. The method is based on the previously introduced TM. The first row of the TM is the TF. Both the TM and the B_1^+ background field are parameterized by a small set of unknowns (~10 and ~40, respectively). This enables the measurement of the TF by acquiring only two MRI data sets that provide the B_1^+ magnitude and transceive phase distributions. The experimentally determined TFs are in good agreement with the reference TMs with Pearson correlation coefficients of R = 0.971 and R = 0.952 for the bare and insulated test implant, respectively. The presented method enables assessment of the TF using only MRI experiments without the need for dedicated hardware, modifications to the implant, or simulations of the setup.
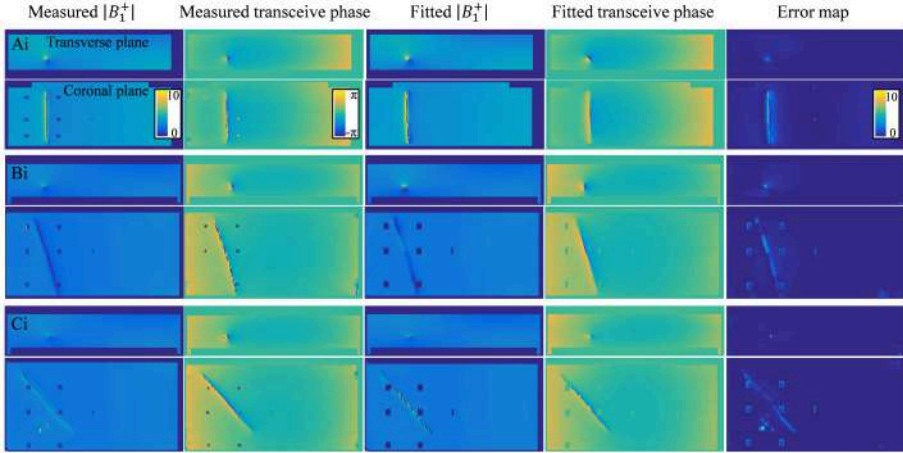
Figure 4.8: The measured B_1^+ magnitude and transceive phase distribution around the insulated 20 cm wire in orientations A_i, B_i and C_i are shown on the left. These fields are fitted with equations 4.8 and 4.9 using the minimization given in equation 4.10. The results from these fits are shown in the third and fourth columns. The absolute error is shown on the right. Again, some discrepancies, especially around the wire, remain present

Measurement of the TF by MRI as presented here is only feasible for elongated "piecewise constant" implants, that is, elongated implants that consist of a small number of segments where each segment has constant effective wave propagation properties. The different segments can have different wave propagation constants, similar to the 3-segment insulated wire parameterization that was used as a test implant throughout the work presented here. Only then is the previously introduced attenuated wave model for the TM applicable. For more complex implants, the parameterization might become more complex, making the optimization in equation 4.10 numerically challenging.

Both results presented in figure 4.6 and figure 4.10 reveal minor deviations between the normalized TF as determined by the presented method and the reference. Particularly for the in silica experiment (figures 4.3, 4.4, and 4.5), these deviations might seem remarkable given that the input fields are simulated and do not have any imperfections that are typical for measured field distributions. The deviations likely originate from simplifications that were made for the presented method that are approximately, but not entirely, valid. The most important assumption is the transceive phase approximation required for the background field determination. The phase of the B+1 field
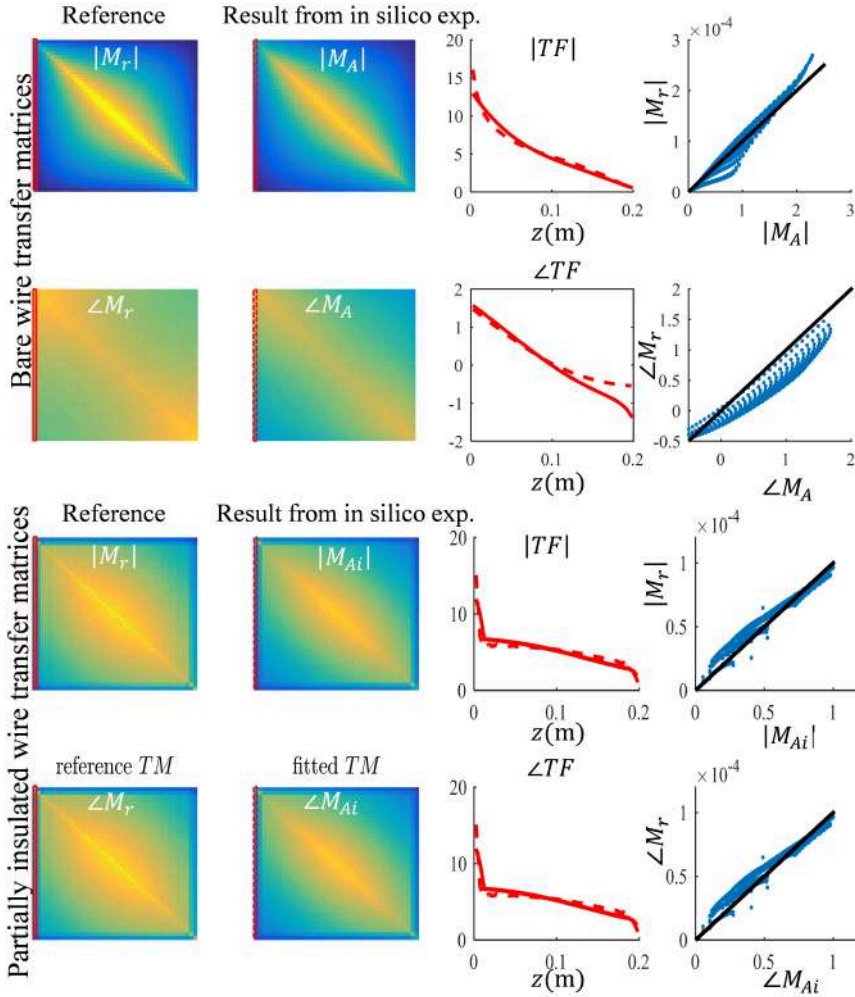
Figure 4.9: Two examples of the TF and TM that follow from the fit of the fields shown in figures 4.3 and 4.4. The results for the straight wire aligned with the z-axis are displayed here, that is, from distribution (A) and (A$_i$) in figures 4.3 and 4.4, respectively. Ideally, the TMs that follow from the full field fit should be identical to the reference TMs and lie the line x = y in the outmost right figures. This is not exactly the case, but Pearson correlations are high, with R = 0.983 and R = 0.962 for the bare and insulated wire, respectively

Correlation coefficients between the TFs of the bare wire

Pearson corr.	Reference	Trajectory A	Trajectory B	Trajectory C	Trajectory D
Reference	1	0.981	0.986	0.982	0.967
Trajectory A		1	0.999	0.992	0.996
Trajectory B			1	0.993	0.994
Trajectory C				1	0.986
Trajectory D					1

Correlation coefficients between the TFs of the insulated wire

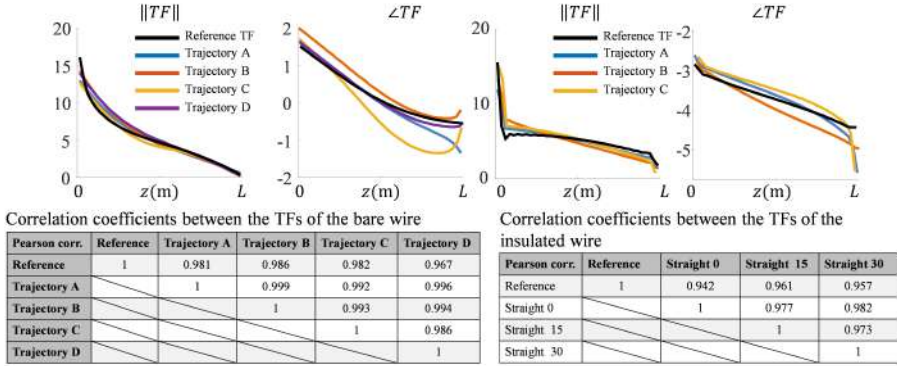| Pearson corr.	Reference	Straight 0	Straight 15	Straight 30
Reference	1	0.942	0.961	0.957
Straight 0		1	0.977	0.982
Straight 15			1	0.973
Straight 30				1

Figure 4.10: The normalized TFs that follow from the fits of the measured fields displayed for the bare wires and insulated wires in figures 4.8 and 4.9, respectively. The TFs found from fitting the fields for the different wire trajectories resemble the gold-standard TF and each other. The correlation coefficients are above 0.98 for the bare and above 0.94 for the insulated wires. The agreement found between the TFs can be viewed as a validation of the measurements

is not exactly equal to half the transceive phase with deviations ranging from –0.29 to +0.30 radians in simulations. The maximal relative overestimation in the B+1 phase distribution compared to half the transceive phase is 16.7%, and the maximal relative underestimation is 12.3%. Nevertheless, the overall distributions are similar, with an average relative error of 3.6% and a Pearson correlation of 0.924. The largest errors occur at the edges of the phantom. Overall, this minor violation of the transceive phase approximation partly explains the modest deviations in figures **??** given that it will result in inaccuracies in the electric field determined from the derivative of the complex $B_1^+{}_{bg}$.

However, for setups where the transceive phase approximation breaks down, the method in its current form will show larger deviations. The deviation will lead to inaccuracies in the incident electric field determined from the complex $B_1^+{}_{bg}$ using equation 4.3. Hence, caution has to be taken when imaging is performed with another transmit coil or when the implant is positioned away from the center of the birdcage coil. The RF interactions of an implant can, however, be assessed in a different imaging location and with a different coil than the actual examination. This freedom should be used to make sure the assumption underlying equation 4.3 is accurate.

Second, the assumption that the z-component of the RF magnetic field is negligible, that is, the electric field is fully oriented in the z-direction, might

not always hold. In the phantom experiment presented here, on average 80.3% of the magnitude of incident electric is contained in its z-component. At the location of the implant, this percentage is 97.8%. So, the incident electric field can be considered to be z-directed. This is not generally true and especially starts to fail around material interfaces in the xy-plane. Both the x- and y-component of the electric field as well as the error in the transceive phase approximation are considered to be responsible for the discrepancy between the reference TFs and the ones determined with in silica experiments are shown in figure 4.5.

Obviously, even more discrepancies are visible between the experimentally determined TM or TF and the reference. One reason can be minor differences between the experimental and the simulation setup. For example a potential cause of deviation is the difference in material properties of the insulation layer around the insulated wire, which is considered to be polyvinyl chloride and can have quite a significant effect [**?**].

The choice for the multi–flip angle $|B_1^+|$ mapping technique is based on previous work [45]. This is a time-consuming method (3 minutes 13 seconds per flip angle for 20 flip angles, leading to a total acquisition time of 1 hour 4 min-utes 20 seconds) and requires acquisitions with a high nominal flip angle (100°). Other B_1^+ mapping techniques [73, 84, 85] will be faster, but may not have the required dynamic range. Optimization of the B_1^+ mapping sequence is not yet performed and may speed up the presented method.

Furthermore, the implants used throughout this work do not generate a susceptibility artifact. Some implants induce B_0 distortions, especially when they are not aligned with B_0, which result in distinctive signal voids and blooming artifacts and also require adaptations to make customary B_1^+ -mapping techniques work [101]. Especially more bulky implants will require additional effort to make the presented method applicable. For the proof of principle presented here, the variable flip angle (VFA) has shown to be the most suitable B_1^+ mapping technique, but for different experiments, other choices might prove more fitting.

To validate the presented method, an independent second electric field exposure can be used to perform separate measurements and verify whether the same TF is found. Such a different incident electric field distribution is obtained by repositioning the implant in the phantom. The implants in the various trajectories will be exposed to different incident electric fields, and hence various currents will be induced. Nevertheless, the TMs and TFs distilled

from fitting the B_1^+ magnitude and transceive phase distributions should be, in principle, the same given that it is generally assumed that different loading conditions have negligible impact on the TM. All measured TFs turn out to correlate strongly.

Conventionally, transfer functions are determined in homogeneous, liquid phantoms. Only then is the measurement probe able to scan along the full length of the implant. The method described here is based on MR images, and hence the measurement phantom does not need to be fluid or homogeneous. Therefore, this method bears potential for measuring the transfer function in heterogeneous media, such as inhomogeneous phantoms or even corpses. For this purpose, some difficulties still need to be addressed. One of these is that the attenuated wave model will presumably require a location-dependent wave propagation constant to describe the attenuation and wavelength of the currents in the implant. Likewise, the SPACY decomposition of the background field might need to be extended with solutions to the Helmholtz equation for inhomogeneous media. However, a recent study shows that even for inhomogeneous situations, the SPACY decomposition seems to work adequately [87].

In principle, the presented method could even be considered as a stepping stone for the measurement of the TF in vivo. However, for this purpose, even more challenges need to be addressed. First of all, a significant speedup of the measurement is necessary. This would require the adaptation of the method such that it can use a local receive array, rather than the birdcage body coil, for receive as presented here. Furthermore, a fast, low-power B_1^+-mapping technique with large dynamic range would be needed. If in vivo TF determination becomes possible, certain worst-case assumptions could be relaxed, possibly enabling scanning of patients with implants of which the RF heating potential is unknown or has resulted in a contraindication for MR exams. MR-based TF determination could furthermore lead to faster scanning or improved image quality in the case of subjects with MR conditional implants.

Explaining current patterns on implantable medical devices during MRI using the transfer matrix

Tokaya, Janot P.

Luijten , Peter R.

van den Berg, Cornelis A.T.

Raaijmakers, Alexander J.E.

Chapter 5

Abstract

Introduction: In this work a simulation study is performed to gain insights in the patterns of induced radiofrequency (RF) currents for various implant-like structures at 1.5T. The previously introduced transfer matrix (TM) is used to determine why certain current patterns have a tendency to naturally occur. This can benefit current safety assessment techniques and may enable the identification of critical exposure conditions.

Theory & Methods: The induced current on an elongated implant can be determined by multiplication of the incident electric field along the implant with its TM. The eigenmode spectrum of the TMs for various lengths and various types of implants are determined. The eigenvector with the highest eigenvalue describes the incident electric field pattern that induces the highest current which in turn will lead to highest heating. Subsequently, a statistical probability analysis is performed using a wide range of potential incident electric field distributions in a representative human subject model during a 1.5T MR exam which are determined by means of electromagnetic FDTD simulations. These incident electric field distributions and the resulting induced current patterns are projected onto eigenvectors of the TM to determine which eigenmodes of the implant dominate the current patterns.

Results: The eigenvectors of the TM of bare and insulated wires resemble sinusoidal harmonics of a string fixed at both ends similar to the natural-current distribution on thin antennas [102]. The currents on implants shorter than 20cm are generally dominated by the first harmonic (similar to half a sine wave). This is firstly because for these implant lengths (relative to the RF wavelength), the first eigenvalue is more than three times bigger than the second showing the ability of an implant to accommodate one eigenmode better than another. Secondly, the incident electric fields have a high likelihood (95,7%) to project predominantly on this first eigenmode.

Conclusions: The eigenmode spectrum of the TM of an implant provides insight into the expected shape of induced current distributions and worst-case exposure conditions. For short implants, the first eigenvector is dominant. In addition, realistic incident electric field distributions project more heavily on this eigenvector. Both effects together cause significant currents to always resemble the dominant eigenmode of the TM for short implants at 1.5T.

Introduction

Medical implants in patients undergoing MRI investigations can pose a safety risk. One of the main safety risks is the hazardous interaction of the implant with the transmit RF field of the MRI system. Conductive structures (like metallic implants) when exposed to the RF electric field component of the RF field tangential to the implant will accommodate currents. The currents cause charge accumulation resulting potentially into sharply peaked electric fields and local tissue heating predominantly occurring at lead tips [25]. Especially elongated implants like guide wires [25], implanted pacemakers leads [26], ECGs [27] and deep brain stimulators [28,29] have shown a capacity to pick-up and focus energy from RF electric fields. Temperature rises of up to 48° C and 20° C degrees have been found in phantom [30] and pig [26] experiments for guide wires and pacemaker leads respectively.

This tip heating can be calculated from the incident RF electric field with an implant characteristic called the transfer function(TF) [41]. The TF describes the contribution of a localized incident electric field at a certain position along the length of the implant to the scattered field at the tip. Thus, given a distribution of the incident electric field along the implant the scattered field at the tip can be calculated. Recently, the concept of the transfer function has been extended to the transfer matrix(TM) [92]. The TM computes the entire induced current profile over the implant from of an incident electric field along the length of the implant. This current can subsequently be used to calculate tip heating [37,103].

The extension of the TF to the TM was originally developed for MR based TF determination [92]. In this work we will show that the TM also provides information about the shape of the current patterns that occur on implants and on worst case electric field exposure conditions. It will be shown that naturally occurring current patterns can be determined from the eigenmode spectrum of the TM of an implant because they correspond to the eigenmodes with the highest eigenvalues.

Firstly, the TMs of various elongated implant structures will be determined through electromagnetic simulations. Subsequently, the eigenmode spectrum of these TMs is calculated. Secondly, realistic incident electric field distributions inside a representative patient model, which has been extensively researched [104–106], are determined with simulations. These electric fields are used to compute potential currents in various implants using their TMs. The currents are subsequently evaluated in a probabilistic approach to determine

what shapes of current distributions on the implant are most likely induced. It is shown that the TM of an implant provides its intrinsically supported current patterns which can help to identify hazardous and safe exposure conditions and provides insights into the resonating behavior of implants.

Methods

Determination of the TM

Determination of the TM The TM, M, relates the induced current pattern over the implant (described by vector I) to the incident electric field along the implant (described by vector E) that caused it, through:

$$I = ME. \tag{5.1}$$

Bare and partially insulated wires of various lengths are investigated. Their TMs are computed from electromagnetic simulations(Sim4Life, ZMT, Zurich, Switzerland) where currents are induced in the various implants by localized electric field excitation created with plane wave sources [92] of 5mm width. The simplest implant is a bare wire with a 2.5 mm diameter, for which the TM is determined for wire lengths of 10cm, 20cm 30cm and 40cm with a resolution corresponding to the width of the plane wave sources. The TM of the 20 cm wire is also determined for a situation where one end of the wire is attached to a cube of perfect electric conductive material with 4 cm edges intended to mimic an implantable pulse generator (IPG). A third 20 cm wire is composed of an 8 cm insulated region and a 12 cm bare region to explore the effect of an impedance transition. Another set of wires for which the TM is determined is insulated except for a small bare part of 1cm at both ends. Also, these wires were studied for a wire length of 10cm, 20cm 30cm and 40cm. An overview of all investigated structures is shown in table 5.1. All structures are gridded with a 0.2 mm isotropic resolution perpendicular to the long axis of the implant and 0.5 mm resolution along the long axis

Note that the simulation method of subsequently repositioned localized electric field excitations for TM determination used here is equivalent to the piecewise excitation method [41, 42] used for transfer function determination with the distinction that the entire induced current distribution and not only the tip field is monitored.

The conductive parts of the wires are made of copper with a conductivity (at 64MHz) of $5.8 \cdot 10^7$S\m. The 0.5mm thick insulation layer has a relative permittivity of 3 and is non-conductive. These generic structures were
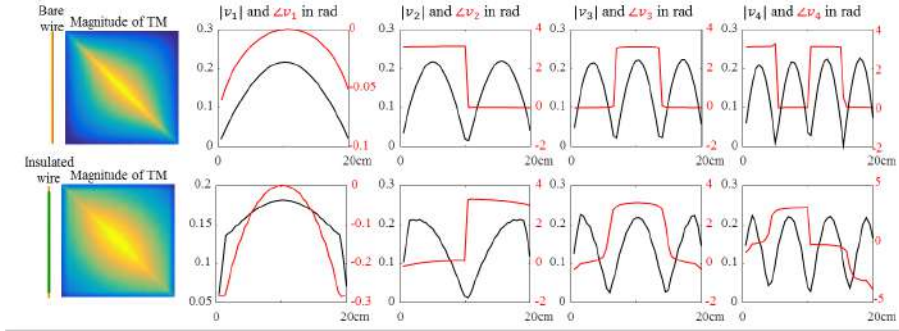
Figure 5.1: The TM of the bare (top) and insulated wire (bottom) of 20cm length together with its first 4 eigenvectors. The eigenvectors are sine shaped modes with increasing number of nodes on the length of the implant. For the structures investigated in this work the first eigenvector always is the mode with smallest number of nodes. This potentially changes if the length of the implants exceeds the maximal length investigated here and will depend on the ratio between the wavelength and the length of the implant. It will result in a different ordering of the modes, but not in an alteration of their overall appearance.

used in this exploration because their TMs will vary significantly and show different responses to an incident electric field. Furthermore, the bare and insulated wires of 20cm length have known properties and have been used in other works [41, 59, 66]. All the structures were simulated in a saline solution (relative permittivity of 78 and a conductivity of 0.47 S\m) that filled the entire computational domain. These properties correspond to the medium described in test standards [61].

Once the TM of an implant has been simulated, the eigenvalues and eigenvectors of this matrix of size NxN are determined with MATLAB (Math-Works, Natick, MA). These eigenvectors give the characteristic eigen current modes in the implant. One can always decompose (part of) the incident electric field in the first k eigenvectors of the TM. Therefore,

$$I = ME = M(\alpha_1 v_1 + \alpha_2 v_2 + \ldots + \alpha_k v_k + E_r).$$ (5.2)

Here v_i stands for the i$^{\text{th}}$ eigenvector, v_i of M. α_i is the coefficient in the eigenvector decomposition. It is computed by taking the normalized inner product of the corresponding eigenvector with the incident field, i.e. $\vec{v_i} \cdot (\vec{E_{inc}})/ \|E_{inc}\|$. E_r is the part of the electric field that is not decomposable into the first k eigenvectors of the TM and is generally extremely small after

inclusion of only a few eigenvectors (for example, already on average 53.3% of E_{inc} is projected onto the first eigenvector, i.e. for all incident electric fields the average residual E_r is 46.7% of the initial E_{inc} showing that the typical incident electric field distribution has a large component that can be described by the first eigenmode of the TM). Hence,

$$I \approx (\lambda_1 \alpha_1 v_1 + \lambda_2 \alpha_2 v_2 + \ldots + \lambda_k \alpha_k v_k). \qquad (5.3)$$

Now it is clear that particularly the eigenvector with the highest eigenvalue has the potential to manifest itself as induced current pattern when it is 'excited' because the contributions of the various eigenvectors are weighted by the corresponding eigenvalue. This occurs when the inner product between the electric field and this eigenvector is large. The first two eigenvectors of the various structures are shown in table 5.1.

Determination of possible electric field exposures

Another FDTD electromagnetic simulation is performed to determine realistic incident electric field distributions. These distributions are determined from a simulation of "Duke" from the Virtual Family [107] positioned for a cardiac MRI in a 1.5 T (or 64MHz) highpass birdcage coil, driven in quadrature. The simulation setup is shown in figure 1. The birdcage coil has 16 rungs, a 35.2 cm coil radius and 42 cm rung length. The RF shield has a 37.2 cm radius, 70 cm length and is composed of perfect electric conductor. Duke was resolved in 2 mm isotropic grid. The additional gridlines of the birdcage coil lead to an average resolution of 1.93x1.94x2mm. The simulation time is set to 100 periods leading to a final power balance of 100.53%.

From the electric field distribution inside Duke, that is predominantly z-oriented, the potential electric field exposures along the implant are extracted. For this purpose, the complete set of possible positions of the implant within the model is evaluated and for each position the incident electric field E_z along the implant is extracted. To speed up this process the electric field inside duke is linearly interpolated to a 2x2x5 mm resolution. The resolution in the z-direction corresponds to the resolution of the TM, i.e. the width of the plane wave boxes used in the piecewise excitation method. For all positions, the wires are assumed to be z-oriented because this configuration will in general lead to worst case exposure conditions and are most likely to occur for linear implants. All connected E_z field distributions of 10cm, 20cm, 30cm and 40cm length inside the human model are extracted from the interpolated electric field, i.e. the complex E_z values inside respectively all 20, 40, 60 and 80 connected 'Duke'

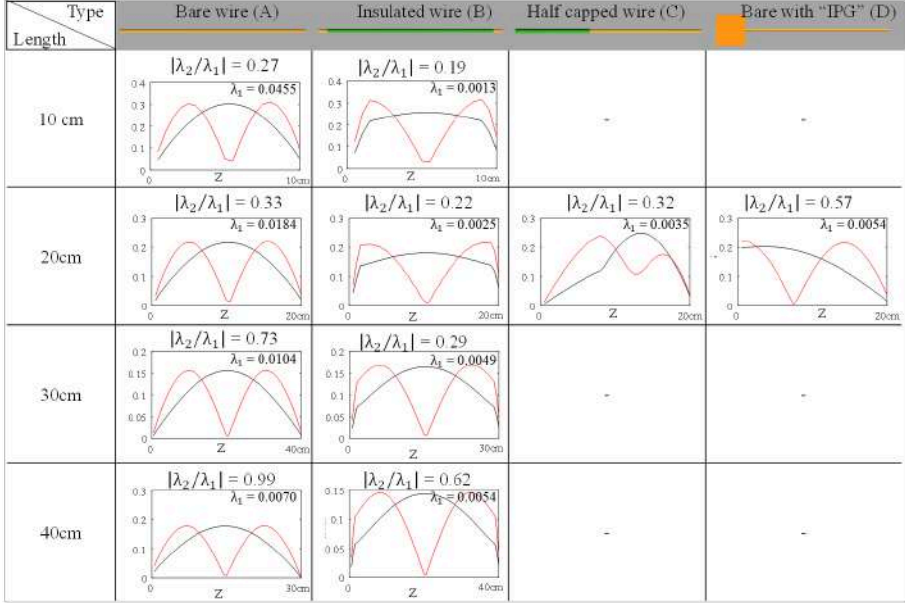| Length \ Type	Bare wire (A)	Insulated wire (B)	Half capped wire (C)	Bare with "IPG" (D)
10 cm	$\|\lambda_2/\lambda_1\| = 0.27$ $\lambda_1 = 0.0455$	$\|\lambda_2/\lambda_1\| = 0.19$ $\lambda_1 = 0.0013$		
20cm	$\|\lambda_2/\lambda_1\| = 0.33$ $\lambda_1 = 0.0184$	$\|\lambda_2/\lambda_1\| = 0.22$ $\lambda_1 = 0.0025$	$\|\lambda_2/\lambda_1\| = 0.32$ $\lambda_1 = 0.0035$	$\|\lambda_2/\lambda_1\| = 0.57$ $\lambda_1 = 0.0054$
30cm	$\|\lambda_2/\lambda_1\| = 0.73$ $\lambda_1 = 0.0104$	$\|\lambda_2/\lambda_1\| = 0.29$ $\lambda_1 = 0.0049$		
40cm	$\|\lambda_2/\lambda_1\| = 0.99$ $\lambda_1 = 0.0070$	$\|\lambda_2/\lambda_1\| = 0.62$ $\lambda_1 = 0.0054$		

Table 5.1: The first and second eigenvector of the TMs of the various investigated structures are shown as black and red lines respectively. The fraction between the corresponding 1st and 2nd eigenvalue, i.e. λ_1 and λ_2, increases with increasing implant length. This shows that the current pattern on longer wires will start to become a superposition of multiple eigenvectors, whereas the current pattern on the shorter implants is essentially dominated by the first eigenvector. Note that for the lengths displayed here the first eigenvector always has one maximum. For longer implants (or higher frequencies) the the eigenvector with the highest eigenvalue can also have multiple maxima.

voxels for the 10cm, 20cm, 30cm and 40cm wire create the distribution of E_{inc} fields. The distribution of incident electric fields, created in this manner, is assumed to be a representative collection of potential electric field exposures.

Determination of possible induced current patterns

The TM is applied to gain insight into the current patterns that can be excited on an implant given the collection of potential incident electric field exposures. Multiplication of the transfer matrix with all possible incident E_z distributions will result in the corresponding current patterns. Note that the highest E_z does not necessarily correspond to the highest current.

Next to a direct calculation of the currents on the wires a more detailed analysis of the resulting current patterns is performed based on the eigenvectors
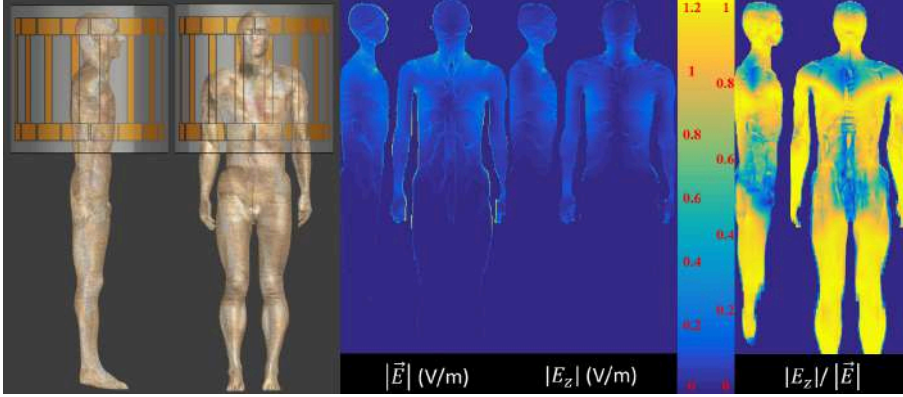
Figure 5.2: The simulation setup of Duke in the birdcage is shown on the left. The electric field distributions (scaled to 30 μT peak B_1^+), resulting from the simulations performed with this setup, show that the electric field inside Duke is predominantly z-oriented. From the electric field distribution inside Duke all 10cm, 20cm, 30cm and 40cm distributions in the z-direction are extracted. These distributions represent all possible electric field exposures that an implant of identical length directed along the z-axis (often worst case) can encounter.

of the TM. Firstly, all the electric field distributions are decomposed into the eigenvectors of the TM to identify modes that are 'excited' more heavily. The projection of eigenvector v_i onto a particular E_z distribution will be denoted with α_i, i.e. $\vec{v_i} \cdot (\vec{E}_{inc})/\|E_{inc}\|$. This projection purely displays how efficient an external field can excite certain current modes and contains no information on the ability of an implant to accommodate a certain mode.

Secondly, after obtaining the induced current on the wire by multiplication of E_z with the TM the actual contribution of a particular eigenvector to this distribution will be denoted by β_i, i.e. $\vec{v_i} \cdot (\vec{I}_{ind})/\|I_{ind}\|$. In these projections the weighting due to the magnitude of the corresponding eigenvalue are incorporated. The magnitude of the eigenvalue is a quantitative measure of the ability of an implant to accommodate the corresponding eigenvector.

Results

Figure 5.1 shows the magnitude of the TMs of the bare and insulated wire of 20 cm length with their first 4 eigenvectors. These eigenvectors come in the shape of sine waves with increasing frequency similar to the natural harmonics that appear on a musical string when it is fixed on both ends. The eigenvectors of the bare and insulated wires of other lengths follow similar patterns. The

eigenvectors of the TM of the partially insulated wire shows a resemblance to the harmonics on a string with variable density along the length of the wire. The TM of the wire that is attached to a conductive block has eigenvectors similar to the standing waves in a pipe with one open end (the end attached to the conductive block). This is similar to the current on a quarter wavelength grounded antenna [108]. The endpoint of this implant, where it is attached to the IPG, acts as if it is grounded and hence open. The other end which is embedded in poorly conducting material is closed.

Table 5.1 shows that the bare and insulated implants with a length of 20 cm and shorter have a 1st eigenvalue that is three or more times bigger than the 2nd eigenvalue. For the 20 cm and 10 cm bare wires the second eigenvalue is only 27% and 33% of the first eigenvalue respectively. In the other structures this dominance is also found with an exception of the bare wire connected on one end to a conductive block, which has a second eigenvector that is 57% of the first. The dominant first eigenvalue shows that one specific current pattern (the eigenvector corresponding to this eigenvalue) will have the largest contribution to the overall current distribution. The dominance of certain modes depends on the length of the implant and the wavelength of the RF field in the medium and is related to resonance effects [109]. The wavelength of electromagnetic waves in the test medium at 64MHz is 44cm [110]. The implants shorter than 20cm (less than half a wavelength) can therefore only accommodate a single mode (the one with a single maximum) whereas the 40cm implants are already able to accommodate higher modes as can be seen by the large magnitude of the second eigenvalue.

After the simulation of the incident electric field in the model 'Duke', in total 2.83 million electric field exposures of 10 cm, 2.27 million electric field exposures of 20 cm, 1.85 million electric field exposures of 30 cm and 1.53 million electric field exposures of 40 cm are extracted. When integrating the electric fields over the implant length, the highest electric potentials are 268V, 445V, 572V and 657V for 10cm, 20cm 30cm and 40cm length respectively after scaling the $B_1^+{}_{max}$ of the birdcage coil to 30 μT in the center of the imaging domain.

These electric field distributions are projected onto the first and second eigenvector of the TM of the various implants. The projections are denoted by α_1 and α_2. The ratio between α_1 and α_2/α_1 indicates how strongly an incident electric field couples to the first eigenvector with respect to the second. The distributions of these ratios for all possible electric field exposures are shown

in figure 5.3 as histograms for the bare and insulated wire. Figure 5.3a, for example, shows two graphs. One for the bare and one for the insulated wire, which are more or less similar. The vertical dashed line displays where the ratio α_2/α_1 equals 1. The large majority of the potential incident electric field distributions results in a α_2/α_1 ratio smaller or much smaller than 1 (i.e. the first eigenvector is dominant) with a maximum likelihood around $\alpha_2/\alpha_1 = 0.176$ and 0.171 for the bare and insulated wire respectively. Only in 1.7 and 1.8% of the cases, for the bare and insulated wires respectively, the projection of the incident field on the second eigenvector is larger.

Looking at all histograms, it is clear that for all wire lengths exciting the first eigenvector is more likely than exciting the second eigenvector. This likelihood goes down with increasing implant length from ca. 98% for 10 cm wires to 81% for 40 cm wires. On top of this, in the less likely situation that the incident electric field excites the second eigenvector stronger, the amplitude of that electric field distribution tends to be lower: the worst-case electric fields that have a larger projection onto the second eigenvector (of a bare wire) compared to the first, i.e. $\alpha_2 > \alpha_1$, are respectively only 73%, 47%, 39% and 41% of the highest electric potentials in general. So even though it can happen that the second mode is excited more effectively by an incident field then this will not correspond to the worst-case exposure.

Multiplication of the incident electric fields with the TM results in the total induced currents on the implant. The current distributions are, like the incident electric fields, projected onto the first two eigenvectors of the TM. These projections, denoted by β_1 and β_2, describe to which eigenvector the induced currents are more similar. These values will be influenced by both the effectiveness of the electric field in exciting a certain eigenvector and the ability of the implant to support this mode. In figure 5.4 the maximal current in the implant is displayed against β_2/β_1. In these scatter plots each point represents one potential incident electric field distribution (i.e. one potential implant position in our simulated model Duke). The horizontal position of each point represents the β_2/β_1 ratio. If $\beta_2/\beta_1 > 1$ the current distribution will be more like the first eigenvector. If $\beta_2/\beta_1 > 1$, the current will be more like the second eigenvector or contain even contributions from higher eigenvectors. The vertical position of each point represents the largest current amplitude along the wire for this incident electric field distribution.

For 10cm wires, the large majority of potential incident electric field distributions results in a current distribution along the wire that is highly
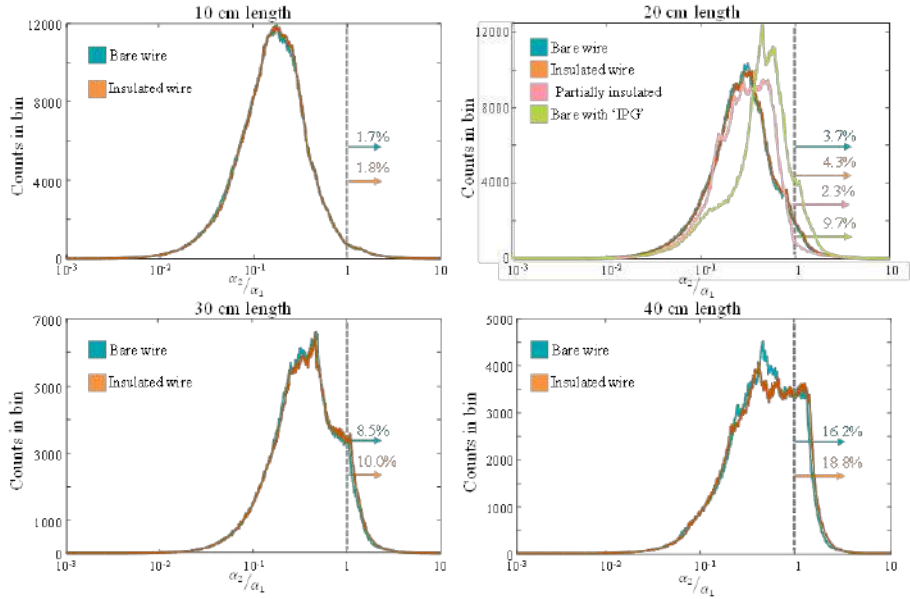
Figure 5.3: The electric field distributions of the various lengths shown in figure 2 are projected onto the first two eigenvectors of the TM of the various implants with the same length. Here, histograms of the fraction between both projection values are displayed. If $\alpha_2/\alpha_1 > 1$, the incident electric field has a larger projection onto the second eigenvector. For the wires shorter than 20cm more than 95% of the electric field distribution are more efficient in exciting the first eigenvector of the TM, with exception of the bare wire connected to a conductive block.

similar to its first eigenvector ($\beta_2/\beta_1 \ll 1$). Only a very small minority of the potential incident electric fields realizes current distributions along the implant that are more similar to the second eigenvector. However, in these situations the maximum amplitude of the induced current is rather low. From figure 5.4 it can be seen that for longer implants the induced currents start to have a larger contribution from the second eigenvector because the entire distribution is shifted towards the region where $\beta_2/\beta_1 > 1$. For all lengths, the amplitude of current distributions that are more similar to the second eigenvector are well below the maximum amplitude of induced currents in general. In addition, this situation is less likely to occur. The distribution of current maxima is on the verge of crossing the $\beta_2/\beta_1=1$ line for the 40cm bare wire. This indicates that at 1.5T wires longer than approximately 40cm will start to have a dominant eigenvector with two current maxima.
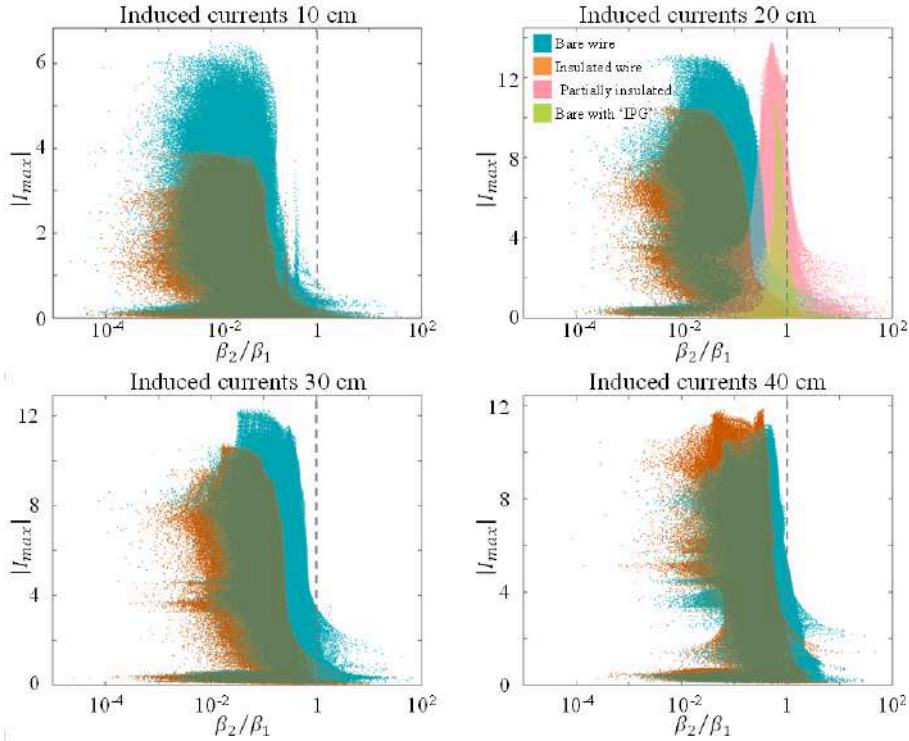
Figure 5.4: The maximum of the current distribution in the wires of various lengths plotted against the fraction between the projection of the 2$^{\text{nd}}$ and 1$^{\text{st}}$ eigenvector of the TM onto this distribution. When this fraction is higher than 1 the current is more similar to the second eigenvector of the TM. From these plots it is clear that the currents induced on the wires predominantly take on a pattern comparable to the first eigenvector which was already to be expected in view of figure 5.3. It is furthermore clear that when a current higher than 50% of the worst-case current is induced the distribution will always be dominated by the first eigenvector.

Discussion

Numerical simulations are performed to determine the TM of various implants. These TMs are subsequently multiplied with a large number of potential incident electric field distributions. These distributions are obtained by extracting the electric field values along the wire for all physically possible positions of the corresponding wire inside a human model. The electric field distribution inside this model is also determined by numerical electromagnetic simulations. The resulting current distributions always tend to appear in a pattern similar to the first dominant eigenvector of the TM of this implant. This especially holds for implants shorter than 20cm. The dominant eigenvectors are always current patterns with one maximum along the implant for the lengths and implants investigated in this work. Note that for longer implants and\or larger frequencies, it is likely that the largest eigenvector may in fact show two maxima and the second eigenvector only has one. This essentially interchanges the eigenvectors when ordered based on the magnitude of the corresponding eigenvalue. The first and second eigenvectors might both contribute significantly for longer implants. The current in the implant can always be decomposed into the eigenvectors of the TM, but generally since the eigenvalues decrease quickly in magnitude a decomposition with only the first few eigenvectors leads to an accurate approximation.

For MRI based current monitoring purposes it is useful to know the shape of the current pattern induced on a wire. This can help improve the accuracy of measured outcomes, allow extrapolation of measured currents to regions outside the field of view of the MRI acquisition or speed up measurements. Knowledge of the TM of an implant is a prerequisite to determine eigenvector resonances and the corresponding current distributions. If an implant with unknown characteristics is present this knowledge might be available or attainable by means of simulations [41, 66] or measurements [42, 43].

The TM of the implants was determined through simulations in a background of high permittivity medium as described in safety standard [53, 61]. This TM is subsequently used to determine currents induced at various locations inside Duke without considering potential changes in the TM due the local dielectric properties. The transfer function, and hence also the TM, is however known to be dependent on the dielectric properties of its surroundings [111–113] and this straightforward translation will introduce an inaccuracy. The extent of this inaccuracy and the way it will influence the current distributions shown in figure 4 is interesting, but is beyond the scope of this paper. An explorative study was presented by Kozlov et al [35].

In this work the electric field distribution inside a human subject is only simulated for one specific model at one specific imaging position in one specific RF coil. Extensions to more locations of Duke inside various coils and using various human models may be necessary to provide confidence that the found results are generalizable to other scenarios. It must be assessed if the millions of incident electric field distributions extracted from this single situation are representative for the other situations as well.

Conclusion

The eigenvectors of the transfer matrix of wire-like implants show similarities to naturally occurring current patterns on thin dipole antennas resembling sinusoidal standing wave patterns. The endpoints of these dipoles are grounded (open) when attached to a 'large' conductive component like an IPG and closed when embedded in a poor conductor like human tissue. This eigenvector spectrum explains why currents induced on short ($L \leq 20$cm) implants have a tendency to appear in one specific pattern. Firstly, the relatively large first eigenvalue shows dominance of the first eigenvector. This is a reflection of the ability of an implant to support one current pattern better than another. The second reason is the likelihood of realistic RF exposures to match these modes. A large set of potential incident electric field distributions was used to show that the large majority of these potential incident fields projects most strongly on the first eigenmode. For all tested implants over 80% of electric field distributions excites the dominant mode more heavily (a number which increases up to 98% for 10cm wires).

If, by coincidence, the second eigenmode is excited more heavily, the corresponding electric field distribution has an integral value far from the worst case (maximally 73%) found in duke. Furthermore, the maximum of the induced current will not reach values close to the potential maximally induced current inside duke (maximally 47%) which can be translated in an approximately four fold [103] decrease in heating.

So, if strong heating is present due to an implant the current pattern causing it, will reflect the dominant eigenvector of its TM. Most severe heating will occur when the incident electric field projects predominantly onto this dominant eigenvector. These insights can be used to aid current monitoring techniques, identify hazardous situations and strategies [72,114,115] to mitigate implant heating.

General Discussion & Summary

Epitome

The presented work is aimed at approaching MR implant safety in a different way. By using the MR scanner as a tool for RF safety assessment a hazard also brings an opportunity. Existing knowledge on RF induced current mapping together with an insight by Feng et al [59] to apply the principle of reciprocity to the RF transfer function of an implant steered the research towards MRI-based measurement procedures of this implant characteristic. To enable MRI-based RF safety assessment of implants it was necessary to generalize the concept of transfer function to a 'transfer matrix' (TM). The matrix description not only facilitates TF determination with MRI, but in itself contains valuable information about the behavior of an implant. Here we provide some additional comments on the results presented in the individual chapters followed by a more general discussion to place this work into perspective.

TF determination with the implant as a transceive antenna

TF determination with the implant as a transceive antenna In chapter one a soldering connection is made between the implant and a coaxial cable thereby

transforming an implant into a transceive antenna. The current induced in the implant in this manner is directly proportional to its TF [66]. Hence its normalized TF can be directly determined from MRI images acquired with this antenna using current mapping techniques. This alternative experimental method allows relatively quick TF determination in a phantom experiment with a high resolution.

The necessary modifications made to the implants did not seem to alter their transfer function. Despite the fact that the structures were poorly matched to the transmit/receive coax cable, which causes poor antenna performance, the current distribution along the implant was resolvable thanks to the strong B1 in the proximity of the implant. In fact, as we realize now, this mismatch plays an important role. Due to the poor matching currents that are running on the implant are not easily transmitted into the coaxial cable. For this reason, the implant is electromagnetically relatively isolated from the coax cable as shown in figure 6.1 and solely the TF of the implant is measured. If a matching network would be added between the coax cable and the implant, the reflections could be avoided. However, the currents on the implant would be able to directly propagate into the coax cable which is not representative of realistic implants. Therefore, for this method the impedance mismatch between cable and implant is essential. The boundary conditions in the experiment should be identical to the actual situation. In reality the implant finds an open end connection, which would result in (near) zero current boundary condition. This is mimicked by the poorly matched coax cable.

Initially, the method had been tried without soldering the cable to the implant but merely placing the open-ended coax cable in close vicinity of the implant ending. However, the power transfer from the cable to the implant was so minimal that the signal was hardly visible even after many averages. The MRI-based assessment of the TF has the advantage that it can be applied in more realistic surroundings. Whereas conventional methods work only in homogenous (liquid) test media the presented method works in solids and can be adapted to work in heterogeneous media. The current technical specification 10974 clarifies transfer functions should be determined in a test medium that is representative for the tissue that the device will be implanted in. Several representative media are suggested. If an implant goes through multiple media (for more than 10% of its cumulative length), or lies on the interface of multiple media the heating in all media should be evaluated. The worst case heating has to be taken from these media and yet still safety margins might be necessary because one homogeneous medium is not an accurate depiction
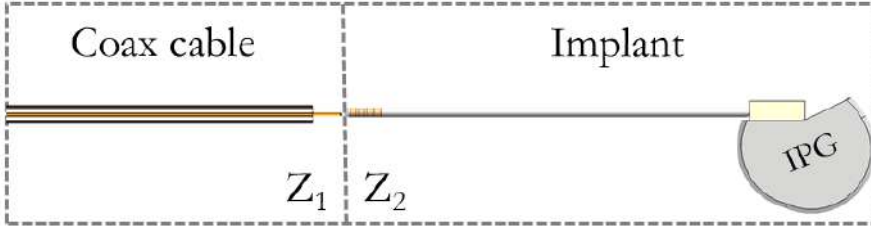
Figure 6.1: The impedance of the coax cable and of the implant are very different such that the reflection coefficient from the implant into the coax cable, i.e. $(Z_1 - Z_2)/(Z_1 + Z_2)$ is close to ± 1. This resembles the poor matching of a realistic scenario between the tip of the implant and the phantom tissue (in experiments) or human tissue (in vivo) around it due to the big difference in conductivity. This makes the reflection coefficient at the tip close to unity and makes it possible to consider the implant as an isolated system for the currents. The same should and incidentally did hold for the suggested MR based method. In this case two structures capable of conducting currents are connected so the mismatch is not a given. If the implant and coax cable would be matched the currents will see an altered reflection coefficient and hence an altered transfer function.

of the actually heterogeneous situation [35, 112, 113]. The MR based method provides possibilities to test how the TF depends on the medium parameters in a more realistic setting and can even be used in animal experiments or corpses.

However, the requirement to solder a coax cable to the implant is a disadvantage because for realistic implants it may damage or alter the implant. In addition, these results have directed our research ambition toward TF measurements in-vivo. Unfortunately, the current method with a cable attached to the implant is fundamentally unsuitable for in-vivo usage.

Contactless transfer function determination
A step towards in-vivo TF determination was made in chapters three and four. In these chapters the implant is no longer attached to a coaxial cable. Not the implant itself, but the regular RF transmit coil of the MRI system (the birdcage body coil) is used for the MR acquisitions from which the TF is determined. Unlike a soldered coax cable, these coils always create a distributed RF electric field. To relate this distributed incident field to an induced current in the implant, the TM was introduced. Its columns give the currents that are induced for an electric field at the location corresponding to this column and thus could be regarded as a sort of scatter current matrix for the implant. The transfer function is hence given by the first column of the transfer matrix

because it describes the current distribution that results from an electric field at the tip of the implant. In this way a single measurement of the current in an implant and the incident electric field that caused it, is actually a collection of equations relating a collection of localized electric fields (a discretized version of the incident electric field distribution) to a current distribution. The matrix contains more unknowns than the TF, but conveniently the columns and rows are related. This is a consequence of the fact that the same physical properties of the implant govern the way currents are induced for electric fields incident on various locations of the implant and a symmetry introduced by the principle of reciprocity.

For the implants used throughout this work an analytical description based on a transmission line model of forward and backward propagating current waves reflected at impedance boundaries is used to parameterize the TM to reduce the number of unknowns in the TM. Despite its simplicity, e.g. ignoring evanescent higher order wave effects and restraining to a 1D description, the model was able to accurately describe the TMs that resulted from simulations. The model was used to describe the TM of bare and partially insulated wires with a maximum of two impedance transitions. The current has a different propagation constant in the bare and the insulated parts of a wire. This is equivalent to a wire embedded into two different media. Extensions to the model to include three or more impedance transitions are possible but will make the derivation in the appendix of chapter three more cumbersome and increase the number of unknowns. If the TF and TM would be determined in a realistically inhomogeneous environment (e.g. in an animal model or corpse) the number of impedance transitions would even be much larger. In a beneficial scenario, the heterogeneous surroundings of the implant would act as one effectively homogeneous medium to the current waves with one corresponding propagation constant. In the more general case, the model may need to be adapted.

In chapter three the transfer matrix concept combined with the parameterized TM is used to determine the TFs wirelessly. In a known experimental setup the incident electric field is computed with electromagnetic simulations and the current is measured with MRI using $|B_1^+|$ and transceive phase acquisitions [45, 55, 71]. The TFs that are subsequently determined from these quantities closely match ground truth numerical results. The necessity to extract the incident electric field from simulations limits the method applicability to situations where the dielectric properties of the subject and the exact drive and design of the RF coil are known. This knowledge, especially about the

dielectric properties of the subject, is often lacking. Therefore, the method was extended in chapter four to remove the necessity of electromagnetic simulation.

To overcome the requirement of a dielectric model of the human subject to simulate the incident electric field, a measurement method to determine the incident electric field is required. However, MR imaging can only directly depict the magnitude of the transverse magnetic component of the RF field distribution, i.e. $|B_1^+|$. Still, (parts of) the electric field can be determined from MR accessible quantities because Maxwell's equations relate the electric and magnetic component of the electromagnetic field. This is used in chapter four. Some assumptions are required to justify the electric field determination from MR accessible quantities. Firstly, the magnetic field generated by the RF coil is assumed to have a negligibly small z component. This holds especially well in the center of birdcage coils (most often used in clinical practice) but not for regions more distant in the caudal or cranial direction. Furthermore, a significant contribution from $B_{1,z}$ would only be relevant for implants that are not aligned with the z-axis because this component would translate into Ex and E_y contributions. Secondly, the transceive phase approximation ($\angle B_1^+ = \angle B_1^-$) is required to hold in the absence of the implant. This is necessary to determine the phase of the complex B_1^+ field. Another strategy to determine the electric field from the complex B_1^+ could be based on deep learning. It was shown that a convolutional neural network can map the local SAR from MR Dixon images and B_1^+ magnitude and relative phase field maps [116]. A similar approach could be used here to estimate the incident electric field. That would likely still require removal of a region where the scattered field has a significant contribution.

In principle the purely experimental method presented in chapter four can be applied to in-vivo TF determination. In practice, still some hurdles have to be overcome. A speed-up of the presented method is required, which is most likely achievable trough the usage of a faster B_1^+ mapping technique. This method should still be able to determine the actual B_1^+ values in a high dynamic range and therefore standard techniques do not directly provide a viable option. A second hurdle is expected to come from the transceive phase approximation. It holds for spherical or cylindrical phantoms but is less accurate in a human subject. Also, the required transceive phase assumption forces the usage of the bodycoil in receive which is a severe concession in the achievable SNR and therefore acquisition speed. The usage of a local receive array which can be placed closer to the body would give an SNR boost, but makes assessment of the B_1^+ phase challenging. One seemingly easy approach would be to use
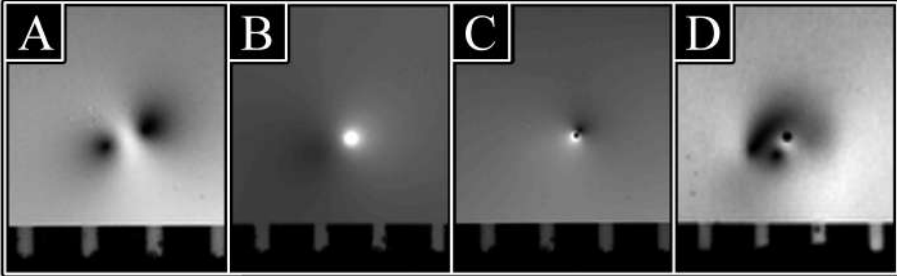
Figure 6.2: A. The artifact around a current carrying wire in a SPGR MR image with a 20 degree flip angle acquired with the birdcage as transmit and receive antenna. B. The $|B_1^+|$ distribution computed from a multi flip angel acquisition. C. The corresponding receive sensitivity. D. The artifact around a current carrying wire in an SPGR MR image with a 20-degree flip angle acquired with a local receive array and CLEAR.

a reference scan for coil sensitivity normalization on the receive array (called CLEAR on Philips MR systems) resulting again in a signal distribution as if the data was acquired with the body coil but still exploiting the higher SNR of the local receive array. However, the reference scan by default has a low resolution to make its acquisition fast. The low resolution gives insufficient accuracy close to the wire to correctly divide out the signals. The results become smudged and are hard to interpret (see figure 6.2D). As a consequence, processing results in erroneous TFs.

Maybe the usage of phase data can be avoided altogether. The image distortion in the magnitude of the B_1^+ field due to the presence of a current carrying wire has a characteristic pattern. In the plane perpendicular to the wire signal enhancements and voids are seen around the wire that alternate in the azimuthal direction (figure 6.2A). The magnitude of the current determines the intensity of the distortions but the phase of the current determines the azimuthal position. Hence, the magnitude data contains information about both the magnitude and the phase of the current. This is possibly exploitable for determination of the TM from only magnitude data. If the phase of the B_1^+ field is no longer required many of the hurdles towards in-vivo TF determination vanish. TF determination from only $|B_1^+|$ data is currently pursued in subsequent studies.

Another potential improvement for the presented MR based TF determination could be found in the usage of multi transmit systems. Some MRI systems have the freedom to modify the transmit field by using multiple antennas in transmission which can be driven independently. By applying different
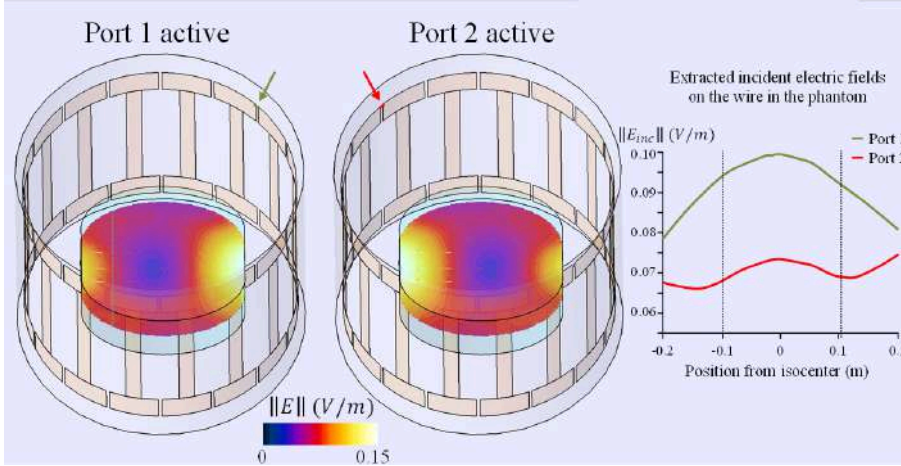
Figure 6.3: The electric field inside the elliptical ASTM phantom created by each of the ports of the birdcage coil. The incident electric fields in the imaging region are shown on the right. The wires, being located between -0.1 and 0.1 meter from the isocenter experience a similar *E*-field from port one and port two (they mainly differ in magnitude). Distinctly different exposure patterns are required to be able to perform independent measurements with the separate ports.

incident electric field distributions, the TM could be determined more precisely through repeated measurements. However, for regular clinical scanners only two transmit channels are available. On top of this, these channels typically result in very similar incident E-field distributions (figure 6.3) in the imaging region of the birdcage coil. A dedicated local transmit/receive coil array can be a solution. Such an array is able to provide a multitude of incident electric fields and induced currents which can improve accuracy of TM determination. It can also allow TM and thereby TF determination for structures with TMs that depends on more unknowns.

Value of the transfer matrix

Actually, the TM contains more information about the implant than just the TF. This is the topic of the last chapter. In chapter 5 we have looked in detail at the potential of the TM in describing an implant. Even if we do not want to resort to MRI based methods, the TM of an implant is experimentally determinable in a similar setup as is used for TF measurements. Similarly the simulation strategy based on localized plane waves for TF determination

107

introduced in chapter 2 can be directly applied to for computation of TMs. The eigenvectors that follow from a singular value decomposition of the TM provides a basis set of current distributions that are accommodated by the implant. It was shown in this chapter that short implants (in the electric sense) have one current pattern (given by the dominant eigenvector) that is particularly effectively supported by the implant. This was shown for simple wires, but it will hold for more complicated structures given they are shorter than half a wavelength of the RF field in the surrounding medium. For longer implants the induced current distributions will become a superposition of multiple patterns. Presumably the current can still be captured by a limited number of contributing patterns given by the eigenvectors of the TM. The eigenvectors of the TM hence provide insight in the induced current patterns that are most likely to occur on the implant.

Furthermore, with the eigenvectors of an implant critical incident electric fields can be determined. The electric fields that have a large projection onto one of the dominant eigenvectors will induce the highest currents. These strong currents will result in severe heating. Therefore, the TM allows determination of electric field distributions that should be avoided if this possibility exists. The worst case tip field will be achieved by an electric field with a phase distribution opposite to the transfer function of the implant but this will not necessarily correspond to the highest induced current.

The continuity equation and the conservation of electric charge make it possible to translate a current distribution into a charge distribution. The electric field will be particularly high around regions where charges accumulate. This happens predominantly at the electrode poles where therapeutic currents are delivered or where the current path encounters a sudden impedance jump. The transfer function is designed to describe the enhancement of the electric field at the tip of elongated implants where it is most significant. In principle other locations of charge accumulation can exist. The identification of these secondary hotspots is possible with the TM.

The future of MR based RF safety assessment

In conclusion, while working on MR based transfer function determination the transfer matrix concept was developed. The TM not only allows MRI based determination of transfer functions without the use of a coaxial contact, it also characterize the RF scattering of an implant. The TM identifies dominant current patterns, critical electric field exposures and secondary hotspots.
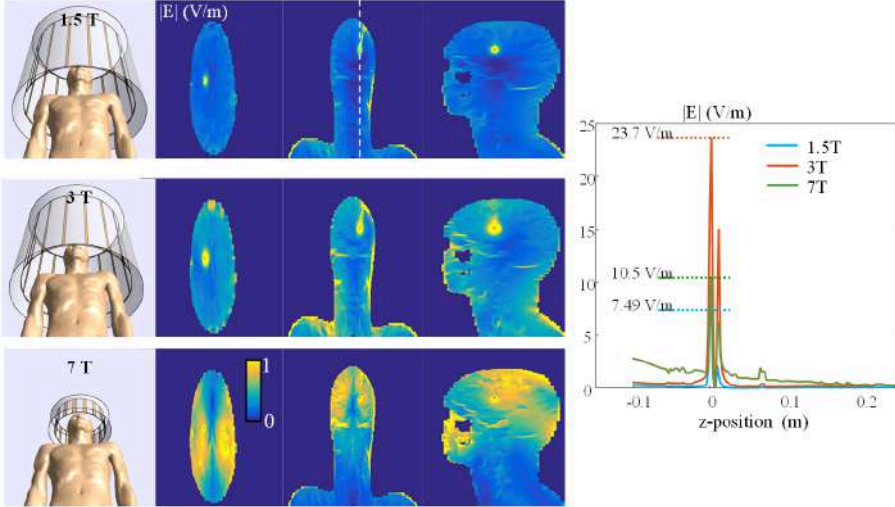
Figure 6.4: Simulations of Duke with a deep brain stimulator like implant in birdcage coils used in clinical practice at 1.5T, 3T and 7T for brain exams. The magnitude of the electric field inside his head is shown in the middle three figures. The scattered field around a deep brain stimulator is highest at 3T and becomes smaller at 7T, contrary to common believe, as can be seen from the line plot depicted in the sagittal plane of the E-field.

The TM enables steps towards in vivo TF determination. Once this becomes feasible, it will help to address the uncertainties currently introduced by translating TFs determined in phantoms to in vivo situations as done in ISO/TS 10974. By removing these uncertainties MR conditional labels will become less stringent thereby improving the potential care MRI can provide to the growing population of patients with MR conditional implants.

Additionally, if in vivo TF determination is possible in an inherently safe way it would allow patient specific safety assessment in the form of a lower power pre-scan that is performed prior to an actual MR exam which should provide subject specific scanning restrictions. Firstly, this potentially improves care for patients with an implant with a MR conditional label through relaxation of worst case assumptions. Currently, worst-case conditions in patient anatomy, implant trajectory within the patient and positioning with respect to the RF transmit coil have to be assumed. These conditions only occur in one unique situation. For all other situation this assumption will introduce unnecessarily stringent RF power restrictions which in turn lead to compromised image quality. Doing an on-site MRI based safety assessment would give

109

information about the specific situation under consideration thereby avoiding the necessity to assume worst case conditions. Secondly, it makes MRI available for patients with an implant of which the RF induced heating is currently unknown. If an implant has unspecified heating risks or is altogether unidentified (despite how curious this sounds, it does happen in practice) the prescan could provide estimates of parameters that are normally described by an MR conditional label. In the latter case of course still, the absence of ferromagnetic materials has to be guaranteed and, for active implants, the implant needs to withstand the harsh electromagnetic surroundings of a MRI scanner, which are essentially hostile to any electronic circuit. Another potential application can be safety assessment of orthopedic implants that are customized during surgery to be the best geometric fit. For this type of implants RF safety assessment is even more challenging because now also the composition of the implant itself is variable. Being able to perform on site safety assessment would be extremely beneficial for this group of patients.

Another promising application of MR based safety assessment is determination of RF associated risks at higher field strengths. Many of the presented methods can be translated to other field strengths directly. Because of the costliness of the procedures described in ISO/TS 10974 to determine MR conditional labels risk analysis is usually only performed for 1.5T scanners because these are most commonly used in clinical practice. Yet, there is a tendency to move to higher field strengths (scanners of 3T, 7T and beyond are becoming more and more prevalent), because of the increased SNR it brings. For these field strengths MR conditional labels are often not provided and contraindications for exams at field strengths larger than 1.5T are given by default since knowledge is lacking. Due to the increasing frequency with field strength the electric field is also increasing. This notion often leads to the misinformed conclusion that heating will become a bigger problem with increasing field strength. Several factors can counteract the effect of the increased magnitude of the electric field. Firstly, the smaller wavelength requires a strong phase gradient in the incident electric field to make current contributions originating from various locations along the wire positively interfere. This is not likely and actually reduction of heating due to cancelling contributions occurs most often resulting in lower scattered fields as can be seen in figures 6.4 and **??**. Secondly the increased loading of the implants at higher frequencies and lower penetration depth of electric fields make it more difficult to induce currents. This furthermore results in a lower Q-factor (more loss for the current per traversed length of the implant) and hence a lower maximal resonance amplitude. For

this reason, risks associated with implants are actually likely to become smaller with increasing field strength beyond a certain point (as can be seen in figures 6.4 and 6.4). Determination of transfer functions at higher field strengths could give experimental insights into the interplay of these effects.

Figure 6.5: Simulation results of bare and insulated copper wires of various lengths (ranging from 3.5 to 44 cm) in a dielectric with a conductivity of 0.47S\m and a relative permittivity of 78 exposed to a constant electric field (1V\m) at 0.5T, 1.5T, 3T and 7T. The insulation layer has a relative permittivity of 2.2. The electric field distributions of several bare wires are shown on top. A line profile through the center of the wire, shown as a dashed green line in the top left distribution, is extracted for each of the simulations. These extracted E-field profiles are shown in subfigure A for bare wires at the four field strengths when exposed to an incident field with constant phase. From these profiles the maximum scattered field is extracted which is shown in subfigure B for bare wires at 1.5T, 3T and 7T exposed to an incident electric field with constant and a worst case phase distribution. In subfigure C maximal tip fields are shown for bare and insulated wires exposed to constant phased E-field. Maximal scattered fields occur at respectively 4.5cm 10cm, 17cm 34cm for bare wires and at respectively 5cm 15cm, 34cm and >44cm for the insulated wires. These lengths correspond to the resonances of the implants at the various frequencies. It should be noted that the maximal scattered field goes down with increasing field strength. Also, insulation in general results in higher scattered fields and longer resonance lengths.

CHAPTER 7
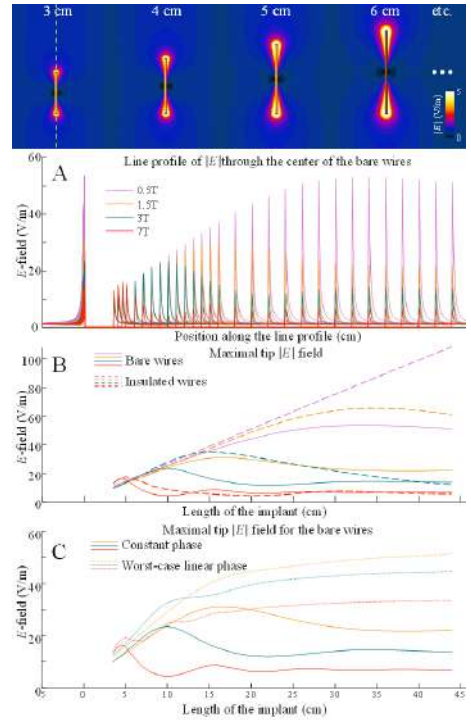
Appendices

Appendix A: Detailed derivation of the parameterized TM (including impedance transitions) using the attenuated wave model

We will start with a derivation of the parameterized TF of the bare wire using the attenuated wave model, i.e. equation 3.1. For the TF derivation the excitation has to occur at $z = 0$. It will create an attenuated wave in the wire of initial amplitude $\sigma_{eff}AE_0$ propagating to the right with complex wave number c_1. This real part of this wave is shown as the black curve in figure S1. The equation describing this wave will be,

$$I_p(z) = \sigma_{eff}AE_0 e^{-c_1 z}. \tag{7.1}$$

This wave travels from $z = 0$ to $z = L$ and hence will be attenuation by a factor $e^{-c_1 L}$. Then it is reflected (say with reflection coefficient Γ_L) before
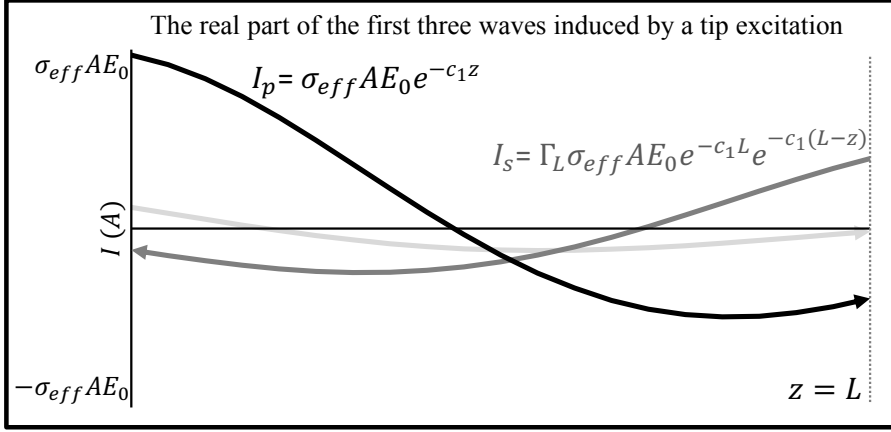
Figure 7.1: The real part of the first three waves in geometric series of the attenuated wave model that is used to derive parameterizations for the transfer functions and matrices of the bare and (partially) insulated wires. In this situation a wire that has a constant wave number along its length is considered.

it propagates back to position z. This second wave is shown as the dark grey curve in figure S1. The equation describing this wave will be,

$$I_{sL}(z) = \Gamma_L \sigma_{eff} A E_0 e^{-c_1 L} e^{-c_1(L-z)} = \Gamma_L \sigma_{eff} A E_0 e^{-2c_1 L} e^{c_1 z}. \qquad (7.2)$$

This wave will in turn reach $z = 0$ and again be reflected. This tertiary wave is shown as the light grey curve in figure S1. The equation describing this wave will be,

$$I_{sL0}(z) = \Gamma_0 \Gamma_L e^{-2c_1 L} \sigma_{eff} A E_0 e^{-c_1 z}. \qquad (7.3)$$

Note this equation is the same as equation 7.1 but here attenuated with a factor $\alpha = \Gamma_0 \Gamma_L e^{-2c_1 L}$ (the attenuation that occurs after one forward and backward propagation and corresponding reflections through the wire). This iterative process continues indefinitely leading to a total sum of waves given by equation 3.1 in chapter 3, i.e.

$$I(z) = \sigma_{eff} A E_0 (e^{-c_1 z} + \Gamma_L e^{c_1(z-2L)})$$
$$\left(1 + \Gamma_0 \Gamma_L e^{-2c_1 L} + (\Gamma_0 \Gamma_L e^{-2c_1 L})^2 + ...\right) \qquad (7.4)$$

We will continue with a detailed derivation of equation 3.3 describing the parameterized TM of a wire without impedance transitions, e.g. a wire that

has the same electromagnetic properties along its entire length. The electric field excitation is now discretized because in practice it always has a certain finite width. This width determines the resolution in which the TM and TF are resolved. If the electric field $E(z_j)$ is incident on the wire at $z = z_j$ it will create a (primary) current wave given by,

$$I_p(z_i) = \sigma_{eff} A E(z_j) e^{-c_1 |z_i - z_j|}. \tag{7.5}$$

This wave reaches both ends of the wire where it will be reflected in the opposite directions with initial amplitudes, $I_{s0}(0) = \Gamma_0 \sigma_{eff} A E(z_j) e^{-c_1 z_j}$ and $I_{sL}(L) = \Gamma_L \sigma_{eff} A E(z_j) e^{-c_1 (L - z_j)}$ at $z = 0$ and $z = L$ respectively. These reflected waves will propagate through the implant for which the wave equations will be,

$$I_{s0}(z_i) = \Gamma_0 \sigma_{eff} A E(z_j) e^{-c_1 z_j} e^{-c_1 z_i} \tag{7.6}$$

$$I_{sL}(z_i) = \Gamma_L \sigma_{eff} A E(z_j) e^{-c_1 (L - z_j)} e^{-c_1 (L - z_i)} \tag{7.7}$$

These waves will again reach either end of the implant and get reflected once more. The waves after this second reflection are described by,

$$\begin{aligned} I_{s0L}(z_i, z_j) &= \Gamma_0 \Gamma_L \sigma_{eff} A E(z_j) e^{-c_1 z_j} e^{-c_1 L} \\ &= \Gamma_0 \Gamma_L e^{-2c_1 L} A E(z_j) e^{-c_1 z_j} e^{c_1 z_i} \end{aligned} \tag{7.8}$$

$$\begin{aligned} I_{sL0}(z_i, z_j) &= \Gamma_0 \Gamma_L \sigma_{eff} A E(z_j) e^{-c_1 (L - z_j)} e^{-c_1 (L - z_i)} \\ &= \Gamma_0 \Gamma_L e^{-2c_1 L} A E(z_j) e^{c_1 z_j} e^{-c_1 z_i} \end{aligned} \tag{7.9}$$

After a third reflection the wave equation will once more be the same as the first reflected waves but attenuated with a factor α. This process can again be continued indefinitely. The sum of all reflected waves hence will be,

$$I_{rall}(z_i) = \sigma_{eff} A E(z_j) \Big(\Gamma_0 (e^{-c_1 (z_j + z_i)} + \Gamma_L e^{-2c_1 L} e^{-c_1 (z_j - z_i)}) + ...$$

$$\Gamma_L e^{-2c_1 L} \big(e^{c_1 (z_j + z_i)} + \Gamma_0 e^{c_1 (z_j - z_i)} \big) \Big) \sum_{n=0}^{\infty} \alpha^n \quad (7.10)$$

The sum of these attenuation factors is a converging geometric series, hence the total current distribution will be,

$$I(z_i) = \frac{\sigma_{eff} A E(z_j)}{1 - \Gamma_0 \Gamma_L e^{-2c_1 L}} \Big(\Gamma_0 e^{-c_1 (z_j + z_i)} + \Gamma_L e^{-2c_1 L} e^{c_1 (z_j + z_i)} + ...$$

$$\Gamma_L \Gamma_0 e^{-2c_1 L} \big(e^{-c_1 (z_j - z_i)} + e^{c_1 (z_j - z_i)} \big) \Big) + I_p \quad (7.11)$$

This results, after some arithmetic, in equation 3.3 that was mentioned in the theory section that relates an incident electric field at $z = z_j$ to an induced current distribution,

$$I(z_i) = \frac{\sigma_{eff}AE(z_j)}{1 - \Gamma_0\Gamma_L e^{-2c_1L}}\left(\sqrt{\Gamma_0\Gamma_L e^{-2c_1L}}\cosh(c_1(z_i + z_j - L) - \frac{1}{2}\ln\frac{\Gamma_0}{\Gamma_L}) + ...\right.$$

$$\left. 2\Gamma_0\Gamma_L e^{-2c_1L}\cosh(c_1(z_i - z_j)) + I_p \stackrel{\text{def}}{=} M(z_i, z_j)E(z_j) \quad (7.12)\right.$$

If the implant is composed of two different domains (e.g. the half insulated wire) the discussion in the theory and the elaboration above need to be extended. We will assume the wavenumber of the currents in the first domain is given by c_1 and the wavenumber in the second domain is given by c_2. Besides the reflection coefficients at $z = 0$ and $z = L$ (L again being the length of the implant), Γ_0 and Γ_L respectively, another reflection will occur at the interface between both domains at $z = h$ which is defined as Γ.

If the localized electric field is incident at $z_j < h$, i.e. on the first domain, it will generate an initial current wave given by,

$$I_p(z) = \sigma_{eff}AE(z_j)e^{-c_1|z_i - z_j|} \quad \forall z_j < h \wedge z_i < h. \quad (7.13)$$

The sum of all reflected waves in this same domain will have the familiar form,

$$I(z_i) = \frac{\sigma_{eff}AE(z_j)}{1 - \Gamma_0\Gamma_{h_{eff}^+}e^{-2c_1L}}\left(\sqrt{\Gamma_0\Gamma_{h_{eff}^+}e^{-2c_1L}}\cosh(c_1(z_i + z_j - L) - \frac{1}{2}\ln\frac{\Gamma_0}{\Gamma_{h_{eff}^+}}) + ...\right.$$

$$\left. \Gamma_0\Gamma_{h_{eff}^+}e^{-2c_1L}\cosh(c_1(z_i - z_j)) + I_p \quad (7.14)\right.$$

Note the similarities with equation 7.12. Now, however, L is replaced by h and Γ_L by $\Gamma_{h_{eff}^+}$, i.e. the effective reflection coefficient of the second domain for waves incident on the impedance interface from the first domain. This effective reflection coefficient is determined by the contributions of all the transmitted and reflected waves which itself again forms a geometric series that converges:

$$\Gamma_{h_{eff}^+} = \Gamma + \frac{(1 - \Gamma^2)e^{-2c_2(L-h)}}{1 + \Gamma\Gamma_L e^{-2c_2(L-h)}} \quad (7.15)$$

This same excitation will also induce a current in the second domain (so in case $z_j < h \wedge z_i > h$), where the wave number is c_2. The current in the first domain

will generate a wave at the boundary of magnitude $e^{-c_1 h}(e^{c_1 z_j} + \Gamma_0 e^{-c_1 z_j})/(1 - \Gamma_0 \Gamma e^{-2c_1 h})$ which in turn create a wave in the second domain given by,

$$I(z_i) = \frac{\sigma_{eff} A E(z_j)(1 - \Gamma)e^{-c_1 h}e^{c_2 h}(e^{-c_2 z_i} + \Gamma_L e^{-2c_2 L}e^{c_2 z_i})(e^{c_1 z_j} + \Gamma_0 e^{-c_1 z_j})}{1 - \Gamma_0 \Gamma e^{-2c_1 h} + \Gamma_L \Gamma e^{-2c_2(L-h)} + \Gamma_L \Gamma_0 e^{-2c_2(L-h)}e^{-2c_1 h}}$$

(7.16)

If the localized electric field is incident at $z_j > h$, i.e. on the second domain, we can deduce the induced currents most easily using the previous equation and symmetry considerations. If we interchange z with $L - z$, Γ with $-\Gamma$, Γ_0 with Γ_L, h with $L - h$ and c_1 with c_2 the resultant equations after substitution will describe the current distributions. With this substitution we define another effective reflection coefficient,

$$\Gamma_{h_{eff}^-} = \Gamma + \frac{(1 - \Gamma^2)e^{-2c_1 h}}{1 + \Gamma \Gamma_0 e^{-2c_1 h}}$$

(7.17)

The substitution leads to an equation that holds $\forall z_j > h \land z_i > h$,

$$I(z_i) = \sigma_{eff} A E(z_j) e^{c_2 |z_i - z_j|} + \frac{\sigma_{eff} A E(z_j)}{1 - \Gamma_0 \Gamma_{h_{eff}^-} e^{-2c_2(L-h)}} \Big(...$$

$$\sqrt{\Gamma_L \Gamma_{h_{eff}^-} e^{-2c_2(L-h)}} \cosh(c_2(z_i + z_j - h) - \frac{1}{2}\ln\frac{L}{\Gamma_{h_{eff}^-}}) + ...$$

$$\Gamma_L \Gamma_{h_{eff}^-} e^{-2c_2(L-h)} \cosh(c_2(z_i - z_j)) \Big) \quad (7.18)$$

and one that holds $\forall z_j > h \land z_i, h$,

$$I(z_i) = \frac{\sigma_{eff} A E(z_j)(1 - \Gamma)e^{-c_1 h}e^{c_2 h}(e^{c_1 z_i} + \Gamma_0 e^{-c_1 z_i})(e^{-c_2 z_j} + \Gamma_L e^{-2c_2 L}e^{c_2 z_j})}{1 - \Gamma_0 \Gamma e^{-2c_1 h} + \Gamma_L \Gamma e^{-2c_2(L-h)} + \Gamma_L \Gamma_0 e^{-2c_2(L-h)}e^{-2c_1 h}}$$

(7.19)

These four equations (i.e. **??**)describe the transfer matrix for a wire with an impedance transition composed of two electromagnetic domains. The same analysis can be used to derive the parameterized TM for more complex structures.

Appendix B: Details on the current determination method from the $|\mathbf{B}_1^+|$ distribution.

Firstly, the $|B_1^+|$ distribution in the phantom with an embedded wire has a high dynamic range, i.e. according to simulations and the corresponding experiments the maximum reached $|B_1^+|$ in the proximity of the wire can be over

an order of magnitude larger than the nominal $|B_1^+|$. This makes it hard to determine the $|B_1^+|$ distribution reliably for the entire actual flip angle range with normal $|B_1^+|$ mapping techniques. An alternative method was adopted based on the fitting the signal equation for multiple spoiled gradient echo acquisitions for various flip angles [45]

$$\mathcal{S}(\vec{r}) = \frac{C_1(\vec{r})(1 - e^{-TR/T_1})\sin(C_2(\vec{r})FA)}{1 - e^{-TR/T_1}\cos(C_2(\vec{r})FA)}e^{-TE/T_2^*}. \qquad (7.20)$$

The principle behind this method is shown in supporting figure S2. Depending on the extent of $|B_1^+|$ enhancement a different range of nominal flip angles is used for the fit with the signal equation. The same scan was acquired with a nominal FA of 0.25, 0.5, 1, 2, 3, 5, 7.5, 11, 15, 20, 30, 45, 70, 100 and 140 degrees. For low flip angles this dense sampling was necessary to get sufficient data points for fits in regions with strong field enhancement in the vicinity of the wire. Firstly, a fit (lsqcurvefit, MATLAB) was performed for increasing sets of flip angles ranging from [0.25:5] to [0.25: 140], i.e. the full set. A selection of the fit results and hence range of flip angles used for the fit was based on the first region of monotonically increasing and decreasing signal where equation S20 holds.

$$|B_1^+(r, \phi, z)| = \left(\frac{B_\phi(r, z)^2}{4} + B_{bc}(r, z)^2 - B_\phi(r, z)B_{bc}(r, z)\sin(\phi - \theta_0(r, z))\right)^{\frac{1}{2}} \qquad (7.21)$$

The fit result is considered as true $|B_1^+|$ distribution in the phantom with the wire present. From this distribution the current in the wire was determined. The superposition of the complex B_1^+ field around the current running in the wire and the complex B_1^+ field of the birdcage coil creates a distinct artifact. This artifact can be used to determine the magnitude of the current and the phase difference between both fields. The equation describing this artifact is,

where $B_\phi(r, z)$ is the B_1^+ field due to the wire, $B_{bc}(r, z)$ is the assumed to be constant B_1^+ field of the birdcage body coil (or any other transmission element) and $\theta_0(r, z)$ is the phase difference between both fields. This equation can be used to determine B_ϕ which is proportional to the current in the wire if we assume amperes circuital law is valid.

An example of a $|B_1^+(r, \phi, z)|$ as function of r and ϕ is shown in supporting figure S3. The modulation due to the wire field is clearly visible and also its inverse proportionality with respect to distance from the wire can be seen. The fit using equation 7.21 is also shown in this figure. This fit results in an estimate
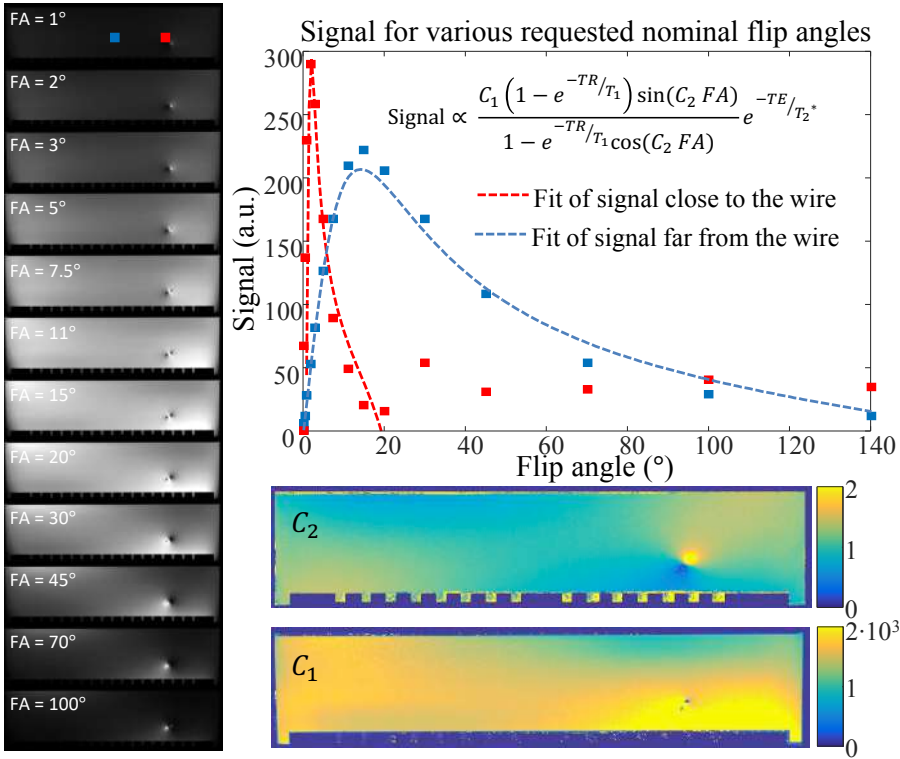
Figure 7.2: The principle behind the $|B_1^+|$ mapping techniques that is able to capture a high dynamic range of actual flip angles. The same scan is performed with various flip angles and the acquired signal as function of requested flip angles is fitted voxel wise with the signal equation for spoiled gradient echo acquisitions [117]. The example fit for a voxel close to the wire (red) and further away from the wire (blue) are shown. If this fit is performed voxel wise distributions for C_1 and C_2 appear which are shown below the example fit.
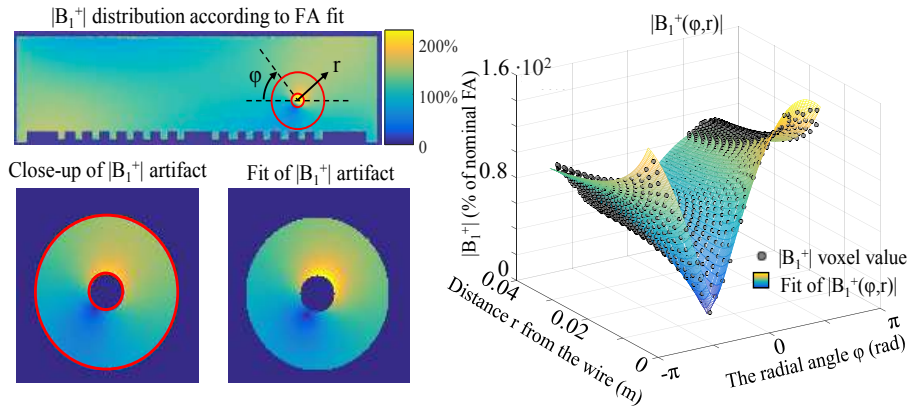
Figure 7.3: Supporting Figure S3. Current determination from the $|B_1^+|$ artifact around a wire. An annulus of $|B_1^+|$ data (from the multi-flip angle analysis) centered around the wire is fitted on a slice by slice bases with equation 7.21. The full $|B_1^+|$ distribution in the phantom is shown in the top left corner. A close-up of the selected annulus of $|B_1^+|$ data and its fit is shown in the bottom left corner. On the right this data and its fit is graphically shown as function of radial distance from the wire.

of the magnitude of the current in the wire and the phase difference between the background $|B_1^+|$ field, which is assumed to be constant, and the field created by the current in the wire. The quantities are used for determination of the transfer matrix.

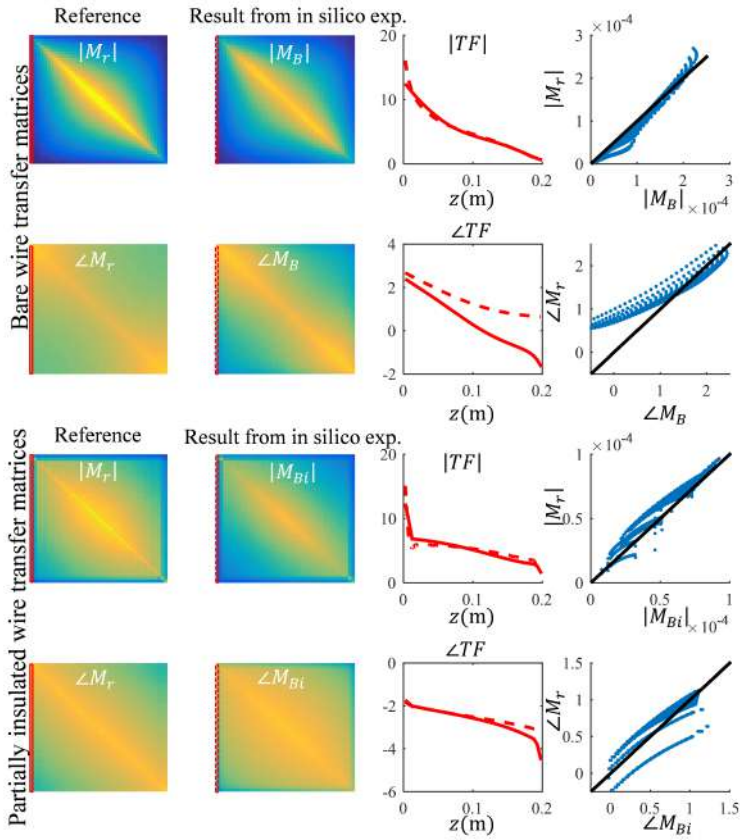# Appendix C:Supplementary figures for chapter 4

Figure 7.4: The TF and TM that follow from the fit of the simulated B_1^+ and tranceive phase distributions B and Bi shown in figures 4.3 and 4.4 respectively, corresponding to the straight wires under a 15 degrees angle with the z-axis.
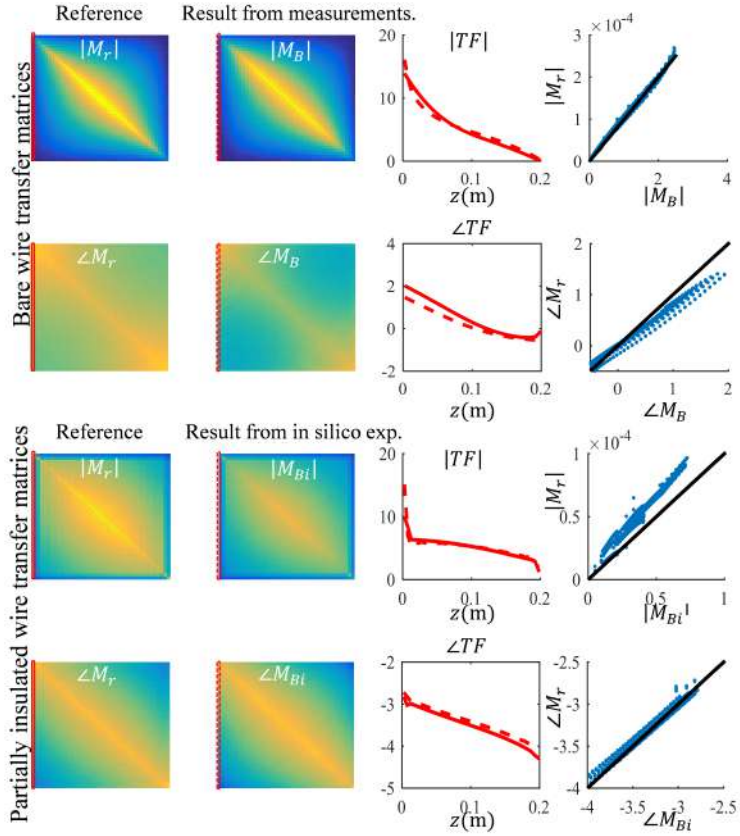
Figure 7.5: The TF and TM that follow from the fit of the measured B_1^+ and tranceive phase distributions B and Bi shown in figures 4.8 and 4.9 respectively, corresponding to the straight wires under a 15 degrees angle with the z-axis.
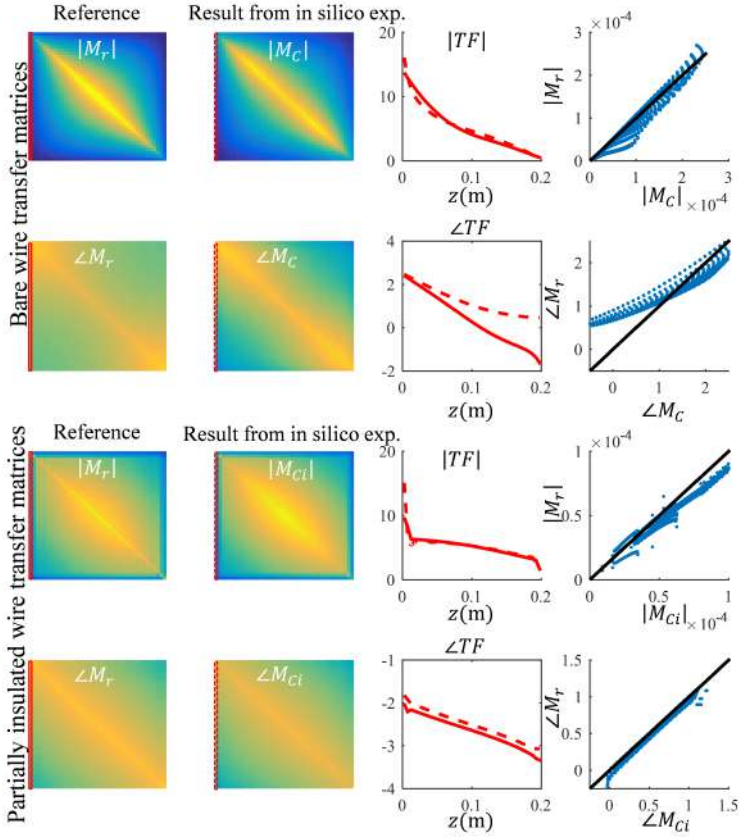
Figure 7.6: The TF and TM that follow from the fit of the simulated B_1^+ and tranceive phase distributions C and Ci shown in figures 4.3 and 4.4 respectively, corresponding to the straight wires under a 30 degrees angle with the z-axis.
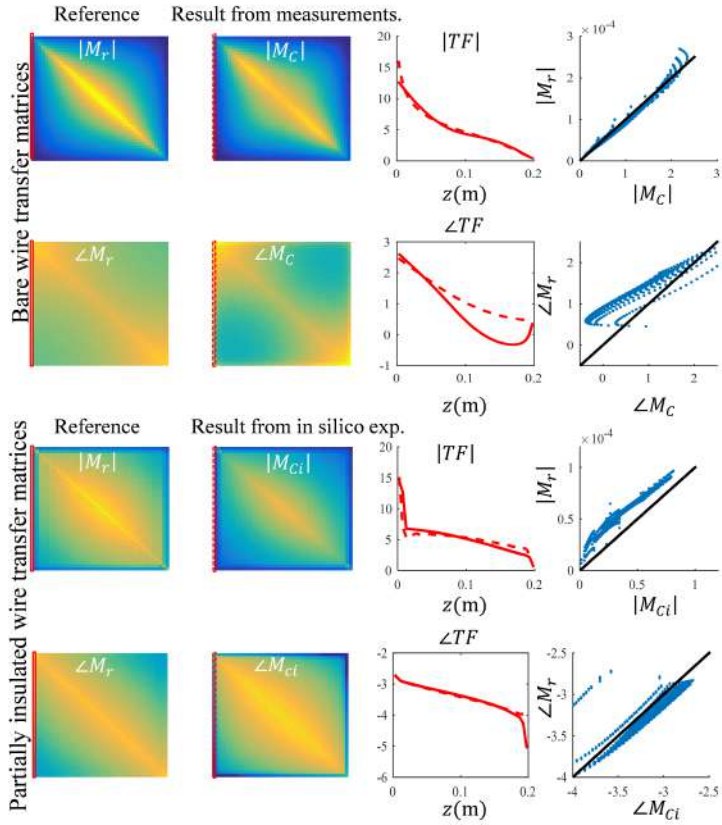
Figure 7.7: The TF and TM that follow from the fit of the measured B_1^+ and tranceive phase distributions C and Ci shown in figures 4.8 and 4.9 respectively, corresponding to the straight wires under a 30 degrees angle with the z-axis.
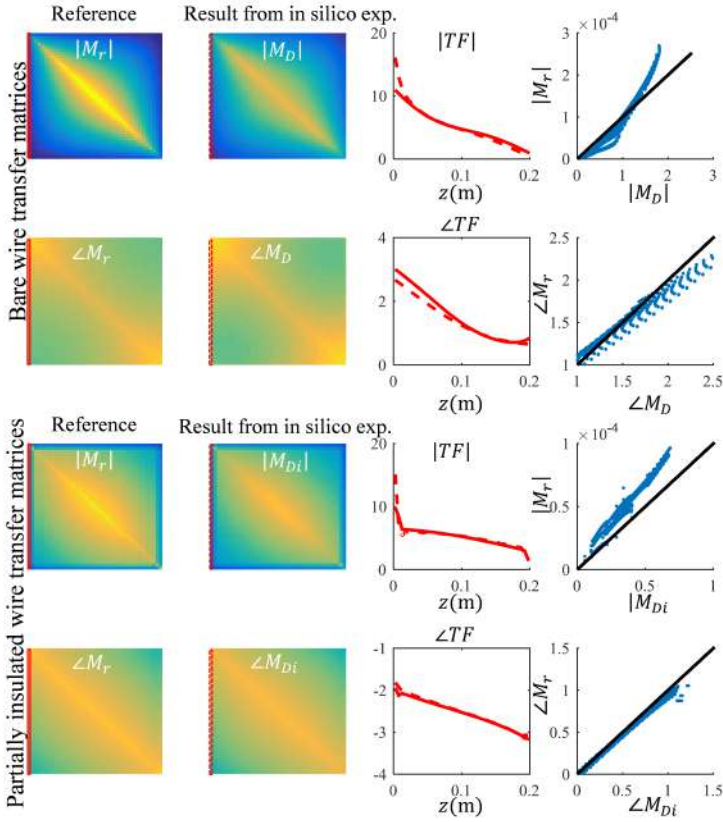
Figure 7.8: The TF and TM that follow from the fit of the simulated B_1^+ and tranceive phase distributions D and Di shown in figures 4.3 and 4.4 respectively, corresponding to the wires with a single bend.
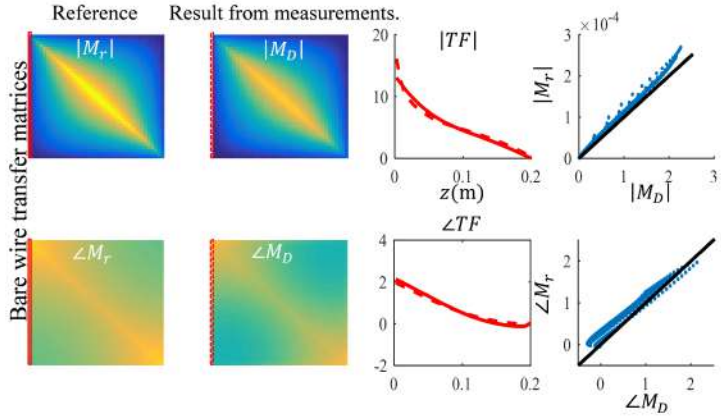
Figure 7.9: The TF and TM that follow from the fit of the measured B_1^+ and tranceive phase distributions D shown in figure 4.8,corresponding to the bare wire with a single bend.
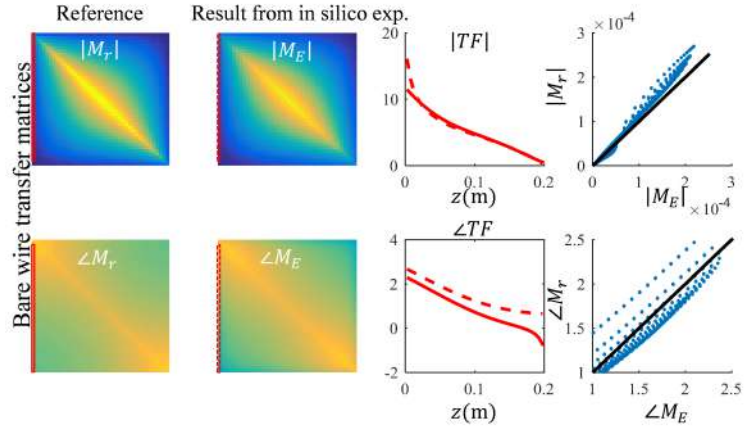

Figure 7.10: The TF and TM that follow from the fit of the measured B_1^+ and tranceive phase distribution E in figure 4.3, correspondingto the bare wire with a multiple bends.

Nederlandse Samenvatting

Voor veel ziektebeelden is MRI de meest geschikte beeldvormende modaliteit voor het stellen van diagnoses. De mogelijke toepassingen van MRI worden bovendien steeds uitgebreider. Naast anatomische informatie kan ook fysische, functionele, en metabole informatie met MRI worden verkregen. De kwaliteit van deze informatie is over de afgelopen jaren sterk toegenomen. Het is daarom niet verrassend dat het wereldwijd gebruik van MRI-scanners toeneemt. Een parallel aan deze trend is te zien in het wereldwijd gebruik van medische implantaten [1–3]. Dit is een logisch gevolg van het feit dat de leeftijdsverwachting blijft stijgen en mensen daarbij vaker ondersteund worden door implantaten waarvan de innovatie ook niet heeft stilgestaan.

Veel implantaten worden helaas beschouwd als een contra-indicatie voor MRI. Patiënten met dergelijke implantaten worden over het algemeen niet gescand tenzij de meerwaarde van de met MRI verkregen beelden opweegt tegen het extra risico waaraan de patiënt wordt blootgesteld. Er zijn verschillende interacties tussen de MRI scanner en implantaten die tot risico's voor de patiënt kunnen leiden.

Bij MRI worden drie (elektro)magnetische velden gebruikt om beelden te maken van de interne structuur en processen in het menselijk lichaam. In eerste instantie is er een sterk statisch magnetisch veld nodig om mensen in zeer geringe mate te magnetiseren. De interne magnetisatie zal gelijk of tegengesteld gericht zijn aan de richting van het externe veld gecreëerd door de MRI scanner. Het menselijke lichaam is niet bijzonder magnetisch en dus ondervinden we geen noemenswaardige aantrekkingskracht door deze magnetisatie. Vervolgens wordt de interne magnetisatie door een radiofrequent elektromagnetisch signaal weggeduwd van de richting van het externe veld. Hierna begint de magnetisatie te draaien terwijl deze langzaam (in verhouding tot de draaisnelheid) terugkeert naar dezelfde positie als voor het radiofrequente signaal. De draaisnelheid

is afhankelijk van de sterkte van het statische magnetische veld. Een extra magnetisch veld zorgt ervoor dat de draaisnelheid per positie verschillend is door een gradiënt aan te brengen bovenop het statische veld. Zo wordt het signaal met een locatie gecodeerd. Deze draaiende magnetisatie creëert een veld fluctuatie buiten de patiënt die kan worden opgevangen met zogenaamde ontvangstspoelen. Met behulp van een gereconstrueerde positie kan vervolgens een beeld worden gevormd.

Zowel het statische, het radiofrequente als het gradiënt magneetveld kunnen tot problemen leiden voor patiënten met implantaten. Het grootste en moeilijkst te vermijden risico voor implantaten met een actieve functie zoals pacemakers en deep brain stimulatoren schuilt in de interactie met het radiofrequente veld. Dit type implantaten bevat geleidende onderdelen om therapeutische stromen af te geven. Op deze geleidende onderdelen kan met name de elektrische component van radiofrequente veld een ongewilde stroom induceren waarbij het implantaat in feite als ontvangstantenne voor het radiofrequente veld functioneert. Deze ongewilde stromen zorgen vervolgens voor lokale opwarming die met name rond de electroden van de implantaten plaatsvindt, omdat de stroom in de geleidende draad bij deze contactpunten met het menselijke weefsel matig verder geleid wordt. Het karakteriseren van deze opwarming is van belang voor implantaat fabrikanten om te bepalen of en onder welke condities specifieke implantaten veilig zijn.

Tegenwoordig worden ontwerpen voorzien van een 'MR conditional label'. Dit label beschrijft operationele limieten voor de scanner waarbinnen veiligheid voor de patiënt gegarandeerd blijft. Het label is noodzakelijkerwijs conservatief omdat er van de meest ongunstige situatie moet worden uitgegaan. Technische specificatie ISO/TS 10974 beschrijft hoe de limieten in het label bepaald worden. Een karakteristiek van implantaten genaamd de transfer functie (TF) speelt een grote rol in de methodes die hierin beschreven staan. De TF vertaalt een invallend radiofrequent elektromagnetisch veld in de resulterende opwarming rond elektrodes op de uiteinden van de implantaten. Het kan worden beschouwd als een manier om het implantaat als ontvangst antenne te karakteriseren. Deze invalshoek ligt ten grondslag aan de methode die in hoofdstuk 2 beschreven staat. Omdat volgens het reciprociteitsprincipe de ontvangst en zend eigenschappen van antennes sterk aan elkaar gerelateerd zijn kwam het idee naar boven om een implantaat als antenne te gebruiken. Uit de MRI beelden die met deze 'antenne' worden verkregen kan vervolgens de TF worden bepaald.

De normale experimentele bepaling van de TF van implantaten gebeurt in toegewijde meetopstellingen in homogene fantomen die ontworpen zijn om relevante menselijke eigenschappen zo goed mogelijk te benaderen. De vertaling van de in fantomen bepaalde TF naar de in-vivo situatie introduceert onnauwkeurigheden omdat de antenne karakteristieken van een implantaat afhangen van de eigenschappen van zijn omgeving en mensen geen homogene zoutoplossingen zijn. De omvang van de effecten van een realistische omgeving op de TF van een implantaat zijn met behulp van een dergelijk experiment niet te bepalen. Daarom is het lastig om een inschatting van de geïntroduceerde onnauwkeurigheden te maken en worden conservatieve marges gebruikt. Met behulp van de methode geïntroduceerd in hoofdstuk 2 is het mogelijk hier een beter beeld van te krijgen. Deze op MRI gebaseerde techniek is namelijk in principe in heterogene vaste en vloeibare stoffen toepasbaar. Dit biedt mogelijkheden om de limieten in de MRI labels preciezer te formuleren. De effecten van een realistische omgeving op de TF kunnen worden gemeten waardoor niet langer van het ergst mogelijke scenario uit hoeft worden gegaan.

Toch zal een veiligheidsmarge nodig zijn omdat het pad dat het implantaat in het lichaam doorloopt per patiënt verschillend is. Daarmee zijn namelijk de eigenschappen van de omgeving waarin het implantaat zich bevindt per situatie anders en kan dus ook andere opwarming verwacht worden. Om veiligheid te garanderen moet van het ongunstigste (realistische) pad uit worden gegaan. In vivo TF bepaling zou de noodzaak van deze veiligheidsmarge wegnemen. Dit is fundamenteel onmogelijk met deze techniek omdat aanzienlijke aanpassing aan het implantaat nodig zijn om deze als een antenne te laten werken.

In hoofdstukken 3 en 4 staan methodes beschreven om de TF met MRI te bepalen zonder aanpassingen aan het implantaat. De gewone zendspoelen van de MRI scanner worden gebruikt in deze hoofdstukken om MRI beelden te krijgen van de implantaten. Deze spoelen generen een invallend veld op het implantaat dat vervolgens een stroom induceert. Een uitbreiding van de TF genaamd transfer matrix (TM) wordt in hoofdstuk 3 geïntroduceerd om het invallende veld en de geïnduceerde stroom aan elkaar te relateren. De TF is een onderdeel van de TM en derhalve bekend zodra de TM bepaald is. In hoofdstuk 3 wordt het invallende elektrische veld bepaald met simulaties en de geïnduceerde stroom gemeten uit de verstoring in het MRI beeld die deze stroom veroorzaakt. Zodra het invallende elektrische veld en de geïnduceerde stroom bekend zijn kan de TM en tegelijkertijd de TF bepaald worden. Het elektrisch veld kan alleen met simulaties bepaald worden als de exacte anatomie en de dielektrische eigenschappen van de geometrie in de scanner bekend zijn.

Omdat deze kennis niet altijd beschikbaar is, hebben we de methode in hoofd-stuk 4 uitgebreid met experimentele bepaling van het elektrische veld.

In hoofdstukken 3 en 4 worden analytisch modellen gebruikt om met MRI meetbare componenten van elektromagnetische velden rond een implantaat te beschrijven en te benaderen. Uit de beste benadering van de gemeten data met het model volgt de TF van het implantaat. Metingen in een fantoom worden door het model goed beschreven en leiden tot nauwkeurige bepaling van de TF. Hoe goed het model in staat is een werkelijke patiënt met een implantaat te beschrijven is een belangrijk vraagstuk op weg naar in-vivo TF bepaling. Ook zijn de methodes getest voor relatief simpele structuren. Realis-tische implantaten hebben vaak een gecompliceerder ontwerp. Het analytische model gebruikt om de TM te beschrijven zal moeten worden uitgebreid om gecompliceerdere implantaten te beschrijven. Ook de metingen om stromen en elektrische velden te bepalen kosten op het moment te veel tijd en vragen te veel vermogen van de MRI scanner om in hun huidige vorm toegepast te worden op patiënten met implantaten.

Als deze obstakels uit de weg geruimd worden en in-vivo TF bepaling op een veilige manier mogelijk wordt zouden patiënten met gelabelde implantaten sneller en/of beter kunnen worden gescand, omdat conservatieve marges kleiner kunnen worden gehouden. Nu moet voor alle factoren die van invloed zijn op de opwarming van een implantaat van het ergste geval worden uitgegaan. Dit is niet langer nodig met extra kennis van de TF in een specifieke positie in het lichaam. De zorg voor patiënten met implantaten met MR conditional labels zal hierdoor verbeteren.

De methodes beschreven in deze thesis zijn in principe direct toepas-baar op hogere veldsterkte. Vanwege de hoge kosten van de veiligheidsanalyse beschreven in ISO/TS 10974 wordt deze vaak alleen op 1.5T uitgevoerd omdat scanners met deze magnetische veldsterkte klinisch het meest gebruikt worden. Voor hogere veldsterktes wordt dan een contra-indicatie gegeven omdat de vei-ligheidsanalyse simpelweg niet is uitgevoerd. Er zijn echter fysische principes die de veiligheidsproblemen met betrekking tot het radiofrequente veld doen afnemen met toenemende veldsterkte. Het is daarom zeker geen gegeven dat een implantaat die een contra-indicatie vormt op 1.5T ook onveilig is op 3T en 7T. Met de beschreven methodes zou de opwarming rond implantaten ook op hogere veldsterktes kunnen worden ingeschat. De TM geeft een uitgebrei-dere beschrijving van de interacties van een implantaat met het radiofrequente elektromagnetische veld dan de TF. Dit wordt in hoofdstuk 5 gebruikt om

stroompatronen op implantaten op een inzichtelijke wijze te verklaren. De eigenvectoren van de TM beschrijven welke patronen op implantaten kunnen ontstaan. Deze kennis kan de methodes om stromen met MRI te meten die in eerdere hoofstukken beschreven staan en in de literatuur bekend zijn versnellen of robuuster maken.

MRI wordt vaak beschouwd als een risico voor patiënten met implantaten. Een van de meest notoire problemen is opwarming van electroden in contact met menselijk weefsel door het radiofrequente veld. Het is uitdagend gebleken een accurate inschatting te maken van de opwarming. Zoals in deze thesis staat beschreven kan juist een krachtige beeldvormende modaliteit als MRI een uitkomst bieden. Met MRI kan de interactie van een implantaat met het radiofrequente veld preciezer in kaart gebracht worden. Dit biedt mogelijkheden aan implantaat fabrikanten om hun producten beter te beschrijven en heeft de potentie de zorg voor een groeiende patiëntgroep te verbeteren.

References

[1] Bradshaw PJ, Stobie P, Knuiman MW, Briffa TG, Hobbs MS. Trends in the incidence and prevalence of cardiac pacemaker insertions in an ageing population. Open Heart 2014; 1:1–6.

[2] Bazaka K, Jacob MV. Implantable devices: Issues and challenges. Electronics 2013; 2:1–34.

[3] Stellbrink C, Trappe HJ. The follow-up of cardiac devices: what to expect for the future? European Heart Journal Supplements 2007; 9:I113–I115.

[4] Kalin R, Stanton MS. Current clinical issues for mri scanning of pacemaker and defibrillator patients. PACE - Pacing and Clinical Electrophysiology 2005; 28:326–328.

[5] Bernstein MA, King KF, Zhou XJ, "Handbook of MRI Pulse Sequences". ACADEMIC PR INC, 2004.

[6] Hanson LG. Introduction to magnetic resonance imaging techniques [teaching resource]. Drcmr 2009; .

[7] Brown RW, Cheng YCN, Haacke EM, Thompson MR, Venkatesan R, "Magnetic Resonance Imaging: Physical Principles and Sequence Design". John Wiley Sons, Inc., 2014.

[8] Schenck JF. Physical interactions of static magnetic fields with living tissues. Progress in Biophysics and Molecular Biology 2005; 87:185–204.

[9] Chaljub G, Kramer LA, Iii RFJ, Johnson RF, Singh H, Crow WN. Original report resulting from the presence of ferromagnetic nitrous oxide or oxygen tanks in the mr suite. AJR. American journal of roentgenology 2001; pp. 27–30.

[10] Spurgeon D. "flying" vacuum cleaners are among hazards in mri suites. British Medical Journal 2001; vol. 323:357.

[11] Chen DW. Boy, 6, dies of skull injury during mri; oxygen tank becomes fatal missile in hospital. ; pp. p B1, 5.

[12] Martin V, Drochon A, Fokapu O, Gerbeau JF. Magnetohemodynamics in the aorta and electrocardiograms. Physics in Medicine and Biology 2012; 57:3177–3195.

[13] Kinouchi Y, Yamaguchi H, Tenforde T. Theoretical analysis of magnetic field interactions with aortic blood flow. Bioelectromagnetics 1996; 17:21–32.

[14] Organization WH. Environmental health criteria 232 static fields. Static fields 2006; pp. 58–174.

[15] Vestibular effects of a 7 tesla mri examination compared to 1.5 t and 0 t in healthy volunteers. PLoS ONE 2014; 9:3–10.

[16] McJury M, a Blug, Joerger C, Condon B, Wyper D. Short communication: acoustic noise levels during magnetic resonance imaging scanning at 1.5 t. The British journal of radiology 1994; 67:413–5.

References

[17]   Foster JR, Hall DA, Summerfield AQ, Palmer AR, Bowtell RW. Sound-level measurements and calculations of safe noise dosage during epi at 3 t. Journal of Magnetic Resonance Imaging 2000; 12:157–163.

[18]   Radomskij P, Schmidt MA, Heron CW, Prasher D. Effect of mri noise on cochlear function pulmonary hypertension after ibuprofen prophylaxis in very preterm infants. Lancet 2002; 359:1485–1486.

[19]   Schaefer DJ, Bourland JD, Nyenhuis JA. Review of patient safety in time-varying gradient fields. Journal of Magnetic Resonance Imaging 2000; 12:20–29.

[20]   Limiting FOR, To E, Fields M. Icnirp guidelines for limiting exposure to time varying electric, magnetic and electromagnetic fields (up to 300ghz). Health Physics 1998; 74:494-522;.

[21]   Marshall J, Martin T, Downie J, Malisza K. A comprehensive analysis of mri research risks: In support of full disclosure. Canadian Journal of Neurological Sciences 2007; 34:11–17.

[22]   YeunHo J. Development of implantable medical devices : From an engineering perspective. International Neurourology Journal 2013; 17:98–106.

[23]   Zilberti L, Arduino A, Bottauscio O, Chiampi M. The underestimated role of gradient coils in mri safety. Magnetic Resonance in Medicine 2017; 77:13–15.

[24]   Bannan KE, Handler W, Chronik B, Salisbury SP. Heating of metallic rods induced by time-varying gradient fields in mri. Journal of Magnetic Resonance Imaging 2013; 38:411–416.

[25]   Nordbeck P, Fidler F, Weiss I, Warmuth M, Friedrich MT, Ehses P, Geistert W, Ritter O, Jakob PM, Ladd ME, Quick HH, Bauer WR. Spatial distribution of rf-induced e-fields and implant heating in mri. Magnetic Resonance in Medicine 2008; 60:312–319.

[26]   In vivo heating of pacemaker leads during magnetic resonance imaging. European Heart Journal 2005; 26:376–383.

[27]   Hazardous situation in the mr bore: induction in ecg leads causes fire. European radiology 2003; 13:690–694.

[28]   Permanent neurological deficit related to magnetic resonance imaging in a patient with implanted deep brain stimulation electrodes for parkinson's disease: case report. Neurosurgery 2005; 57:E1063; discussion E1063.

[29]   Rezai AR, Finelli D, Nyenhuis JA, Hrdlicka G, Tkach J, Sharan A, Rugieri P, Stypulkowski PH, Shellock FG. Neurostimulation systems for deep brain stimulation: In vitro evaluation of magnetic resonance imaging-related heating at 1.5 tesla. Journal of Magnetic Resonance Imaging 2002; 15:241–250.

[30]   Konings MK, Bartels LW, Smits HF, Bakker CJ. Heating around intravascular guidewires by resonating rf waves. Journal of Magnetic Resonance Imaging 2000; 12:79–85.

[31]   Martin ET, Coman JA, Shellock FG, Pulling CC, Fair R, Jenkins K. Magnetic resonance imaging and cardiac pacemaker safety at 1.5-tesla. Journal of the American College of Cardiology 2004; 43:1315–1324.

[32]   Nazarian S, Hansford R, Roguin A, Goldsher D, Zviman MM, Lardo AC, Caffo BS, Frick KD, Kraut MA, Kamel IR, Calkins H, Berger RD, Bluemke DA, Halperin HR. A prospective evaluation of a protocol for magnetic resonance imaging of patients with implanted cardiac devices. Annals of Internal Medicine 2011; 155:415–424.

[33]   Gray RW, Bibens WT, Shellock FG. Simple design changes to wires to substantially reduce mri-induced heating at 1.5 t: implications for implanted leads. Magnetic Resonance Imaging 2005; 23:887 – 891.

[34]   Bottomley PA, Kumar A, Edelstein WA, Allen JM, Karmarkar PV. Designing passive mri-safe implantable conducting leads with electrodes. Medical Physics 2010; 37:3828–3843.

[35]   Kozlov M, Kainz W. Sensitivity of the transfer function of a helix lead on the dielectric properties of the surrounding media: A case study. 2017 IEEE International Conference on Microwaves, Antennas, Communications and Electronic Systems, COMCAS 2017 2018; 2017-Novem:1–6.

134

[36] Baker KB, Tkach J, Hall JD, Nyenhuis JA, Shellock FG, Rezai AR. Reduction of magnetic resonance imaging-related heating in deep brain stimulation leads using a lead management device. Neurosurgery 2005; 57:392–397.

[37] Measuring rf-induced currents inside implants: Impact of device configuration on mri safety of cardiac pacemaker leads. Magnetic Resonance in Medicine 2009; 61:570–578.

[38] Sommer T, Vahlhaus C, Lauck G, a von Smekal, Reinke M, Hofer U, Block W, Träber F, Schneider C, Gieseke J, Jung W, Schild H. Mr imaging and cardiac pacemakers: in-vitro evaluation and in-vivo studies in 51 patients at 0.5 t. Radiology 2000; 215:869–879.

[39] Complexity of mri induced heating on metallic leads: Experimental measurements of 374 configurations. BioMedical Engineering Online 2008; 7:1–16.

[40] Comparison of three multichannel transmit/receive radiofrequency coil configurations for anatomic and functional cardiac mri at 7.0t: Implications for clinical imaging. European Radiology 2012; 22:2211–2220.

[41] Calculation of mri-induced heating of an implanted medical lead wire with an electric field transfer function. Journal of Magnetic Resonance Imaging 2007; 26:1278–1285.

[42] Zastrow E, Capstick M, Cabot E, Kuster N. Piece-wise excitation system for the characterization of local {RF}-induced heating of {AIMD} during {MR} exposure. Proceeding of the International Symposium on Electromagnetic Compatibility, Tokyo 2014; pp. 241–244.

[43] Missoffe A, Aissani S. Experimental setup for transfer function measurement to assess rf heating of medical leads in mri: Validation in the case of a single wire. Magnetic Resonance in Medicine 2017; 00:1–7.

[44] Griffin GH, Ramanan V, Barry J, Wright GA. Toward in vivo quantification of induced rf currents on long thin conductors. Magnetic Resonance in Medicine 2018; .

[45] van den Bosch MR, Moerland MA, Lagendijk JJW, Bartels LW, van den Berg CAT. New method to monitor rf safety in mri-guided interventions based on rf induced image artefacts. Medical Physics 2010; 37:814–821.

[46] Stellbrink C, Trappe HJ. The follow-up of cardiac devices: what to expect for the future? European Heart Journal Supplements 2007; 9:I113–I115.

[47] Feng S, Qiang R, Kainz W, Chen J. A technique to evaluate mri-induced electric fields at the ends of practical implanted lead. IEEE Transactions on Microwave Theory and Techniques 2015; 63:305–313.

[48] Nyenhuis JA, Park SM, Kamondetdacha R, Amjad A, Shellock FG, Rezai AR. Mri and implanted medical devices: basic interactions with an emphasis on heating. IEEE Transactions on Device and Materials Reliability 2005; 5:467–480.

[49] Kainz W, Neubauer G, Überbacher R, Alesch F, Chan DD. Temperature measurement on neurological pulse generators during mr scans. BioMedical Engineering OnLine 2002; 1:2.

[50] Overall WR, Pauly JM, Stang PP, Scott GC. Ensuring safety of implanted devices under mri using reversed rf polarization. Magnetic Resonance in Medicine 2010; 64:823–833.

[51] Eryaman Y, Akin B, Atalar E. Reduction of implant rf heating through modification of transmit coil electric field. Magnetic Resonance in Medicine 2011; 65:1305–1313.

[52] EtezadiAmoli M, Stang P, Kerr A, Pauly J, Scott G. Controlling radiofrequency-induced currents in guidewires using parallel transmit. Magnetic Resonance in Medicine 2015; 74:1790–1802.

[53] implants ISA. Iso/ts 10974:2012(en). assessment of the safety of magnetic resonance imaging for patients with an active implantable medical device. 2012; .

[54] Park SM, Kamondetdacha R, Nyenhuis JA. Calculation of mri-induced heating of an implanted medical lead wire with an electric field transfer function. Journal of Magnetic Resonance Imaging 2007; 26:1278–1285.

References

[55] Venook R, Overall W, Shultz K, Conolly S, Pauly J, Scott G. Monitoring induced currents on long conductive structures during mri. In: Proceedings 16th Scientific Meeting, International Society for Magnetic Resonance in Medicine, In: Proceedings 16th Scientific Meeting, International Society for Magnetic Resonance in Medicine, 2008. p. 898.

[56] Nordbeck P, Weiss I, Ehses P, Ritter O, Warmuth M, Fidler F, Herold V, Jakob PM, Ladd ME, Quick HH, Bauer WR. Measuring rf-induced currents inside implants: Impact of device configuration on mri safety of cardiac pacemaker leads. Magnetic Resonance in Medicine 2009; 61:570–578.

[57] Griffin GH, Anderson KJ, Celik H, Wright GA. Safely assessing radiofrequency heating potential of conductive devices using image-based current measurements. Magnetic Resonance in Medicine 2015; 73:427–441.

[58] Hoult DI. The principle of reciprocity in signal strength calculations—a mathematical guide. Concepts in Magnetic Resonance 2000; 12:173–187.

[59] Feng S, Qiang R, Kainz W, Chen J. A technique to evaluate mri-induced electric fields at the ends of practical implanted lead. IEEE Transactions on Microwve Theory and Techniques 2015; 63:305–313.

[60] Kozlov M, Schaefers G. Numerical analysis of time - varied radio frequency induced heating on and near an implant during magnetic resonance imaging. IEEE International Conference on Microwaves, Communications, Antennas and Electronic Systems (COMCAS 2015), November 2015, Tel Aviv, Israel 2015; l:2–4.

[61] F218211a A. Standard test method for measurement of radio frequency induced heating on or near passive implants during magnetic resonance imaging. ; .

[62] van Lier AL, Brunner DO, Pruessmann KP, Klomp DW, Luijten PR, Lagendijk JJ, van den Berg CA. B phase mapping at 7 t and its application for in vivo electrical conductivity mapping. Magnetic Resonance in Medicine 2012; 67:552–561.

[63] Yeung CJ, Susil RC, Atalar E. Rf heating due to conductive wires during mri depends on the phase distribution of the transmit field. Magnetic Resonance in Medicine 2002; 48:1096–1098.

[64] Yeung CJ, Susil RC, Atalar E. Rf safety of wires in interventional mri: Using a safety index. ; 47:187–193.

[65] Langman DA, Goldberg IB, Judy J, Finn JP, Ennis DB. The dependence of radiofrequency induced pacemaker lead tip heating on the electrical conductivity of the medium at the lead tip. Magnetic Resonance in Medicine 2012; 68:606–613.

[66] Tokaya JP, Raaijmakers AJE, Luijten PR, Bakker JF, van den Berg CAT. Mri-based transfer function determination for the assessment of implant safety. Magnetic Resonance in Medicine 2017; 00.

[67] Yeh P, "Optical Waves in Layered Media". 1988.

[68] Arfken GB, Weber HJ, Harris FE, "Mathematical Methods for Physicists". 2013.

[69] Katscher U, van den Berg CA. Electric properties tomography: Biochemical, physical and technical background, evaluation and clinical applications. NMR in Biomedicine 2017; 30:1–15.

[70] F2182-11a. A. standard test method for measurement of radio frequency induced heating on or near passive implants during magnetic resonance imaging. Book of Standards Volume: 13.01 2014; .

[71] Griffin GH, Anderson KJ, Celik H, a. Wright G. Safely assessing radiofrequency heating potential of conductive devices using image-based current measurements. Magnetic Resonance in Medicine 2015; 73:427–441.

[72] Overall WR, Pauly JM, Stang PP, Scott GC. Ensuring safety of implanted devices under mri using reversed rf polarization. Magnetic Resonance in Medicine 2010; 64:823–833.

[73] Yarnykh VL. Actual flip-angle imaging in the pulsed steady state: A method for rapid three-dimensional mapping of the transmitted radiofrequency field. Magnetic Resonance in Medicine 2007; 57:192–200.

[74] Klassen LM, Menon RS. Robust automated shimming technique using arbitrary mapping acquisition parameters (rastamap). Magnetic Resonance in Medicine 2004; 51:881–887.

[75] Barker GJ, Simmons A, Arridge SR, Tofts PS. A simple method for investigating the effects of non-uniformity of radiofrequency transmission and radiofrequency reception in mri. British Journal of Radiology 1998; 71:59–67.

[76] Alecci M, Collins CM, Smith MB, Jezzard P. Radio frequency magnetic field mapping of a 3 tesla birdcage coil: experimental and theoretical... - abstract - uk pubmed central. Magnetic Resonance in Medicine 2001; 46:379–385.

[77] in den Kleef JJE, Cuppen JJM. Rlsq: T1, t2, and ?? calculations, combining ratios and least squares. Magnetic Resonance in Medicine 1987; 5:513–524.

[78] Wen H. Noninvasive quantitative mapping of conductivity and dielectric distributions using rf wave propagation effects in high-field mri. Proc. SPIE 5030, Medical Imaging: Physics of Medical Imaging 2003; 5030:471–477.

[79] Gupte AA, Shrivastava D, Spaniol MA, Abosch A. Mri-related heating near deep brain stimulation electrodes: More data are needed. Stereotactic and Functional Neurosurgery 2011; 89:131–140.

[80] Shen LC, Wu TT, King RWP. A simple formula of current in dipole antennas. IEEE Transactions on Antennas and Propagation 1968; AP-16:542–547.

[81] King RW, Trembly BS, Strohbehn JW. The electromagnetic field of an insulated antenna in a conducting or dielectric medium. IEEE Transactions on Microwave Theory and Techniques 1983; 31:574–583.

[82] Acikel V, Atalar E. Modeling of radio-frequency induced currents on lead wires during mr imaging using a modified transmission line method. Medical Physics 2011; 38:6623–6632.

[83] Hargreaves BA, Worters PW, Pauly KB, Pauly JM, Koch KM, Gold GE. Metal-induced artifacts in mri. American Journal of Roentgenology 2011; 197:547–555.

[84] Sacolick LI, Wiesinger F, Hancu I, Vogel MW. B1 mapping by bloch-siegert shift. Magnetic Resonance in Medicine 2010; 63:1315–1322.

[85] Nehrke K, Versluis MJ, Webb A, Börnert P. Volumetric b1+ mapping of the brain at 7t using dream. Magnetic Resonance in Medicine 2014; 71:246–256.

[86] Iterative separation of transmit and receive phase contributions and b 1 + -based estimation of the specific absorption rate for transmit arrays. Magnetic Resonance Materials in Physics, Biology and Medicine 2013; 26:463–476.

[87] Sbrizzi A, Hoogduin H, Lagendijk JJ, Luijten P, Berg CATVD. Robust reconstruction of b1+ maps by projection into a spherical functions space. Magnetic Resonance in Medicine 2014; 71:394–401.

[88] Katscher U, Findeklee C, Voigt T. B1-based specific energy absorption rate determination for nonquadrature radiofrequency excitation. Magnetic Resonance in Medicine 2012; 68:1911–1918.

[89] Eryaman Y, Turk EA, Oto C, Algin O, Atalar E. Reduction of the radiofrequency heating of metallic devices using a dual-drive birdcage coil. Magnetic Resonance in Medicine 2013; 69:845–852.

[90] McElcheran CE, Yang B, Anderson KJ, GolenstaniRad L, Graham SJ. Investigation of parallel radiofrequency transmission for the reduction of heating in long conductive leads in 3 tesla magnetic resonance imaging. PLoS ONE 2015; 10:1–21.

References

[91] Golestanirad L, Keil B, Angelone LM, Bonmassar G, Mareyam A, Wald LL. Feasibility of using linearly polarized rotating birdcage transmitters and close-fitting receive arrays in mri to reduce sar in the vicinity of deep brain simulation implants. Magnetic Resonance in Medicine 2017; 77:1701–1712.

[92] Tokaya JP, Raaijmakers AJ, Luijten PR, van den Berg CA, Tokaya CPJ. Mri-based, wireless determination of the transfer function of a linear implant: Introduction of the transfer matrix. 2018; pp. 1–14.

[93] Glover G, Hayes C, Pelc N, Edelstein W, Mueller O, Hart H, Hardy C, O'Donnell M, Barber W. Comparison of linear and circular polarization for magnetic resonance imaging. Journal of Magnetic Resonance 1985; 64:255–270.

[94] van Lier ALHMW, Raaijmakers A, Voigt T, Lagendijk JJW, Luijten PR, Katscher U, van den Berg CAT. Electrical properties tomography in the human brain at 1.5, 3, and 7t: A comparison study. Magnetic Resonance in Medicine 2014; 71:354–363.

[95] Jefimenko OD. Solutions of maxwell's equations for electric and magnetic fields in arbitrary media. American Journal of Physics 2005; 60:899–902.

[96] Jefimenko OD, "Electricity and magnetism an Introduction". Electret Scientific; 2nd edition, 1989.

[97] J.C.Lagarias, J.A.Reeds MHWPW. Convergence properties of the nelder–mead simplex method in low dimensions. Society for Industrial and Applied Mathematics 1998; 07932:112–147.

[98] Wright PE. No title. 1998; 07932.

[99] BioucasDias JM, Valadão G. Phase unwrapping via graph cuts. IEEE Trans. Image Process. 2007; 16:698–709.

[100] Kolmogorov V, Zabih R. What energy functions can be minimized via grph cuts? IEEE Trans. on Pattern Analysis and Machine Intelligence 2004; 26:147–159.

[101] Monu U, Worters P, Sung K, Koch K, Gold G, Hargreaves B. B1 mapping near metallic implants. In Proceedings of the 19th Annual Meeting of the ISMRM 2011; p. 317.

[102] Kraus JD, Marhefka RJ. Antennas for all applications.pdf, 1988.

[103] Scott G, EtezadiAmoli M, Stang P, Nan H, Aliroteh M, Pauly J. Thermo-acoustic ultrasound detection of rf coil and tip sar. ISMRM Proceedings 2015; 23:2015.

[104] Dimbylow PJ. Fdtd calculations of the whole-body averaged sar in an anatomically realistic voxel model of the human body from 1 mhz to 1 ghz. Physics in Medicine and Biology 1997; 42:479–490.

[105] Córcoles J, Zastrow E, Kuster N. Convex optimization of mri exposure for mitigation of rf-heating from active medical implants. Physics in Medicine and Biology 2015; 60:7293–7308.

[106] Murbach M, Neufeld E, Kainz W, Pruessmann KP, Kuster N. Whole-body and local rf absorption in human models as a function of anatomy and position within 1.5t mr body coil. Magnetic Resonance in Medicine 2014; 71:839–845.

[107] Christ A, Kainz W, Hahn EG, Honegger K, Zefferer M, Neufeld E, Rascher W, Janka R, Bautz W, Chen J, Kiefer B, Schmitt P, Hollenbach HP, Shen J, Oberle M, Szczerba D, Kam A, Guag JW, Kuster N. The virtual family - development of surface-based anatomical models of two adults and two children for dosimetric simulations. Physics in Medicine and Biology 2010; 55.

[108] Huang Y, Boyle K, "ANTENNAS". 2018.

[109] Yeung CJ, Susil RC, Atalar E. Rf safety of wires in interventional mri: Using a safety index. Magnetic Resonance in Medicine 2002; 47:187–193.

[110] a. Nyenhuis J, Park SM, Kamondetdacha R, Amjad A, Shellock FG, Rezai AR. Mri and implanted medical devices: Basic interactions with an emphasis on heating. IEEE Transactions on Device and Materials Reliability 2005; 5:467–479.

138

[111] Kozlov M, Schaefers G. Influence of electrical properties of lead insulation on radio frequency induced heating during mri. ISMRM Proceedings 2016; .

[112] Kozlov M, Schaefers G. Influence of the second surrounding tissue on radio frequency induced power deposition. 2016; pp. 1635–1636.

[113] Chen XL, Feng S, Xin X, Huang X, Jiang R, Sison S. Implantable lead mri rf heating in-vivo transfer function modeling to determine suitable test medium. ISMRM Proceedings 2018; .

[114] Eryaman Y, Akin B, Atalar E. Reduction of implant rf heating through modification of transmit coil electric field. Magnetic Resonance in Medicine 2011; 65:1305–1313.

[115] Eryaman Y, Guerin B, Akgun C, Herraiz JL, Martin A, TorradoCarvajal A, Malpica N, HernandezTamames JA, Schiavi E, Adalsteinsson E, Wald LL. Parallel transmit pulse design for patients with deep brain stimulation implants. Magnetic Resonance in Medicine 2015; 73:1896–1903.

[116] Meliado E, Raaijmakers A, Sbrizzi A, Steensma B, Maspero M, Savenije M, Luijten PR, van den Berg C. A deep learning method for image-based subject specific local sar assessment. MRM 2019; .

[117] W.A.Ernst, R.R. A. Application of fourier transform spectroscopy to magnetic resonance. Review of Scientific Instruments 1966; 37:93–102.

List of publications

Scientific Papers

1. MRI-based transfer function determination for the assessment of implant safety.
   Janot P. Tokaya, Alexander J.E. Raaijmakers, Peter R. Luijten, Jurriaan F Bakker and Cornelis A.T. van den Berg, Magn Reson Med 2017,78(6):2449-2459. doi: 10.1002/mrm.26613.

2. MRI-based, wireless determination of the transfer function of a linear implant: Introduction of the transfer matrix.
   Janot P. Tokaya, Alexander J.E. Raaijmakers, Peter R. Luijten, and Cornelis A.T. van den Berg, Magn Reson Med. 2018 Dec;80(6):2771-2784. doi: 10.1002/mrm.27218.

3. MRI-based transfer function determination through the transfer matrix by jointly fitting the incident and scattered B_1^+ field.
   Janot P. Tokaya Alexander J.E. Raaijmakers Peter R. Luijten Alessandro Sbrizzi Cornelis A.T. van den Berg, Magn Reson Med. 2019, 00:1–15. doi: 10.1002/mrm.

4. Explaining current patterns on implantable medical devices during MRI using the transfer matrix.
   Janot P. Tokaya, Peter R.S. Stijnman, Peter R. Luijten, Cornelis A.T. van den Berg and Alexander J.E. Raaijmakers, Conditionally accepted for publication in Medical Physics.

5. Accelerating implant RF safety assessment using a low-rank inverse update method.
   Peter R.S. Stijnman, Janot P. Tokaya, Jeroen van Gemert, Peter R. Luijten, Josien P.W. Pluim, Wyger M. Brink, Rob F. Remis, Cornelis A.T. van den Berg, Alexander J.E. Raaijmakers. Magn Reson Med. 2019,doi: 10.1002/mrm.28023, Epub ahead of print

Conference proceedings

1. Depth dependent safety analysis of peripheral arterial stents at 7 tesla.
   Janot P. Tokaya, Alexander J.E. Raaijmakers, Anja van der Kolk, Jurriaan F. Bakker, Peter R. Luijten, Dennis Klomp and Cornelis A.T. van den Berg, ISMRM Benelux 2015

2. Ultra-fast MRI based transfer function determination for the assessment of implant safety.
   Janot P. Tokaya, Alexander J.E. Raaijmakers, Peter R. Luijten and Cornelis A.T. van den Berg, ISMRM and ISMRM Benelux 2016 (Acknowledged with a summa cum laude merit award and best presenter award

3. MRI based RF safety characterization of implants using the implant response matrix: a simulation study.
   Janot P. Tokaya, Alexander J.E. Raaijmakers, Peter R. Luijten and Cornelis A.T. van den Berg, ISMRM and ISMRM Benelux 2017

4. MR based transfer matrix determination for a linear implant by joint estimation of the incident and scattered B_1^+ fields
   Janot P. Tokaya, Alexander J.E. Raaijmakers, Alessandro Sbrizzi, Peter R. Luijten and Cornelis A.T. van den Berg, ISMRM Benelux 2018

5. Explaining current patterns on linear metallic implants during MRI exams using the transfer matrix.
   Janot P. Tokaya, Peter Stijnman, Peter R. Luijten, Cornelis A.T. van den Berg and Alexander J.E. Raaijmakers, ISMRM 2019 (Acknowledged with a magna cum laude merit award)

Curriculum vitae

Nederlands

Janot Philippe Tokaya werd op 9 augustus 1989 in Groningen geboren en is in Stedum opgegroeid. Na als beste bèta van het jaar 2007 aan het Praedinius Gymnasium zijn middelbare schoolopleiding te hebben afgerond begon hij aan natuurkunde aan de Rijksuniversiteit Groningen. Vervolgens ontving hij, na het behalen van zijn bachelor in natuurkunde en wiskunde, de master theoretische natuurkunde met de distinctie 'cum laude' in 2013. Zijn masteronderzoek, onder begeleiding van prof. dr. M.V. (Maxim) Mostovoy, ging over de detectie van de magnetische skyrmion toestand in helimagneten.

In 2014 begon hij met het promotieonderzoek naar de veiligheid van implantaten in MRI scanners aan het Universitair Medisch Centrum Utrecht in samenwerking met Sapiens Steering Brain Stimulation. De belangrijkste bevindingen van dit onderzoek staan in dit proefschrift beschreven.

English

Janot Philippe Tokaya was born on the 9th of august 1989 in Groningen. After graduating high school as the best beta student of the class of 2007 at the Praedinius Gymnasium he started studying physics at the Rijksuniversiteit Groningen. Here, he received a masters degree in theoretical physics with a cum laude distinction in 2013, after finishing a bachelor in physics and mathematics. In his master thesis the detection of the skyrmion state in helimagnets was researched under the supervision of prof. dr. M.V. (Maxim) Mostovoy.

In 2014 he started as a Ph.D. candidate at the University Medical Centre Utrecht in collaboration with Sapiens Steering Brain Stimulation researching the safety of implants in MRI scanners. The most important research findings are presented in this thesis.

Dankwoord

Dit proefschrift is tot stand gekomen dankzij bijdrages van veel mensen en zonder deze steun had de inhoud nooit de vorm gekregen die het nu heeft. Mijn dank voor alle inbreng, op wat voor manier dan ook, is groot. Als ik mensen individueel ga bedanken zal ik daar ongetwijfeld sommigen bij vergeten, maar toch voel ik de noodzaak om een aantal mensen persoonlijk te noemen.

In eerste instantie wil ik mijn copromotoren dr. ir. C.A.T. van den Berg en dr. ir. A.J.E. Raaijmakers bedanken. Beste Nico en Alexander, Jullie inbreng over de afgelopen jaren is enorm geweest. Jullie vullen elkaar met jullie verschillende aanpak en perspectief geweldig aan. Nico, je creatieve manier van denken en je kennis van wat er door verschillende onderzoeksgroepen over de wereld wordt gedaan zorgt ervoor dat je altijd met originele vondsten komt. Vaak had ik na een gesprek met jou weer nieuwe energie en allerlei nieuwe ideeën om uit te proberen. Alexander, je praktische inzicht en resultaatgerichtheid waren daarna vaak noodzakelijk om weer richting aan het onderzoek te geven. Ik kan me nog goed herinneren hoe enthousiast we werden toen we tijdens een avond scannen voor het eerst een implant, die we naar aanleiding van een ingeving van jou als antenne gebruikten, in de MRI-beelden zagen oplichten. Verder heb je me vaak gestimuleerd om bevindingen op papier te zetten en vervolgens veel tijd besteed om mijn teksten van feedback te voorzien. Vaak kon ik deze stimulans goed gebruiken.

Daarnaast wil ik mijn promotor, prof. dr. Peter Luijten, bedanken. De door jou aangestuurde 7T MRI groep is een inspirerende en gezellige omgeving met een mooie balans tussen expertise, gedrevenheid en plezier. Toen mijn eerste poging om iets te publiceren in het water was gevallen, omdat een onderzoeksgroep uit Berlijn ons net voor was met het naar buiten brengen van vergelijkbare bevindingen heb je mij een hart onder de riem gestoken. Jou was tijdens je eigen promotieonderzoek iets soortgelijks overkomen, maar dat dit

145

kon ook positief worden uitgelegd. De resultaten waren immers al bevestigd en er was bovendien interesse in het onderwerp.

Beste leden van de beoordelingscommissie, prof. dr. D.W.J. Klomp, prof. dr.ir. J.W. Lagendijk, prof. dr. T. Leiner, dr. A.G van der Kolk, hartelijk bedankt voor het lezen en beoordelen van het proefschrift en jullie aanwezigheid bij de promotieplechtigheid. Dear Prof. Dr. Ing. Andreas Bitz thank you very much for your time, reading and assessing the thesis and for coming to Utrecht for the defense.

Ik wil al mijn lieve collega's van Q2 bedanken voor de plezierige werkomgeving. Als je hier over de gang loopt staan de deuren open voor advies, een kopje koffie of een gezellig praatje. Toen ik net begon bij het UMC Utrecht duurde het niet lang voordat ik me welkom voelde op de afdeling. In een kamer met Tijl, Vincent, Woko en later Arrie kon ik me snel bekend maken met alle facetten van MRI. Geen MRI gerelateerd raadsel bleef in een kantoor met dergelijke connaisseurs onbeantwoord.

Arrie, Arjan, of onderhand dr. Hendriks, ik ben blij dat wij, toen onze afdeling twee verdiepingen omlaag verhuisde, wederom bij elkaar op de kamer beland zijn. Ik ken weinig mensen die zo eerlijk en behulpzaam zijn als jij. Je hebt me veel geholpen en het was voor mij dan ook een grote eer om je tijdens je eigen verdediging te mogen flankeren. Met onze nieuw kamergenoten, Tim en Frank, hadden we het ook goed getroffen. Met zijn 4en vormden we, Q02.4.312, de gezelligste kamer van Q2. Frank, Quickfox, bedankt voor de thermometrie tips en dat je me bekend hebt gemaakt met de AIVD-kerstpuzzel. Tim, dankzij jou voetbal ik bij de Geuken, snap ik iets van de scanner software en weet ik dat je Pröpper altijd moet opstellen. Daarnaast begonnen de ochtenden altijd goed met een kop morning delight. Het was goed om naast je te zitten op het werk, naast je te staan tijdens je promotie en je met Charlotte in het huwelijksbootje te zien stappen. Bedankt voor deze mooie momenten. Toen Oscar erbij kwam om Frank te vervangen werd de humus traditie in ere hersteld. Ondanks je tips lukt het me nog steeds niet je cappuccino te evenaren.

I'd also like to thank my new roommates. You made leaving Q02.4.312 more pleasant. Ria, thanks for making my dal bhat more digestible. Zahra, thanks for the exotic sweets and Lieke for putting up with all my papers spilling over onto your desk. Peter, ik vond het echt fijn dat jij ook op het implantaat project bent begonnen en dat we de afgelopen tijd samen hebben kunnen werken. Gelukkig blijven we elkaar op het voetbalveld en de spelletjes avonden nog wel tegen komen.

Super Superweirdos, Lisa, Arjen, Erwin, Tijl, Cata, Deji, Mario, Wouter en Alex de vele mooie avonden met etentjes pubquizzen, films en andere gezelligheid hebben mijn leven als promovendus zo veel leuker gemaakt. Bedankt hiervoor. Lisa, Arjen en Erwin wil ik daarnaast bedanken voor de weekendjes weg, het gezamenlijk sporten en de lunchwandelingen. Sander wil ik bedanken voor de fanatieke lunchwandelingen. Cyril, thanks for showing Arrie, Deji and me all good things Marseille has to offer and for discussing some none sciency stuff every now and then. Keep loving your live! Sylvia, als dobber waar Q2 op drijft, wil ik je voor alle praktische hulp bedanken. Ik dank verder alle medewerkers van het ziekenhuis die me op een of ander moment ter wille zijn geweest. Weet dat ik zonder jullie ondersteuning dit werk niet heb kunnen doen.

Buiten het werk kan ik ook de nodige mensen bedanken. Een paar wil ik persoonlijk noemen. Om het werk los te kunnen laten heb ik de geweldigste vrienden. Wouter, Lars, Dylan, Thomas, ik ken jullie al jaren en weet zeker dat we nog veel mooie avonturen tegemoet gaan op de fiets, in de sneeuw en de kroeg. Bedankt dat jullie me de afgelopen jaren zovele mooie tijden hebben bezorgd. Tom, ik wil jou bedanken voor het recreëren. De ideale manier voor een soms zo nodige mentale reset.

Manon bedankt voor de hulp met het ontwerpen van de cover en voor de vele leuke tijden het afgelopen jaar.

Lieve pap, mam en George-Emile, bedankt dat jullie er voor me zijn. In de afgelopen jaren zijn ook moeilijke momenten voorbijgekomen en hier helpen jullie me altijd doorheen. De stabiele basis die jullie me bieden maakt het voor mij mogelijk om te doen wat ik doe. Ik kan jullie hier niet genoeg voor bedanken.

147